Title

Anatomy Inspired Hardware for Magnetic Resonance Imaging

Author

Gopalan, Karthik

Publication Date

2022

Anatomy Inspired Hardware for Magnetic Resonance Imaging

by

Karthik Gopalan

A dissertation submitted in partial satisfaction of the

requirements for the degree of

Doctor of Philosophy

in

Engineering - Electrical Engineering and Computer Sciences

in the

Graduate Division

of the

University of California, Berkeley

Committee in charge:

Professor Michael Lustig, Chair
Professor Ana Claudia Arias
Professor Moriel Vandsburger

Spring 2022

Anatomy Inspired Hardware for Magnetic Resonance Imaging

Abstract

Anatomy Inspired Hardware for Magnetic Resonance Imaging

by

Karthik Gopalan

Doctor of Philosophy in Engineering - Electrical Engineering and Computer Sciences

University of California, Berkeley

Professor Michael Lustig, Chair

Magnetic Resonance Imaging (MRI) is a powerful and non-invasive imaging modality that is widely used in medicine. MRI uses a static magnetic field, radiofrequency (RF) pulses, and linearly varying gradient fields to create high quality images of internal anatomy. Despite the ability to safely image soft tissue, MRI inherently suffers from low signal to noise ratio (SNR) which causes long scan times. In addition, the time required to perform multiple scans implies that most imaging is qualitative in nature. Instead of extracting the true value of quantitative parameters like T1, T2, and susceptibility, most MR images capture a single snapshot that is only weighted by these parameters. Speeding up and extracting more information from MR scans is an active area of research. In order to test new reconstruction methods and pulse sequences, it is necessary to have high quality phantoms that accurately mimic human anatomy. SNR of the scan can also be improved with form fitting receive coils since the signal drops off as a cubic function of the distance between the subject and the receiver.

To improve the SNR of MRI scans, this dissertation will discuss two methods for patterning receive coil arrays on complex three-dimensional surfaces. The first method involves spray coating conductive inks and dielectric materials onto a 3D printed surface. The second method uses vacuum forming, sandblasting, and electroless copper plating to deposit conductive traces onto curved polycarbonate substrates. To account for the deformation of vacuum forming, a graphical simulation to pre-distort trace designs was developed. Both processes produce coils that have similar performance to coils made with conventional methods.

This dissertation also discusses the development of slice phantoms that provide a more accurate representation of human anatomy compared to phantoms that are commercially available. A method is presented for preparing and 3D printing these phantoms with any segmented imaging data. A reproducible calibration process is described for creating agar gels that mimic a wide range of T1 and T2 values found in the body.

Contents

List of Figures

List of Tables

Acknowledgments

I always thought the acknowledgements would be the easiest section of my thesis to write. That was until I realized that this is the section that most people who open this document will read. These days, the acknowledgements are my favorite part of someone's thesis. They show a small glimpse into the author's life at that point in time.

There are so many people that helped me get through these past seven years. I will try to mention as many as possible but in the event that I forget someone close to me, I hope you know that you had a significant impact on my life. I hope you also know that I love to procrastinate and that I did not give myself enough time to write this section.

First I would like to thank my advisors Ana and Miki. Thank you for taking me in after my first year in graduate school. The friendship you two share is so special and I already miss our meetings together. I know we had some rough patches but I could always tell that you both cared about me and had my best interests in mind. Ana, you are truly inspirational. You handle tough moments in your work and personal life with so much grace. Miki, thank you for basically giving me free reign to build our lab. That was very special for me. I have loved seeing the way the group has changed over the years. We have so many common interests, I'm sure we would have been inseparable if we were the same age. Lets talk on the radio sometime, my call sign is KM6BJP.

I did two internships in graduate school. One at Palo Alto Research Center (PARC) where I worked with Steve Ready, Sean Doris, and Bob Street. That experience exposed me to the world of electroless plating and completely changed the direction of my PhD. The second internship was a small stint at Massachusetts General Hospital in Larry Wald's RF lab. I had the pleasure of working with one of the smartest people in the MRI community, Jason Stockmann. Thank you for guiding me through my first 7T coils. I am glad we have kept in touch and I hope you move to California.

During my time at Berkeley, I worked with some amazing undergraduate students starting with Nmachi Anumba and Chelsea Conaway. Marc Fisher was actually still in high school when he started working with me. Your energy and enthusiasm for life are contagious. Thank you to Jaren Mendelsohn for helping me with the vacuum forming simulation. I hope we have many more days of climbing together. Jolene Huey is exceptionally talented and has taken over the phantom project. I am so excited to see what you all will do in the future.

I had many wonderful collaborators over the years. Matt Waks, Jutta Ellerman, and Gregor Adriany from UMN are some of the nicest people that I have ever met. Thank you to Fraser Robb who listened to my presentations and always had something funny to say. Glad I am almost finished "writing the f'ing thing". Thank you to Thomas Grafendorfer for helping me at the beginning and end of my graduate career.

A huge thank you to Anita Flynn who helped me so much the last few years. You are such a special person. If you were around for my entire PhD I would have probably been twice as productive and much more organized. Thank you to both you and Eric for opening your home and machine shop to me.

There were many people in graduate school that I could talk to for hours. Jim Tropp's stories and mannerisms always managed to cheer me up. Thank you for advising me on coil design as well as life philosophies. I hope we can stay in touch. I have to acknowledge Logan Baldini, my favorite building manager, for putting up with me for so many years. Let me know if you strike it rich panning for gold. Thank you to Ryan Kaveh for being an excellent conversationalist and always being there to talk. Thank you to Adam Bush for always challenging my opinions. You have changed so much since I first met you and I am always happy to see how far you have come in life.

Thank you to my partner in crime Jon Tamir. I had no idea that you would become one of my greatest friends when Miki introduced us six years ago. I truly miss our long desk conversations. I am really happy that you have found a job that you like. Its so exciting to see the life you and Marcelle are building in Austin.

Thank you Joe, Natasha, and Alla for the lovely dinners and all of the advice that you shared with me over the years. Joe, I really appreciate that you included me on some of your extracurricular projects. I hope we can do many more of those together. I am so happy that you and Natasha are geographically together again. Alla, you are the strongest and most passionate person that I have ever met. You are certainly going to change the world if you haven't already.

There were many professors who helped guide me through this process. Thank you to Chunlei Liu for co-funding our lab space with Miki and always providing feedback on my projects. Let me know if Tristan would like a woodworking lesson in the future. Jon Pauly for being on my qualifying exam committee and letting me use your lab space in the evenings after my internship at PARC. Ren Ng and James O'Brien for guiding me into the world of computer graphics. Thank you to Moriel Vandsburger for being on both my qualifying exam and thesis committee. I always enjoyed our meetings when I was your GSI.

A large part of what makes graduate school a rich experience is the people that you share your lab space with. I was fortunate enough to be a part of two groups. Thank you to the alumni and current members of the Arias group including: Adrien, Claire, Han, Abhinav, Yasser, Ting, Mahsa, Igal, Balthazar, Maggie, Maruf, Payton, Carol, Xiaodong, Juan, Jasmine, Anju, Natalie, and Yuhan. Thank you to the many members of Mikgroup that made the lab and office special including Frank, Wenwen, Sidd, Alan, Xucheng, Shreya, Jingjia, Alfredo, Rebekah, Efrat, Gopal, Volkert, Rahul, Celine, Katie, and Arda. Thank you to Ke, Ekin, and Suma for bringing a new wave of happiness and creativity to the group. Ke, I hope you can dunk when you graduate because I certainly cannot. Ekin, I will always appreciate you for smuggling all of those Mavi jeans from Turkey. To Victor who was technically not in the group but was always fun to talk to and work with. I am excited to see what you will make in the future and if it will involve diamonds. I have to thank Zhiyong for constantly making me laugh. Our dinners with your family were so much fun, I hope I can visit you in China one day.

Thank you to the dinner crew of Michael K., Jera, Michael B., Nate, Sadie-Mae, Brittany, Elyse, Eric, and Daniel. Michael K., you have changed so much since I met you at a random bar night seven years ago. I am glad we have become close friends and hope we have many more adventures together. Thank you for always bringing the group together and getting us through this pandemic. Thank you to Eric for continuing to fuel my adrenaline addiction and getting me into climbing. I promise we will make it up the Nose in the fall. Nate, lets go skiing, I will try not to have pneumonia this time.

One downside of living in the Bay Area is the exorbitant rent prices but the major upside is that you get to live with many wonderful people in order to afford housing. Over the years many of my housemates have become my good friends. Thank you to Raghid who was my first friend in Berkeley. I'm glad we both have semi-functional cars now. I miss the times we stayed up playing music and chess with Mimo and Luc. I have fond memories of 2212 Parker with Lucas, MC, Marie, Christophe, Robin, and Bahador. My next communal housing experience was in the Ragency. Thanks to Aaron Schaller for always making me laugh, teaching me how to garden, and the long conversations. Thanks to Raghid, Mimo, Gaby, Matt, Lynn, Gabriel, Maddie, Abigail, as well as our honorary housemates Charlotte and Lydia for all of the adventures and dinners. Thank you to many other friends including Korok, Matthew, Gabriel, Luke, Nick, Casey, and Austin. Thanks to Jose, you are truly living my dream, I'm glad you took a chance and got out of the city.

I have to thank my parents for sacrificing everything to move to this country and giving me the life I have today. Thank you to my Fremont family for the meals and laughter. Its been lovely seeing the boys grow into adults.

Lastly, I want to thank my partner Zahra who has been with me through it all. Thank you for pulling me out of my darkest holes and supporting me through my crazy endeavors. I am so proud of you for making it through medical school and becoming a doctor. You are so smart and kind and I am excited for our life together.

Karthik Gopalan
May 2022
Berkeley, CA

Chapter 1

Introduction

1.1 Magnetic Resonance Imaging

Magnetic Resonance Imaging (MRI) is a non-invasive imaging modality that is widely used in medicine. MRI uses non-ionizing radio frequency (RF) pulses to construct high quality images of internal anatomy. The images are so good that when I started working in the field, it was hard to imagine how my work could make substantial contributions. Figure 1.1 shows an example of a localizer, a scan that takes less than 30 seconds and appears to produce high quality multi-slice images in three imaging planes. This seems like the holy grail, a fast scan that can create diagnostic quality images.

However, magnetic resonance has the power to produce images with much richer informa-

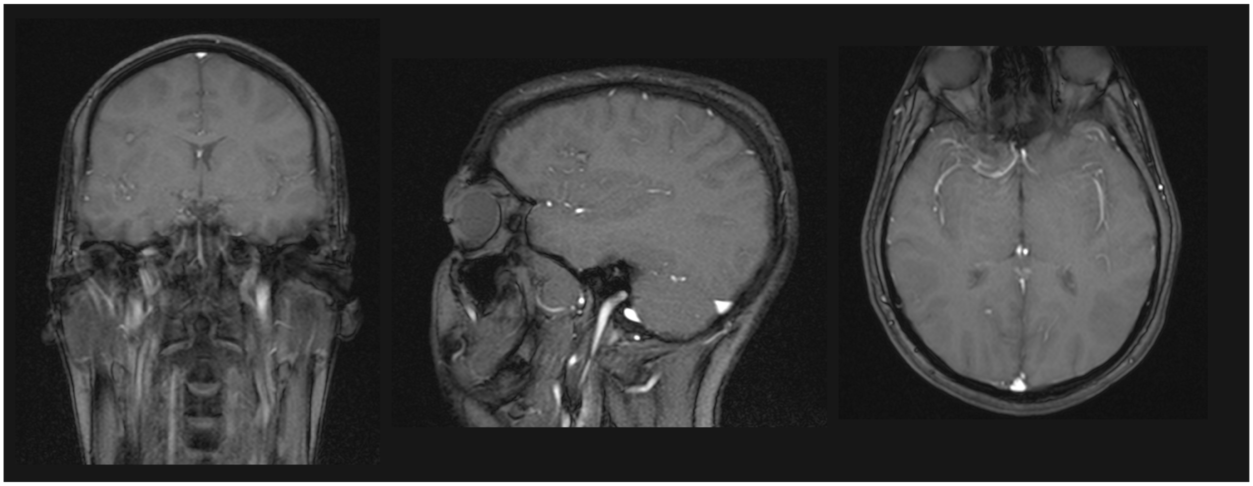

Figure 1.1: Localizer scan performed on a Siemens 3T Trio scanner. Imaging planes from left to right are coronal, sagittal, and axial.

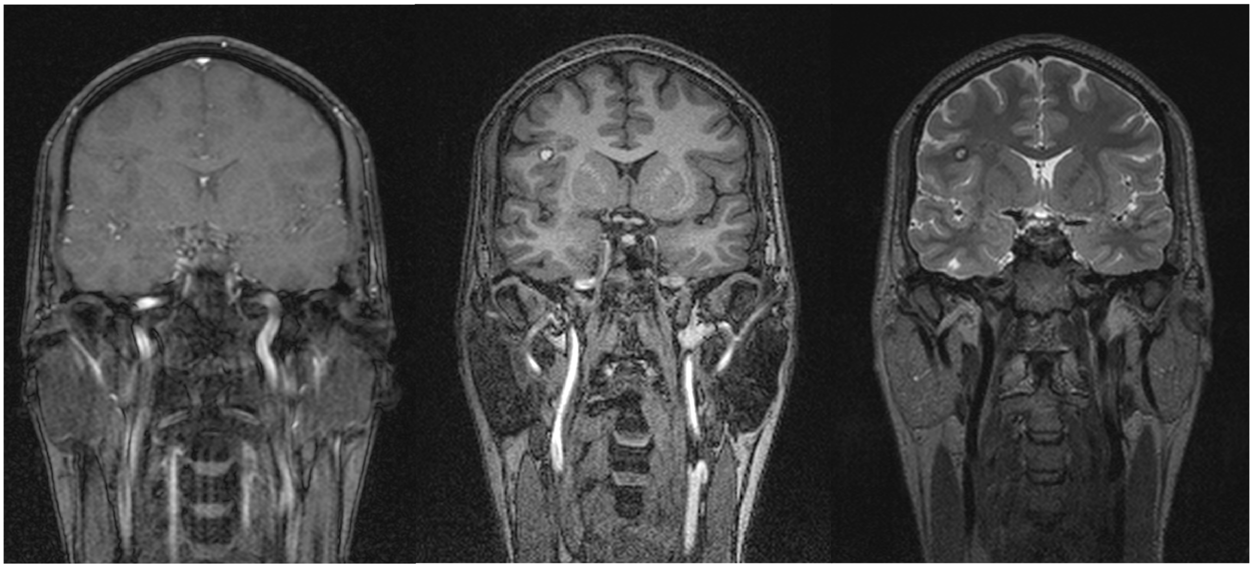

Figure 1.2: The power of contrast. Coronal scans from left to right, a localizer, single slice of a T1 weighted MPRAGE acquisition, single slice of a T2 weighted 3D fast spin echo sequence. Notice the benign cavernoma in the upper left side of the brain. This incidental finding is much easier to see in the T1 and T2 weighted images.

tion. Parameters including T1, T2, susceptibility, diffusion, blood oxygenation, and proton density all contribute to the signal displayed in a single voxel. Scanners use various pulse sequences and reconstruction methods to weight the images by these parameters. For example, a pure spin echo sequence [10] can generate an image with a T2 weighting where fluid is bright while an inversion recovery spin echo sequence can produce an image with a T1 weighting where fluid appears dark. Figure 1.2 shows three coronal images of a human head with varying contrast. The image on the left is from a localizer, the image in the center is a single slice of a T1 weighted scan, and the image on the right is a single slice of a 3D fast spin echo T2 weighted scan. A cavernoma [1], a benign vascular deformation, can be seen in all three images in the upper left side of the brain. This incidental finding is much easier to see in the images with T1 and T2 weighting compared to the image acquired with a localizer. Since the cavernoma is a pool of blood, it appears bright in both T1 and T2 weighted images. Despite being a fluid, blood contains iron which greatly decreases the T1 value.

These contrast weighted images can be used for diagnosing numerous diseases and conditions that cannot be seen with anatomical imaging alone. An example of this is myocardial edema, swelling or fluid build up in the heart muscle, which is typically diagnosed with a T2 weighted MRI scan [9]. Giri et al. showed that fully quantifying the T2 parameter with multiple scans led to a more accurate diagnosis.

The typical cost of this extra information is scan time. A full three dimensional scan of the head can take between 5 and 15 minutes depending on the desired resolution and contrast. This is substantially more time than what is required for a high resolution computed tomography (CT) scan of the head which only takes a few seconds. In addition, a single scan only provides a snapshot in time of the signal evolution and multiple scans are required to quantify certain parameters. Accelerating MRI scans is an active area of research. Compressed sensing [17, 8] and deep learning [31] can be used to reduce the amount of data that needs to be acquired. In addition, techniques like magnetic resonance fingerprinting [18] are used to extract more information from a scan with the same amount of acquisition time.

Magnetic Resonance Imaging has many areas for improvement. Faster and higher resolution scans would greatly expand its clinical utility. The work presented in this dissertation addresses a need for hardware that is inspired by anatomical features. The work presented here discusses new methods for manufacturing receive coil arrays that can improve the signal to noise ratio (SNR) of the MRI system. In addition, a later chapter provides methods to design and fabricate phantoms derived from digital scans of real human anatomy. Put together, these techniques attempt to improve the MR system by interfacing hardware with the body and providing a more realistic measurement tool.

1.1.1 Basic Principles

This section will provide a cursory overview of the basics of MRI. For a more detailed description please refer to the following resources. *MRI from Picture to Proton* [20] is a fantastic textbook with full color diagrams that provides a detailed and easy to read explanation of many concepts within MRI. *Principles of Magnetic Resonance Imaging* by Prof. Dwight Nishimura [23] is an excellent resource for the more advanced reader which explores the mathematical foundations of MRI in great detail.

MRI machines rely on a large main magnetic field called B_0. The common field strengths are 1.5 and 3 tesla. In the presence of the main field, the spin 1/2 protons in the body align with or against B_0. A slight majority of the protons will align with the field and produce a net magnetization vector. The torque presented to this magnetic moment causes the spins to precess at a rate known as the Larmor frequency (Equation 1.1). The gyromagnetic ratio γ is a constant in units of $^{\mathrm{rad}}/_{\mathrm{T}}$ that determines the rotation frequency of each nuclei.

$$\omega_0 = -\gamma B \tag{1.1}$$

To excite the precessing spins, a second field B_1 is presented in the rotating frame with an RF pulse at the Larmor frequency. This field tips the magnetization into the transverse plane orthogonal to the direction of the main field B_0. When the RF pulse is turned off, the magnetization vector of the spins relaxes back to its initial state of thermal equilibrium and its changing magnetic field can be detected with a receive coil. To achieve spacial encoding, MRI machines use linearly varying gradient fields which can superimpose a spatially dependent magnetic field on top of the existing static field B_0.

1.1.2 Receive Coils

Receive coils are used in order to capture the MR signal. After excitation, spins relax back to their original orientation and create a local changing magnetic field. This field can be detected by a resonant circuit tuned to the Larmor frequency due to Faraday's law of induction (Equation 1.2) which states that a electromotive force is generated in a loop of wire by a changing magnetic field.

$$\epsilon = -\frac{d\phi}{dt} \tag{1.2}$$

$$\omega = \frac{1}{\sqrt{LC}} \tag{1.3}$$

$$Q = \frac{\omega L}{R} \tag{1.4}$$

A resonant circuit accepts current around its center frequency which is defined by the oscillations between an indcutor and a capacitor. The formula for the angular frequency of an LC oscillator is provided in Equation 1.3 where L is the inductance in Henries and C is the capacitance in Farads. The quality factor of a resonator is a metric of how selective it is to a specific frequency. The quality factor can be calculated by dividing the resonant frequency by the bandwidth at the points where the signal is half of the maximum value. In addition, the quality factor (Q) of an LC oscillator can be defined by the inductance, L, resonant frequency ω, and the intrinsic resistance R which is displayed in Equation 1.4.

It is possible to make coils of wire that are selective to the MR frequency. There are many different styles of receive coils including solenoids, butterfly coils, dipoles, etc. The type of coil is typically chosen by the field strength, the imaging region, and the preferred imaging parameters. For example, dipole coils become too large to be used at lower field strengths due to the large wavelengths at the associated Larmor frequency. In addition, multiple coils can be arranged in arrays to accelerate imaging [25]. For more details about RF coil design the books *NMR Probeheads for Biomedical and Biophysical Applications* [21] and *RF Coils for MRI* [30] are invaluable resources.

The coil work in this thesis will focus on arrays of surface loops. The basic anatomy of a single surface loop is shown in Figure 1.3. It consists of a loop of wire, capacitors, inductors, a diode, coaxial cable, and a pre amplifier. The capacitors C_t are used to resonate with the inductance formed by the loop of wire. Multiple tuning capacitors are used in order to limit the voltage on each individual element and reduce electric fields. The matching capacitor C_m completes the loop and matches the impedance of the coil to the characteristic impedance of the rest of the receive system, typically 50Ω. A mechanism to de-tune or turn off the coil is necessary in order to protect the receive circuitry during the transmit phase of the MR sequence. This process of turning off the coil is typically called Q-spoiling and there are many

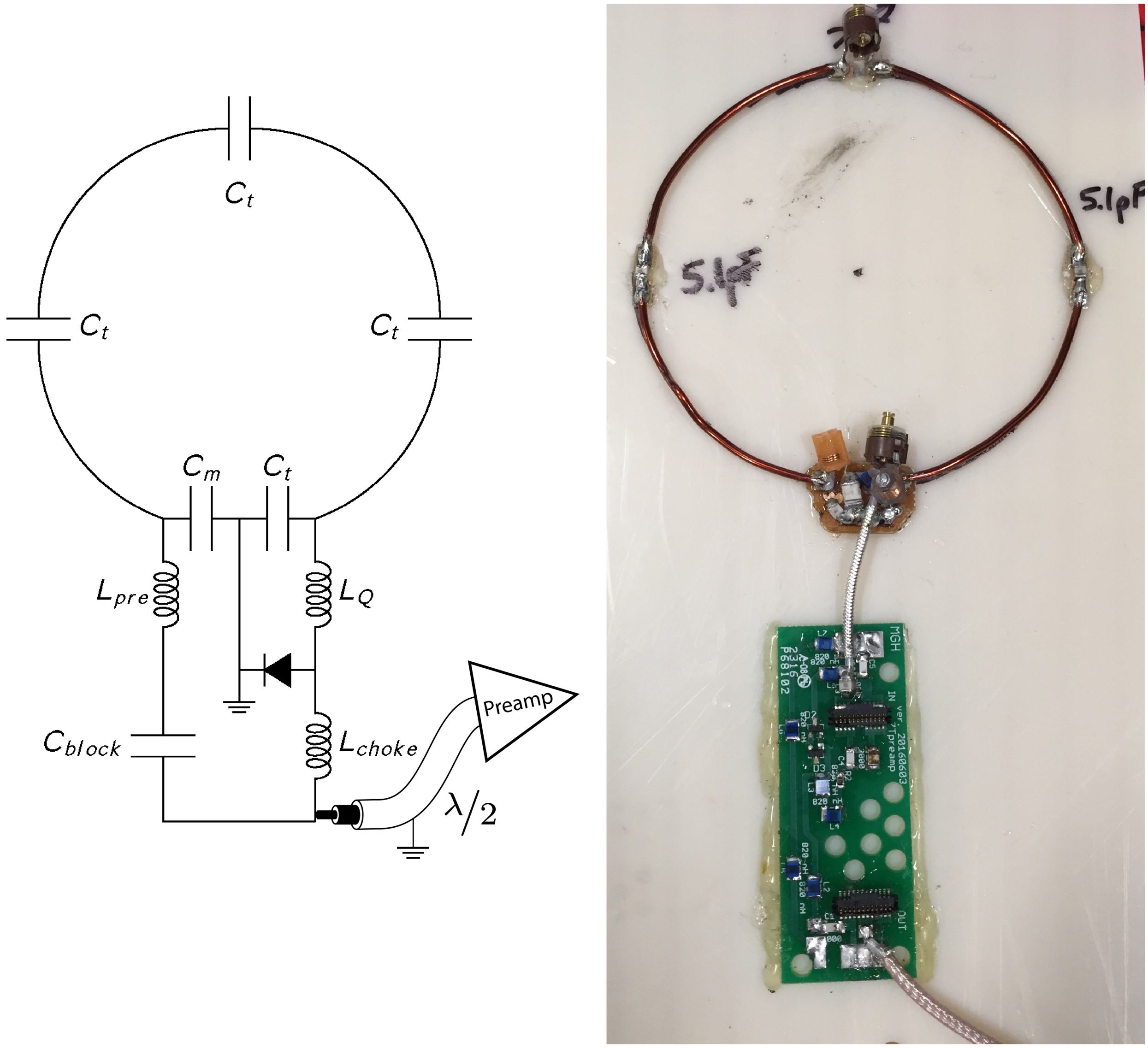

Figure 1.3: Schematic diagram of a single MRI receive coil on the left. A coil designed for 7T magnetic resonance imaging constructed with copper wire on the right. Notice the preamplifier is very close to the coil for improved signal to noise ratio.

methods to accomplish it. A pair of crossed diodes can be used in parallel with a tuning capacitor. During the transmit phase, enough voltage is induced in the coil which turns on the diodes and shorts the tuning capacitor. The most common method is to form a resonant trap between an inductor, the matching capacitor, and a shunt diode. When the diode is off, the coil functions normally but when a DC bias is applied the resonant trap blocks current from entering the receive chain [35]. The same method can be applied by Q-spoiling with a tuning capacitor as shown in the schematic in Figure 1.3. This arrangement requires more circuitry but results in a higher blocking impedance compared to Q-spoiling with the matching capacitor. Many coils also employ a non magnetic fuse within the receive loop that can stop all currents if any of the Q-spoiling circuitry were to fail. Boris Keil describes the construction of receive arrays in [14] using many of the tools shown in Figure 1.4.

Surface coils can achieve a high signal to noise ratio but their sensitivity is limited to the area around the loop. In order to achieve more coverage, it is possible to use multiple surface coils arranged in an array. However, coil elements placed next to each other will interact in unwanted ways. The mutual inductance between neighboring coils will cause a resonance frequency shift and an effect called peak splitting. This leads to lower SNR due to a lower quality factor and increased noise coupling. There are multiple ways to decouple neighboring coils but the most common technique is to geometrically decouple neighboring elements and rely on preamplifer decoupling for other pairs of elements. Geometric decoupling is acheived by changing the area of overlap between neighboring coils. Figure 1.5 shows a pair of coils measured with a decoupled double probe with a network analyzer. The coil shown in Figure 1.5A produces a nice resonance when measured in isolation. A neighboring coil that is far enough away does not interfere with the resonance but this distance leads to inadequate imaging coverage. Peak splitting occurs when there is significant mutual inductance between neighboring coils as shown in Figure 1.5D,E,G,H. At the point where the coils are critically overlapped (Figure 1.5F), the frequency response is indistinguishable from the response of an individual element.

Geometric decoupling works for neighboring coils but the distance between a coil and its next nearest neighbor cannot be controlled. To limit the coupling between these coils it is common to use a technique called preamplifier decoupling. This method uses a pi network or a length of coaxial cable to transform the impedance of the preamplifer to a low impedance across the PIN diode. This low impedance partially activates the Q spoiling circuitry which limits the current in the loop and presents a high impedance at the coil ports.

The signal to noise ratio (SNR) is an important consideration when choosing receive coil designs. Surface coils typically have a higher SNR near the coil while volume coils like birdcages and solenoids have a more uniform reception profile. The SNR of a circular surface loop was derived with surface integrals over the discretized space near the coil by Wang et al [32]. The coil area was represented as a two dimensional array of infinitesimally small dipoles. The resulting equation for the SNR of a circular surface loop is shown in Equation 1.5.

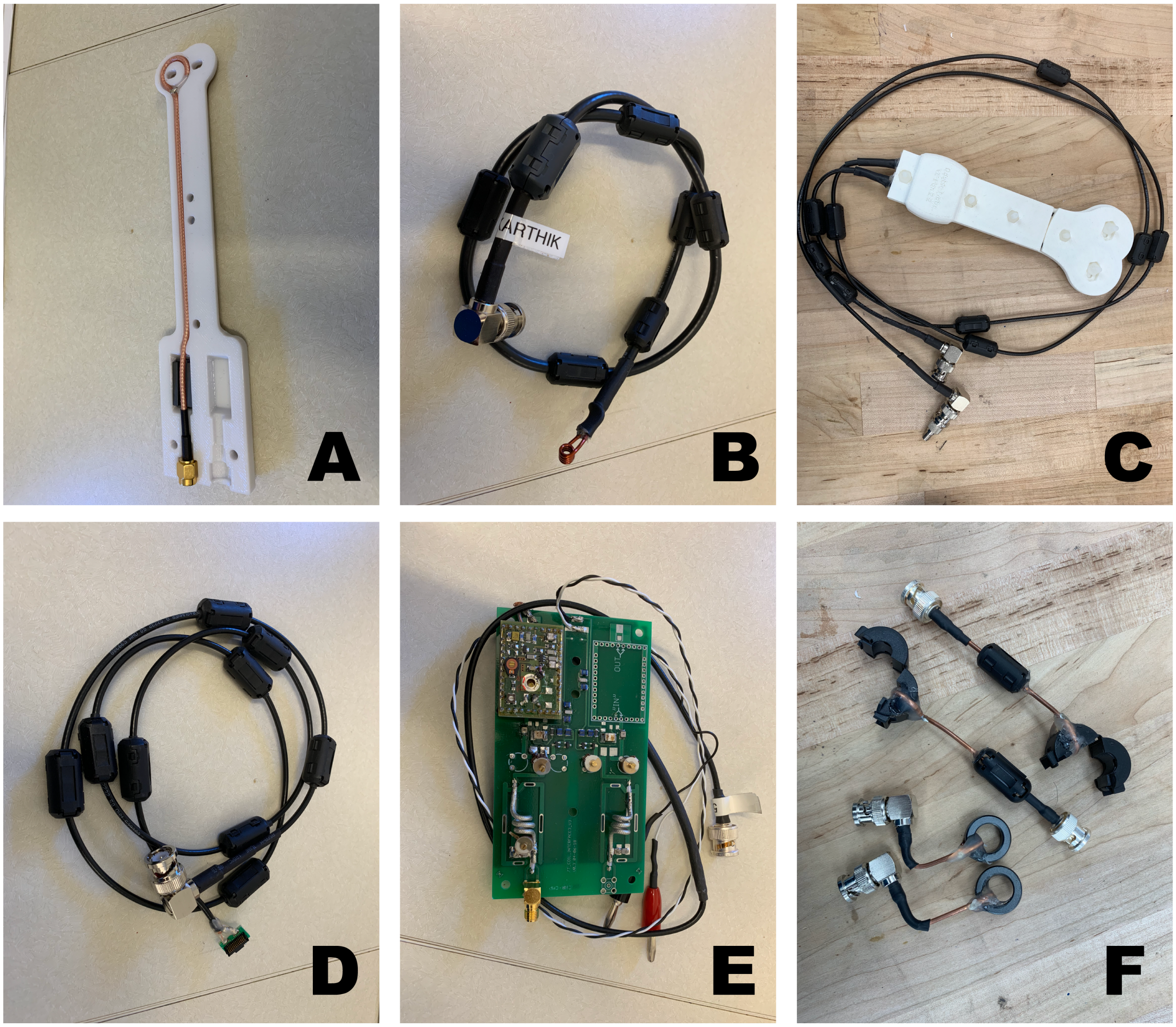

Figure 1.4: Tools used to build receive coils for magnetic resonance imaging. A. A single probe used for S11 measurements. B. Small sniffer probe used to excite inductors and miniature coils. C. A decoupled double probe used to interrogate RF structures with an S21 measurement. D. A preamplifier interface for a Siemens system. E. Single preamplfier with input balun used to check the performance of a coil when attached to a preamplifer. F. Current probes for measuring on cable baluns.

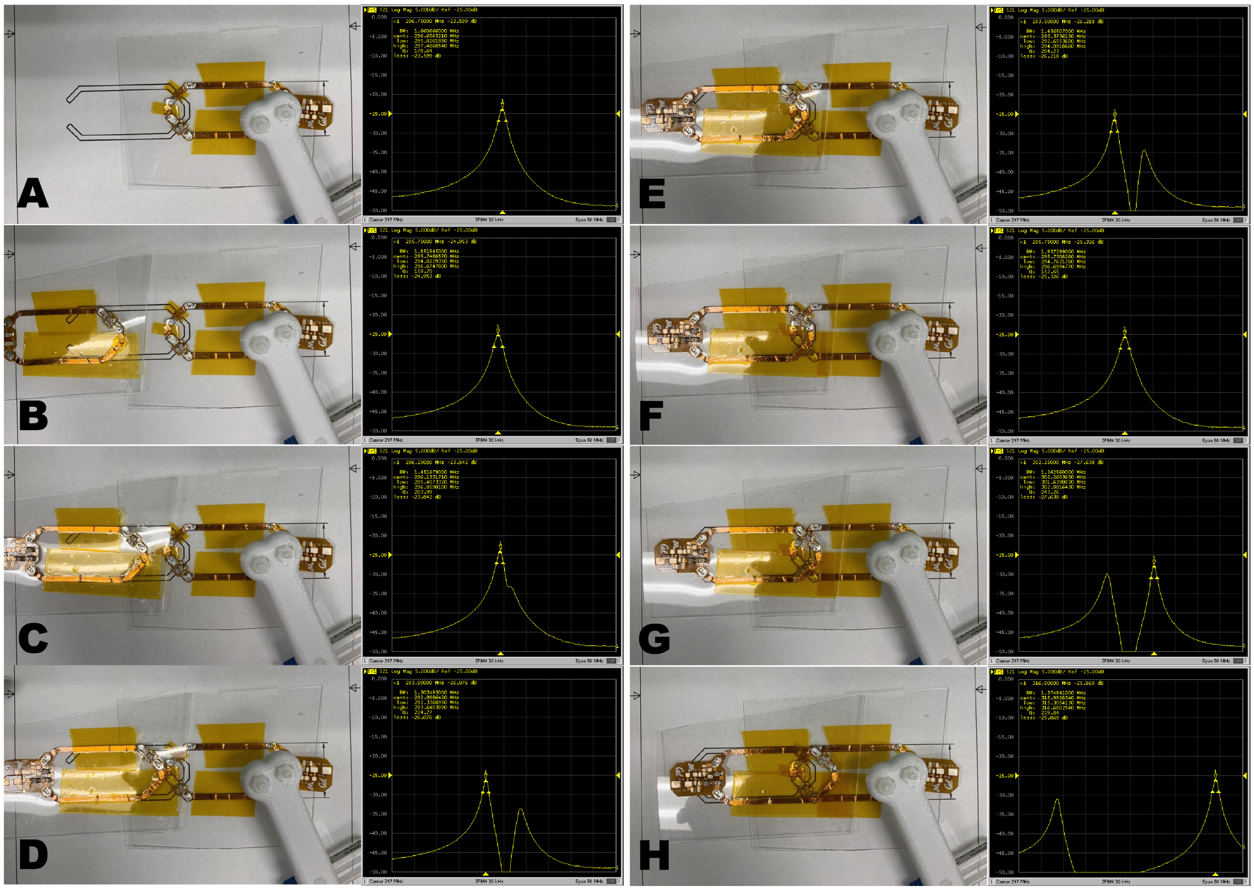

Figure 1.5: Effect of overlap between neighboring coil elements. The network analyzer traces reveal a different response depending on the distance between the two copper tape coils. A critical overlap distance is reached in F when the mutual inductance between the two coils cancels and the response is indistinguishable from the response of an individual element shown in A.

$$SNR = \frac{MV\sqrt{a}}{\sqrt{(a^2+z_p^2)^3}}\sqrt{\frac{3}{16kT\Delta f\sigma}} \tag{1.5}$$

Where M is the magnetization density, V is the voxel volume, a is the radius of the coil, z_p is the depth from the center of the coil into a conducting half space, and σ is the conductivity of the half space. The thermal noise is accounted for by the formula $\sqrt{4kT\Delta f}$ where k is the Boltzmann constant, T is the temperature, and Δf is the bandwidth of the receiver's low pass filter. This formula shows that the SNR of a circular surface loop drops off as a cubic function of distance as shown in Equation 1.6

$$SNR \propto \frac{1}{z_p^3} \tag{1.6}$$

Since the signal to noise ratio drops off as a cubic function of distance to the sample, these equations show how important it is to bring a surface coil as close to the subject as possible. Conventional receive coils are made with loops of copper wire and rigid components. These coils can be difficult and expensive to make since they required a skilled RF engineer to manually lay out and tune each element. Due to the complexity, it is more common for scanner sites to have coil arrays that fit the majority of subjects as shown by the head coil in Figure 1.6.

Most research in coil design focuses on expanding channel counts instead of fit [34, 27]. The increased number of coils allows more acceleration but a lot of SNR is lost due to the poor proximity to the subject. Since the noise is dominated by the sample, it is reasonable to sacrifice the intrinsic resistance of the coil or the quality factor [5]. This expands the material and design choices for substrates and conductors and allows the use of new manufacturing techniques that can bring coils closer to the body. The use of flexible and form fitting coils can boost SNR and have major benefits for improving patient comfort. The authors in [19] describe the use of a 16 channel flexible coil for MR guided radiation therapy and found that it produced comparable SNR to a conventional 30 channel coil. The flexible coil described was also more comfortable and had a smaller form factor. In 2018, Zhang et al. [36] described a method for making high impedance coils that were flexible and designed to be worn on a glove. The authors reported that these coils intrinsically limit coupling between neighboring elements and provided a high signal to noise ratio independent of overlap distance.

The coil work in this thesis focuses on bringing the coils as close to the subject as possible. This is achieved by pattering conductors on rigid three dimensional surfaces. New manufacturing techniques are presented that could speed up the process of coil development and allows coils to be made in many shapes and sizes. Figure 1.7 shows three coil arrays made with these new manufacturing methods. Figure 1.7A shows a hand coil made by vacuum forming printed conductive traces onto a mold of a hand. Figure 1.7B shows an 8 channel visual cortex coil made with a combination of vacuum forming, sandblasting, and

Figure 1.6: Commercial 14 channel head and neck coil designed to fit the majority of subjects.

electroless copper plating. Finally, Figure 1.7C shows a coil array made by spray coating conductive ink and a polystyrene dielectric onto a 3D printed substrate.

1.1.3 Quantitative Imaging and Phantoms

Quantitative magnetic resonance imaging (qMRI) is the use of MRI to extract and quantify various parameters like T1, T2, T2∗, flow, and diffusion [13]. qMRI has the power to generate much more information compared to qualitative scans. However, the cost of this information is a significant increase in scan time. In order to accelerate the development of faster methods, it is necessary to have standardized phantoms that can be used for testing and validating new sequences and reconstruction methods. Due to the lack of viable commercial options, there is a need for phantoms with anatomical features that replicate the tissue parameters found in the body. Work discussed later in this dissertation focuses on creating gels that mimic specific T1 and T2 values. T1 and T2 are time constants that define the measured MR signal. T1 is the rate of recovery in the direction parallel to the main magnetic field B_0. T2 is the rate of relaxation of the transverse component of a spin after excitation [29].

Figure 1.7: Examples of rigid coil arrays fabricated on three dimensional substrates. A) A multi channel hand coil made with vacuum forming. B) An eight channel visual cortex head coil made with vacuum forming and electroless copper plating. C) A four channel neck coil made by printing silver ink directly onto a 3D printed substrate.

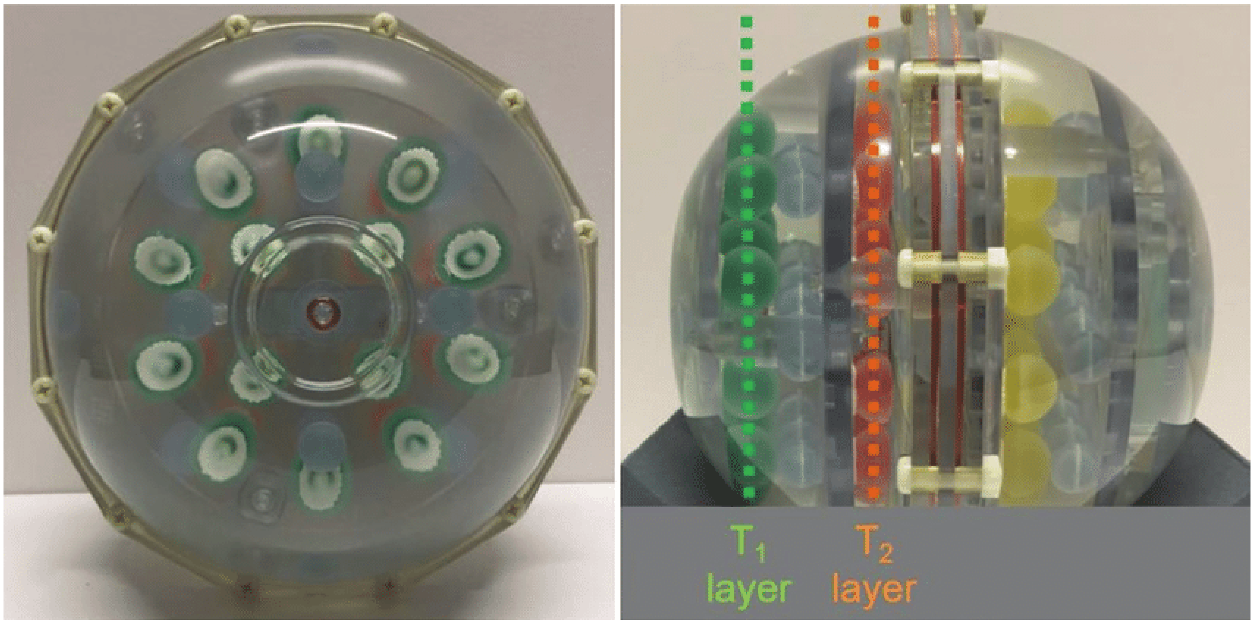

Figure 1.8: The gold standard phantom for quantitative MRI. The phantom consists of an arrangement of spheres filled with varying levels of an aqueous Manganese (II) Chloride solution. This phantom is commercially available at the time of writing and was designed by the National Institute for Standards and Technology (NIST). Image reproduced from [12].

$$
\begin{aligned}
M_z(t) &= M_0(1 - e^{-\frac{t}{T1}}) \\
M_{xy}(t) &= M_0 e^{-\frac{t}{T2}}
\end{aligned}
\tag{1.7}
$$

Equation 1.7 shows the effect of the time constants T1 and T2 on the longitudinal magnetization $M_z(t)$ and the transverse component of the magnetization $M_{xy}(t)$ where M_0 is the magnetization before a 90 degree excitation. T1 and T2 play an important role in the contrast of an MR image. Fluids exhibit long T1 and T2 values and appear bright in T2 weighted scans but dark in T1 weighted scans. Pulse sequence parameters are often chosen due to their effect on the T1 and T2 values of the tissue of interest. A sequence with a short TR will typically have a T1 weighted contrast as the signal is not able to fully recover in between excitations. Tissues with different T1 values will have varying effective initial magnetization before each RF pulse leading to a different contrast compared to a long TR where the spins can fully recover.

Most commercially available phantoms designed for testing qMRI methods are similar to the one shown in Figure 1.8. They consist of separate compartments of spheres and cylinders with simple shapes. Though phantoms like these are extremely useful, they do not replicate the intricate details of human anatomy. To make a more realistic phantom it is necessary

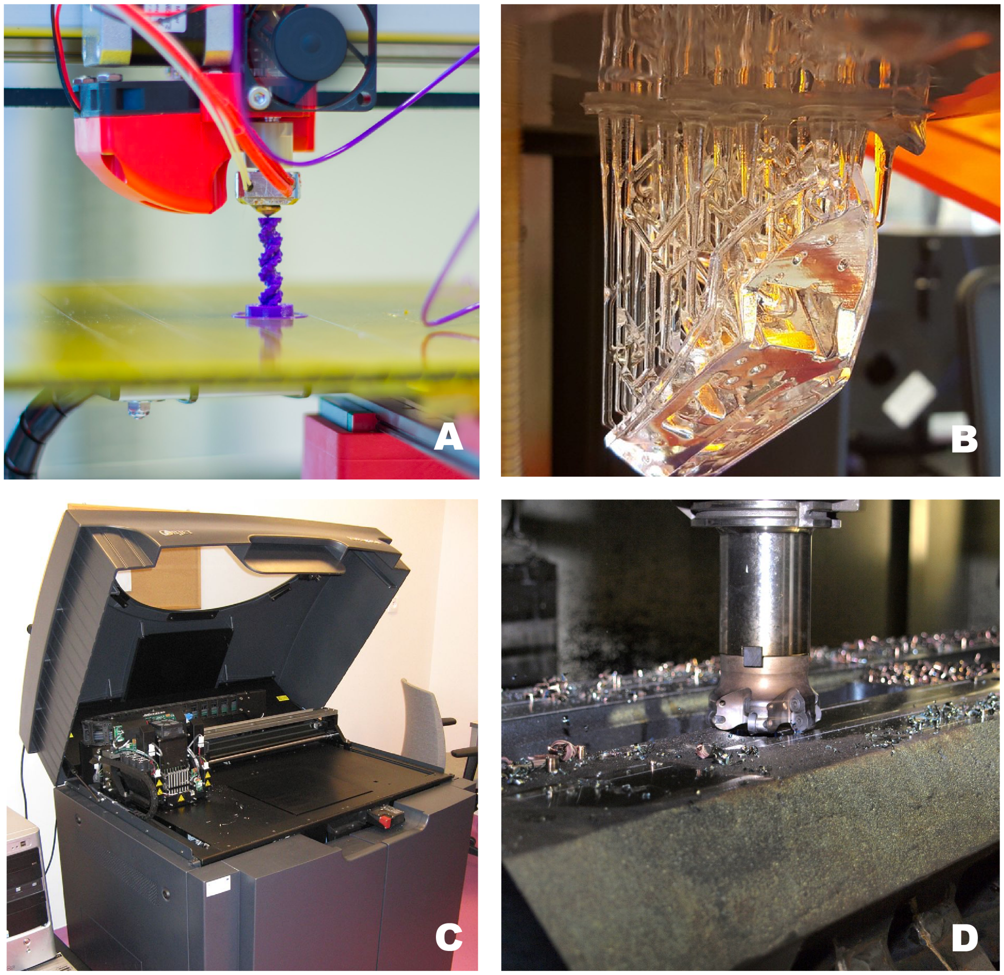

Figure 1.9: A few examples of digital manufacturing methods. A) A fused depostion modeling (FDM) 3D printer makes parts by extruding molten plastic through a small nozzle. B) Stereolitography (SLA) 3D printing uses high light sources to polymerize UV curable resins and make detailed parts. C) An example of an inkjet 3D printer which can quickly make parts by depositing UV curable resins through a piezoelectric nozzle. D) A part being machined by a computer numerical control (CNC) machine. The cutter head removes material in order to reveal the desired object.

to model T1 and T2 values found in the body [33] and house these values in an anatomical structure.

1.2 Digital Manufacturing

1.2.1 3D Printing

Three dimensional (3D) printing is a rapid prototyping technique that has changed dramatically over the past decade [22]. It is an additive method which uses various deposition processes to create functional and complex parts from digital 3D models. The first example of 3D printing was from the 1980's and used stereolithography (SLA) to cure layers of UV curable polymers and form a solid object. Recent advances to the process have made it cheaper, more accessible, and more functional.

Fused deposition modeling (FDM) is a process where a plastic filament is heated beyond its melting temperature and extruded through a nozzle (Figure 1.9). The nozzle is moved with a multi-axis actuator in order to print a part layer by layer. FDM printing is described in this thesis and was used to create masks for spray coated MRI coils as well as slice phantoms.

Significant advances have been made to SLA 3D printing. The major companies at the of writing are Formlabs and Carbon3D. Formlabs makes an SLA 3D printer that is accessible to universities, small companies, and affluent hobbyists. Parts can be made with various materials ranging from rigid to flexible, and clear to neon. An example of a part printed with the Formlabs printer is shown in Figure 1.9B. Our lab utilized the Form 2 and Form 3 for printing phantoms and various components for coil designs. These printers work by lowering a build platform into a tank of resin, curing a layer with a laser redirected with a galvanometer, lifting the stage, and repeating. Carbon 3D developed a printer with a process called Direct Light Synthesis (DLS). The resin build platform has an oxygen permiable membrane that prevents resin from curing directly on the surface. This allows the printer to print continuously without having to lift the stage and recalibrate. Parts from the Carbon 3D printer rival those create with injection molding. We used substrates from Carbon3D for our spray coated neck coil for carotid artery imaging. The substrates were made with cyanate ester, a high performance material that has excellent mechanical properties, high thermal stability, and good MR transparency.

Another method of 3D printing involves depositing UV curable polymers with inkjet printheads. The printheads use piezoelectric nozzles that can eject fluids at a high rate. Parts are printed layer by layer with a UV curing step in between. An example of an inkjet printer made by Objet is shown in Figure 1.9C. Inkjet 3D printing is useful for creating highly detailed parts. The build volume is typically bigger than that of an SLA printer and the inkjet printheads have the capability to print multiple materials. Parts made with these machines can have variable material properties like color and durometer.

There is also a 3D printing technique called selective laser sintering (SLS). This process uses a laser to cure a single layer in a bed of powdered polymer. A stage with the cured layer is lowered, the powder is flattened, and the curing process repeats for subsequent layers. Nylon is the most common material for SLS printing. Parts made with this method are strong, however the surface can be quite rough. It is possible to perform post processing methods like chemical vapor smoothing or ceramic tumbling to achieve a better surface finish. Since the parts are made while suspended in a bed of powder, support structures are typically not needed and complex geometries can be realized with this printing method.

1.2.2 CNC Machining

Computer numerical control (CNC) machining is a subtractive manufacturing method used to make complex parts out of various materials like metals, plastics, and composites. Machines range in capabilities including the ability to machine multiple axes with high resolutions. A basic CNC machine works with a rotating cutter head and a three axis stage. Stock larger than a part to be machined is mounted to the stage with a vise, clamps, bolts, or glue. This stock is moved relative to the cutter head and material is removed until the desired part is cut out of the base material. An example of a part being machined is shown in Figure 1.9D. CNC machining is quite powerful but has some downsides. The machine needs to be programmed which requires skill and knowledge of the materials and cutters. The process can also be wasteful since material must be subtracted away. Our lab used a Tormach 1100M CNC machine to accomplish various tasks throughout my time in graduate school. The main use of the machine was for cutting foam molds which were used for vacuum forming. Cutting large objects out of foam was much faster and more economical compared to other manufacturing methods like 3D printing. The CNC machine was also used to make fixtures and phantoms.

1.2.3 Vacuum Forming

Vacuum forming is an industrial process used to produce various items including hot tubs, storage containers, and packaging. The workflow involves heating a plastic sheet past its glass transition temperature, pulling it over a mold, and drawing vacuum to suck the plastic onto the mold. Once cooled, the mold is removed and reused. This process is widely used to make consumer products. Hot tubs, tupperware, takeout containers, and chocolate packaging are common examples of vacuum formed items. An image of a vacuum forming machine is shown in Figure 1.10. The parts of the machine consist of a heating element, a movable stage, vacuum pump, and a clamp for the plastic sheet.

In this thesis, we use vacuum forming to make receive coils for magnetic resonance imaging. The vacuum formed plastic can conform to most convex surfaces. This makes it ideal for MRI coils as it is possible to bring the receivers close to the body and potentially limit motion.

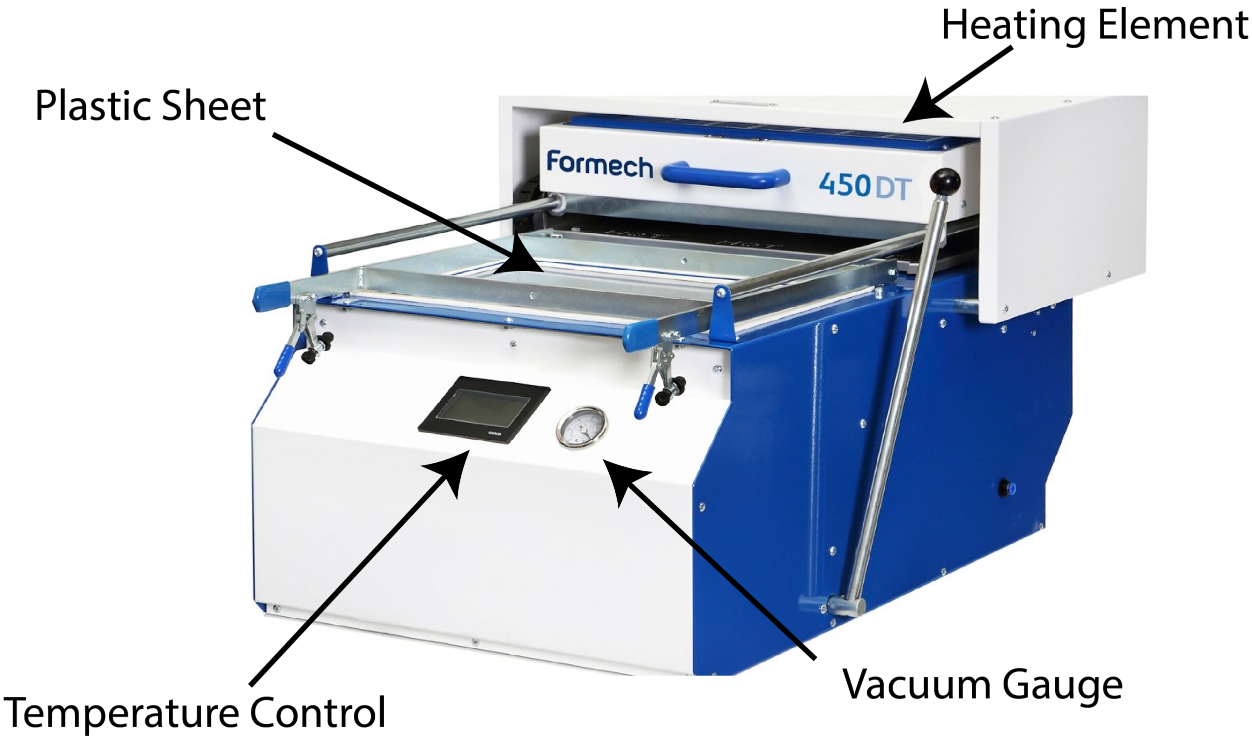

Figure 1.10: Formech 450DT benchtop vacuum forming machine. Image provided by Formech.

1.3 Flexible and Printed Electronics

1.3.1 Printing Methods

Printed and flexible electronics are a class of electronic devices that are produced by the additive deposition of materials including conductors, dielectrics, and semi conductors onto substrates such as plastic and paper [15]. Traditional electronics are formed by etching traces out of fiberglass boards laminated with copper. These printed circuit boards are easy to produce at a large scale and have excellent electrical properties. However, the production of these boards can be wasteful and their rigid nature creates issues when trying to conform to the complex surfaces of the body. Previous work from our group showed the benefits of a pulse oximeter that was printed on a flexible substrate[16]. With the ability to conform to the area of measurement, the pulse oximeter was more comfortable and produced a higher quality signal compared to a commercial counterpart. Another example that had a major influece on the work presented in this dissertation was the flexible receive coil arrays that were made by Joe Corea[5, 6, 4]. These receive coil arrays were screen printed with conductive silver ink onto PEEK substrates. He was one of the first to show that using new manufacturing

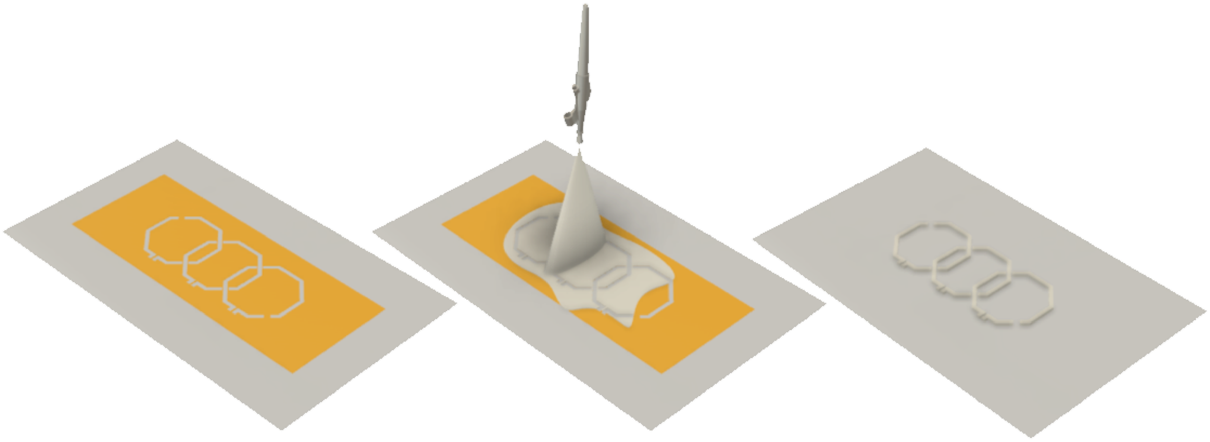

Figure 1.11: Spray coating conductive inks to form MRI receive coils on a flat plastic sheet. The inks are sprayed with a Badger 105 airbrush through a laser cut kapton mask.

methods to bring the coils closer to the body was worth the slight degradation of electrical performance of the individual elements.

Some common methods for printing electronics include inkjet printing, screen printing, gravure printing, and blade coating. Inkjet printing involves ejecting microscopic droplets of fluids and inks through a piezoelectric or thermally modulated nozzle [28]. Arrays of inkjet nozzles can be arranged in a high density to form a printhead. This allows printing with a high resolution and accuracy but limits the rate of material deposition. Inkjet printing works well for making intricate designs over a large area. The method is truly additive and allows rapid prototyping since the printed designs can be changed digitally. Due to the rate of deposition, it is necessary to print multiple layers to achieve a reasonable conductivity while inkjet printing conductors.

Screen printing is frequently used for printing garments. The process uses a mesh that is partially clogged to form a printing pattern. An ink or material with sheer thinning properties is then passed through the mesh to print onto a substrate. Screen printing is an excellent method for repeatably patterning various materials. One downside is that it is necessary to order a new screen every time the design needs to be changed. Another method of printing is called gravure printing. It is a high throughput process that is used to produce newspapers. Ink is deposited onto a drum that is etched with a printing pattern. Excess ink is wiped away and the drum is rolled over a substrate to pattern the material. This process is excellent for roll to roll manufacturing. A full spool of plastic film could be printed continuously with gravure printing. This process could be very powerful when making printed electronics at scale but it has some drawbacks while prototyping in the lab. Whenever the design of the printed structures need to be changed, the heavy steel drum needs to be machined.

Blade coating or doctor blading is a blanket coating method where a thin metal edge is dragged slightly above a substrate to spread a small film of material. The printed electronics presented in this dissertation primarily involved spray coating. The technique uses an airbrush to spray material onto a surface. It is possible to blanket coat a surface or pattern a material through a mask. Spray coating allows rapid prototyping and development since the masks can be laser cut in order to change the design. There are numerous parameters to control during spray coating including the nozzle size, air pressure, material viscosity, and the distance to the substrate. A schematic of spray coating a set of MRI receive coils through a kapton mask is shown in Figure 1.11. This process was used to pattern receive coil arrays directly onto a 3D substrate. By using spray coating, it was possible to print both the conductors and dielectrics to make tuning and matching capacitors for the coils.

1.3.2 Electroless Copper Plating

Copper plating is a method of depositing copper onto a surface. This is typically done for aesthetics or to make the object functional. Copper is an excellent electrical conductor that is relatively cheap compared to metals with similar conductivity like gold and silver. The electronics industry uses copper plating for creating printed circuit boards. The fiberglass boards are treated with a catalytic solution and then placed in a copper plating tank with an attached electrode. The copper plating tank contains copper ions in solution that are reduced to copper metal when they react with a grounded surface. Numerous metals can be plated including nickel, gold, silver, platinum, and palladium [26].

One requirement of this process is an attached electrode with an applied voltage. This means that anything that is going to be plated must already be conductive enough to form an electrical connection between the surface to be plated and an electrode. It is common to use a method called electroless plating to make a surface conductive. Instead of relying on an applied voltage, electroless plating solutions use a chemical reducing agent to convert a metal ion to its base metal and various reaction by products [7]. Compared to electrolytic plating, electroless plating produces a more uniform deposition over complex parts since there is no variability in current density. Electroless plating also does not require the conductive elements to be connected.

Electroless copper solutions consist of a copper salt, a reducing agent, a pH adjuster, and numerous additives. One example of a copper plating solution that is used in this thesis contains copper sulfate as a copper salt, Ethylenediaminetetraacetic acid (EDTA) as a complexing agent used to help the copper dissolve, formaldehyde as a reducing agent, sodium hydroxide to increase the pH, and potassium ferrocyanide to reduce the copper grain size.

$$HCOO^- + 2H_2 + 2e^- \Longleftrightarrow HCHO + 3OH^- \tag{1.8}$$

$$Cu^{+2} + 2e^- \Longleftrightarrow Cu^0 \tag{1.9}$$

Formaldehyde breaks down and reacts with hydroxide ions in a high pH solution as shown in Equation 1.9. This reaction creates electrons that are used to reduce the ionic copper into its base metal. Electroless plating requires a conductive surface to attract electrons. This is typically achieved with a thin layer of palladium metal. An aqueous solution of palladium and tin salts can be used to catalyze non conductive surfaces [24]. In acidic conditions, a reduction-oxidation reaction takes place to further oxidize the tin ions and reduce the palladium ions to palladium metal. This leaves the surface to be plated with a small layer of highly conductive and inert particles. Once the copper plating reaction starts, it is automatically catalyzed by the previous copper layer.

It is important to passivate a surface that is plated with copper. Copper readily forms oxides when exposed to air. These oxides reduce the conductivity of electronic components and can be detrimental for soldering. It is common to protect the copper by displacing the surface metal with one that is more inert. Immersion plating is a process that is not autocatalytic and will only deposit a single layer of metal. It is common to displace the top layer of copper with tin, gold, or silver since they are more stable in air. Another method of passivation is to cover the copper with an inert polymer.

Electroless copper plating has been used for printed electronics. The authors in [11] used copper plating to improve the conductivity of printed silver lines. Cook et al. [3] used inkjet printing to pattern catalysts and copper plate on paper substrates. The work presented later in this thesis uses electroless copper to pattern conductive traces on vacuum formed surfaces in order to fabricate MRI receive coils.

1.3.3 In-Mold Electronics

Injection molding is a technique for fabricating plastic components by injecting molten plastic into a rigid mold. In-mold electronics is a relatively new process for integrating electronics into injection molded plastic parts. The process involves printing conductive inks onto a thin polymer substrate and attaching rigid components with a pick and place machine. Next, the plastic sheet is vacuum formed into the shape of one face of the mold and the formed plastic is placed inside of the injection mold. The molten plastic surrounds the formed sheet and the electronic components are embedded into the plastic part. This process can create complex plastic parts that are integrated with electrical components like lights, buttons, and switches. Prior methods would involve designing rigid, fiberglass printed circuit boards and mechanically fastening them to the plastic parts. This posed numerous design challenges as the electronics were constrained to a flat plane of the circuit board and the assembly need to be put together manually. In-mold electronics integrated the assembly and manufacturing into one step. In addition, the electronics could be deformed onto a three dimensional surface which could create more interesting and elegant designs. A comprehensive review of the developments of in-mold electronics was written by Beltrão et al[2].

It is possible to make functional three dimensional electronics without injection molding. The vacuum formed plastic can be made with a thicker substrate in order to be more durable. However, vacuum forming printed electronics over complex shapes creates cracks in conduc-

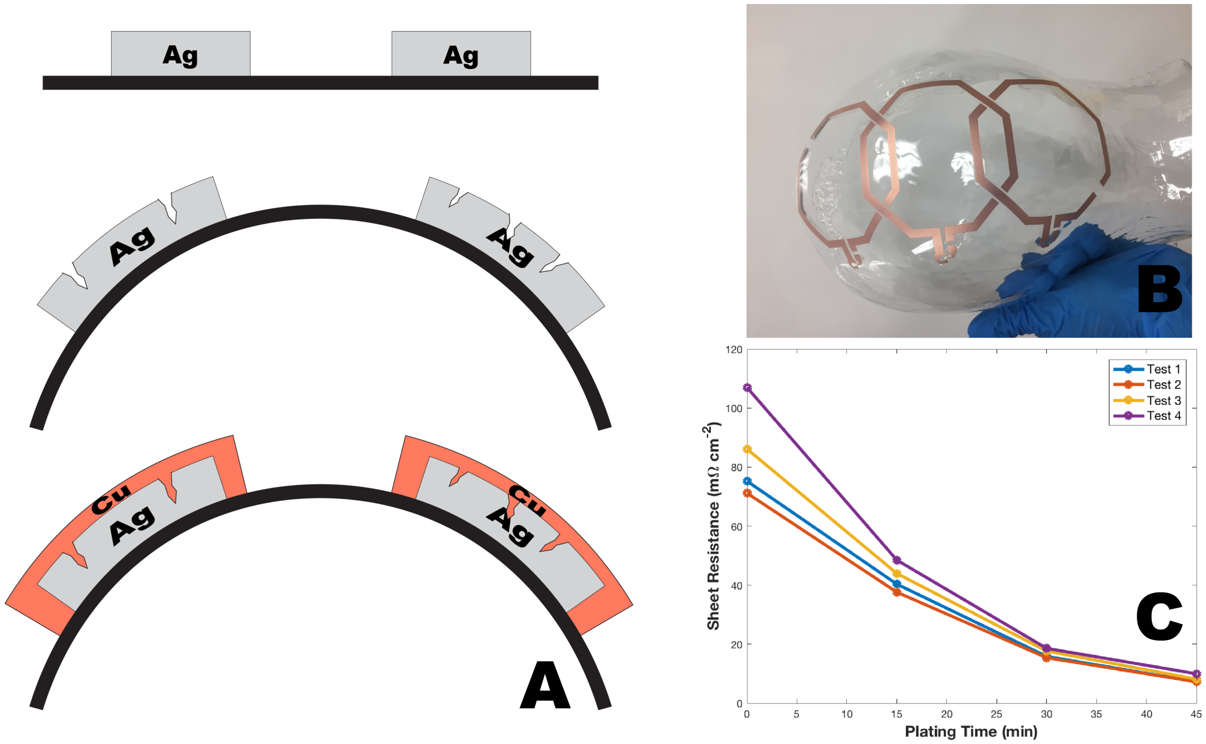

Figure 1.12: Example of electroless plating on printed silver lines. A. A schematic of electroless copper being applied to cracked silver traces. Silver cracks when the plastic substrate is vacuum formed. B. Copper plating a vacuum formed head coil with printed silver conductors. C. Copper plating on printed silver improves the sheet resistance of individual traces.

tive inks due to the extreme deformation during the forming process. This leads to reduced or entirely diminished conductivity which can be unusable for electronic components. This cracking is illustrated by the schematic in Figure 1.12A. One solution that we explored was to copper plate on top of the printed silver traces (Figure 1.12B). The copper filled in the gaps and improved the conductivity as shown by the graph in Figure 1.12C.

Printed silver is also an excellent heat reflector. This causes problems during vacuum forming since the plastic underneath the electronic traces cannot be adequately heated. The uneven heating leads to artifacts that can be difficult to model like raised edges around the printed traces. To expand the design possibilities for in-mold electronics, we came up with a method of directly copper plating onto a vacuum formed substrate. A flat plastic sheet is first cleaned and etched with the desired pattern. The etched pattern is catalyzed and vacuum formed. Since the catalyst only deposits a microscopic layer of palladium, it does not interfere with the vacuum forming process. The plastic is then loaded into the vacuum forming machine and formed over a mold. Once cooled, the formed part can be placed into an electroless copper plating bath to make the traces conductive. This method allows high density conductors to be patterned on complex three dimensional surfaces. A chapter in this thesis describes using this process for fabricating receive coil arrays for Magnetic Resonance Imaging.

1.4 Thesis Outline

Chapter 2

This chapter discusses a fabrication process for printing receive coil arrays on complex 3D printed surfaces. Coils are made by patterning silver conductive ink and a polystyrene dielectric to create resonant structures. The materials were spray coated through 3D printed masks. Careful material selection and characterization was performed. The chapter covers the construction of a prototype 4 channel coil array for carotid imaging. This coil was tested on the bench and used for in vivo imaging.

Chapter 3

Chapter 3 describes a different process for pattering coils on three dimensional surfaces. Instead of directly depositing the coils onto a 3D substrate, the coil geometry is designed on a flat plastic sheet and vacuum formed into a three dimensional shape. Coil conductors are made with electroless copper plating. The chapter describes simulation methods used to model and verify the mechanical aspect of the vacuum forming process as well as a simulation to investigate the electrical properties of the coils. To validate these methods, we constructed an 8 channel receive array to image the visual cortex. In vivo and phantom images are provided.

Chapter 4

This chapter describes a reproducible method for creating high resolution, quantitative slice phantoms. The phantoms are created using agar gels with different concentrations of $NiCl_2$ and $MnCl_2$ to achieve targeted T1 and T2 values. We describe a calibration method for accurately targeting anatomically realistic relaxation pairs. In addition, we developed a method of fabricating slice phantoms by extruding 3D printed walls on acrylic sheets. These procedures are combined to create a physical analog of the Brainweb digital phantom.

Chapter 5

The final chapter summarizes the work and discusses future directions.

Bibliography

[1] Issam A Awad and Sean P Polster. Cavernous angiomas: deconstructing a neurosurgical disease: Jnspg 75th anniversary invited review article. *Journal of neurosurgery*, 131(1):1–13, 2019.

[2] Mariana Beltrão, Fernando M Duarte, Júlio C Viana, and Vitor Paulo. A review on in-mold electronics technology. *Polymer Engineering & Science*.

[3] Benjamin S Cook, Yunnan Fang, Sangkil Kim, Taoran Le, W Brandon Goodwin, Kenneth H Sandhage, and Manos M Tentzeris. Inkjet catalyst printing and electroless copper deposition for low-cost patterned microwave passive devices on paper. *Electronic Materials Letters*, 9(5):669–676, 2013.

[4] Joseph Corea, Patrick Ye, Dongjin Seo, Kim Butts-Pauly, Ana Claudia Arias, and Michael Lustig. Printed receive coils with high acoustic transparency for magnetic resonance guided focused ultrasound. *Scientific reports*, 8(1):1–10, 2018.

[5] Joseph R Corea, Anita M Flynn, Balthazar Lechêne, Greig Scott, Galen D Reed, Peter J Shin, Michael Lustig, and Ana C Arias. Screen-printed flexible mri receive coils. *Nature communications*, 7(1):1–7, 2016.

[6] Joseph R Corea, P Balthazar Lechene, Michael Lustig, and Ana C Arias. Materials and methods for higher performance screen-printed flexible mri receive coils. *Magnetic resonance in medicine*, 78(2):775–783, 2017.

[7] Cheryl Deckert. Electroless copper plating, a review: Part i. *Plating and surface finishing*, 82(2):48–55, 1995.

[8] Mariya Doneva, Peter Börnert, Holger Eggers, Christian Stehning, Julien Sénégas, and Alfred Mertins. Compressed sensing reconstruction for magnetic resonance parameter mapping. *Magnetic Resonance in Medicine*, 64(4):1114–1120, 2010.

[9] Shivraman Giri, Yiu-Cho Chung, Ali Merchant, Georgeta Mihai, Sanjay Rajagopalan, Subha V Raman, and Orlando P Simonetti. T2 quantification for improved detection of myocardial edema. *Journal of cardiovascular magnetic resonance*, 11(1):1–13, 2009.

[10] Erwin L Hahn. Spin echoes. *Physical review*, 80(4):580, 1950.

[11] Chen-Yu Kao and Kan-Sen Chou. Electroless copper plating onto printed lines of nanosized silver seeds. *Electrochemical and solid-state letters*, 10(3):D32, 2007.

[12] Yutaka Kato, Kazushige Ichikawa, Kuniyasu Okudaira, Toshiaki Taoka, Hirokazu Kawaguchi, Katsutoshi Murata, Katsuya Maruyama, Gregor Koerzdoerfer, Josef Pfeuffer, Mathias Nittka, et al. Comprehensive evaluation of [b1+]-corrected fisp-based magnetic resonance fingerprinting: Accuracy, repeatability and reproducibility of t1 and t2 relaxation times for ismrm/nist system phantom and volunteers. *Magnetic Resonance in Medical Sciences*, 19(3):168, 2020.

[13] Kathryn E Keenan, Joshua R Biller, Jana G Delfino, Michael A Boss, Mark D Does, Jeffrey L Evelhoch, Mark A Griswold, Jeffrey L Gunter, R Scott Hinks, Stuart W Hoffman, et al. Recommendations towards standards for quantitative mri (qmri) and outstanding needs. *Journal of magnetic resonance imaging: JMRI*, 49(7):e26, 2019.

[14] B Keil. Construction of receive arrays. In *Proc Intl Soc Mag Reson Med*, 2013.

[15] Haibo Li, Yinji Ma, and Yonggang Huang. Material innovation and mechanics design for substrates and encapsulation of flexible electronics: a review. *Materials Horizons*, 8(2):383–400, 2021.

[16] Claire M Lochner, Yasser Khan, Adrien Pierre, and Ana C Arias. All-organic optoelectronic sensor for pulse oximetry. *Nature communications*, 5(1):1–7, 2014.

[17] Michael Lustig, David Donoho, and John M Pauly. Sparse mri: The application of compressed sensing for rapid mr imaging. *Magnetic Resonance in Medicine: An Official Journal of the International Society for Magnetic Resonance in Medicine*, 58(6):1182–1195, 2007.

[18] Dan Ma, Vikas Gulani, Nicole Seiberlich, Kecheng Liu, Jeffrey L Sunshine, Jeffrey L Duerk, and Mark A Griswold. Magnetic resonance fingerprinting. *Nature*, 495(7440):187–192, 2013.

[19] Kiaran P McGee, Robert S Stormont, Scott A Lindsay, Victor Taracila, Dennis Savitskij, Fraser Robb, Robert J Witte, Timothy J Kaufmann, John Huston, Stephen J Riederer, et al. Characterization and evaluation of a flexible mri receive coil array for radiation therapy mr treatment planning using highly decoupled rf circuits. *Physics in Medicine & Biology*, 63(8):08NT02, 2018.

[20] Donald W McRobbie, Elizabeth A Moore, Martin J Graves, and Martin R Prince. *MRI from Picture to Proton*. Cambridge university press, 2017.

[21] Joël Mispelter, Mihaela Lupu, and André Briguet. *NMR probeheads for biophysical and biomedical experiments: theoretical principles and practical guidelines*. World Scientific Publishing Company, 2015.

[22] Tuan D Ngo, Alireza Kashani, Gabriele Imbalzano, Kate TQ Nguyen, and David Hui. Additive manufacturing (3d printing): A review of materials, methods, applications and challenges. *Composites Part B: Engineering*, 143:172–196, 2018.

[23] Dwight G Nishimura. *Principles of magnetic resonance imaging*. Standford Univ., 2010.

[24] Sachiko Ono, Tetsuya Osaka, Kazuhisa Naitoh, and Yutaka Nakagishi. Mechanism of direct copper plating on nonconducting substrates. *Journal of The Electrochemical Society*, 146(1):160, 1999.

[25] Peter B Roemer, William A Edelstein, Cecil E Hayes, Steven P Souza, and Otward M Mueller. The nmr phased array. *Magnetic resonance in medicine*, 16(2):192–225, 1990.

[26] Mordechay Schlesinger and Milan Paunovic. *Modern electroplating*. John Wiley & Sons, 2011.

[27] Melanie Schmitt, Andreas Potthast, David E Sosnovik, Jonathan R Polimeni, Graham C Wiggins, Christina Triantafyllou, and Lawrence L Wald. A 128-channel receive-only cardiac coil for highly accelerated cardiac mri at 3 tesla. *Magnetic Resonance in Medicine: An Official Journal of the International Society for Magnetic Resonance in Medicine*, 59(6):1431–1439, 2008.

[28] Madhusudan Singh, Hanna M Haverinen, Parul Dhagat, and Ghassan E Jabbour. Inkjet printing—process and its applications. *Advanced materials*, 22(6):673–685, 2010.

[29] Jonathan I Tamir. *MR Shuffling: Accelerated Single-Scan Multi-Contrast Magnetic Resonance Imaging*. University of California, Berkeley, 2018.

[30] J Thomas Vaughan and John R Griffiths. *RF coils for MRI*. John Wiley & Sons, 2012.

[31] Ge Wang, Jong Chu Ye, Klaus Mueller, and Jeffrey A Fessler. Image reconstruction is a new frontier of machine learning. *IEEE transactions on medical imaging*, 37(6):1289–1296, 2018.

[32] Jianmin Wang, Arne Reykowski, and Johannes Dickas. Calculation of the signal-to-noise ratio for simple surface coils and arrays of coils [magnetic resonance imaging]. *IEEE transactions on biomedical engineering*, 42(9):908–917, 1995.

[33] Janaka P Wansapura, Scott K Holland, R Scott Dunn, and William S Ball Jr. Nmr relaxation times in the human brain at 3.0 tesla. *Journal of Magnetic Resonance Imaging: An Official Journal of the International Society for Magnetic Resonance in Medicine*, 9(4):531–538, 1999.

[34] Graham C Wiggins, Jonathan R Polimeni, Andreas Potthast, Melanie Schmitt, Vijay Alagappan, and Lawrence L Wald. 96-channel receive-only head coil for 3 tesla: design optimization and evaluation. *Magnetic Resonance in Medicine: An Official Journal of the International Society for Magnetic Resonance in Medicine*, 62(3):754–762, 2009.

[35] Graham C Wiggins, C Triantafyllou, A Potthast, A Reykowski, M Nittka, and LL Wald. 32-channel 3 tesla receive-only phased-array head coil with soccer-ball element geometry. *Magnetic Resonance in Medicine: An Official Journal of the International Society for Magnetic Resonance in Medicine*, 56(1):216–223, 2006.

[36] Bei Zhang, Daniel K Sodickson, and Martijn A Cloos. A high-impedance detector-array glove for magnetic resonance imaging of the hand. *Nature biomedical engineering*, 2(8):570–577, 2018.

Chapter 2

Custom, Spray Coated Receive Coils for Magnetic Resonance Imaging

2.1 Introduction

Healthcare technology can be significantly improved through customization to individual patients [1, 2, 3]. Magnetic resonance imaging (MRI) is one of the examples where the customization of hardware could appreciably advance clinical outcomes. One of the key factors determining signal-to-noise ratio (SNR) of MR images is the design of the receive coils that are used to collect RF signal and their proximity to the patient [4, 5, 6]. Particularly, placing coils close to the body has been shown to significantly improve SNR and, thus, diagnostic image quality [7, 8]. However, commercially available receive coils are typically designed to accommodate the largest possible subjects and do not optimally fit every patient or subject. This often results in substantial gaps between the coils and the body, which in turn compromises SNR. For instance, Corea et al. showed that placing coil only 1.8 cm away from the body results in an 8% decrease in SNR [7]. Additionally, conventional coils are not designed for reproducible positioning on the patient, and do not restrict a patient from moving, which leads to motion artifacts during MRI scans. These shortcomings hinder the development of the next generation therapeutic approaches, such as MRI guided surgeries [9, 10, 11], that require multiple time-consuming MRI scans on a given patient visit. In addition, fMRI researchers who perform repeated scans on the same subject may find the reproducible placement of the coils beneficial. Custom receive coils that are fabricated on-demand to fit a patient's or subject's anatomy would address some of the aforementioned imitations. However, the established commercial manufacturing process is not suitable for on-demand and custom coil production. Typical coil manufacturing requires a trained RF engineer and involves hand assembly and packaging of electronic components such as copper wires and porcelain capacitors [12]. Entirely new approaches that allow seamless manufacturing and integration of electronic elements must be adopted to enable custom MRI coils. Novel additive manufacturing techniques and solution-processed materials offer a potential to transform patient-specific coil manufacturing [13, 14]. The common concern with shifting towards solution-processed electronic materials is the higher loss associated with their use; for example, printed solution-based conductors exhibit lower conductivity than that of bulk metals [15]. However, in clinical MRI intrinsic losses in the system are dominated by losses stemming from the human body [16, 17]. Therefore, printed materials could perform comparably or better than the conventional materials, while enabling additive manufacturing of custom coils. The first demonstrations of the conformal MRI receive coils did not rely on additive manufacturing and were fabricated by sewing conductor into fabric [18], using mercury [19, 20], or copper tape [21, 22, 23] as a conductor. Mager et al. produced flexible coils using ink-jet printing [24]. While inkjet printing allows printing coils onto the flexible substrates, it requires many printing passes to achieve the desired conductivity for RF applications [13]. Corea et al. developed highly flexible and lightweight receive coils that were fabricated using scalable and low-cost screen-printing approach [7, 8, 11]. This paved the way to new opportunities in imaging, particularly for pediatric patients for whom conventional adult coils are especially problematic.

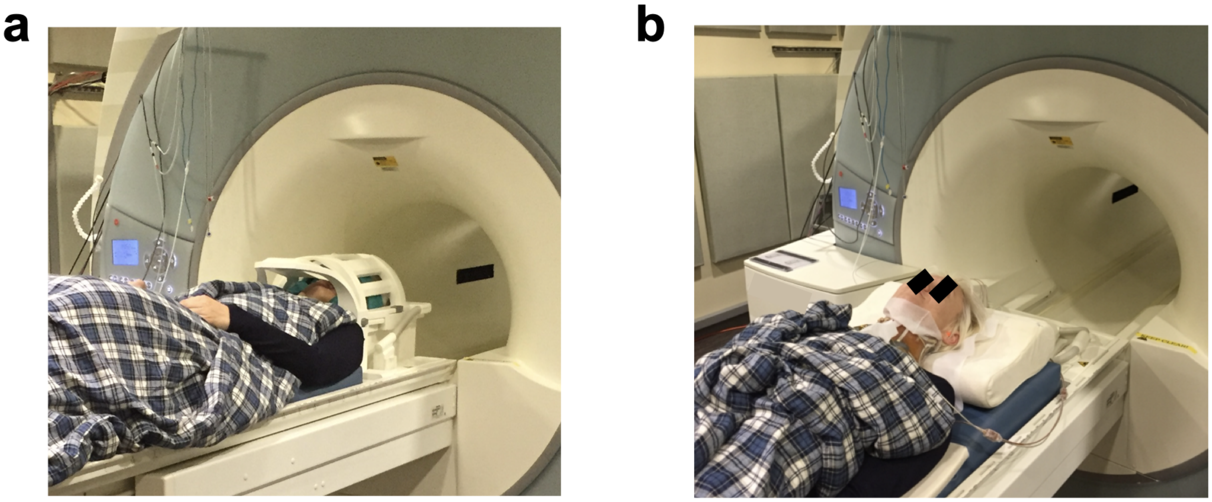

Figure 2.1: Photograph of volunteer prepared for MRI scan of the neck with the commercially available (a) and custom (b) neck arrays. The commercially available neck array (Siemens 3T) consisted of two elements operating in an integrated fashion with the head matrix coil. The custom array was fabricated by printing a pair of two-coil elements onto the substrate covering the entire neck surface area. Image reproduced from [25].

In this work we developed a process for additive manufacturing of 3D patient-specific MRI coils. Such coils are advantageous for applications where, in addition to improved SNR and reproducible placement on the patient are important. The 3D coils also ensure perfect fit to the body parts with complex geometries, like a neck, which is challenging to achieve with flexible 2D coils. To demonstrate how custom 3D printed coils can improve clinical imaging, we manufactured a custom neck array for c-spine and carotid artery imaging. Commercial neck coils are positioned at a distance from the body (Figure 2.1a) to have large field of view and fit the majority of subjects, at the expense of SNR. High-resolution neck imaging is an indispensable tool for the evaluation of health conditions involving the neck and cervical spine. For instance, lesions[26, 27, 28] or plaque accumulation in the carotid artery leading to stroke [27, 29, 30] could be imaged and detected. We used conventional and printed coil arrays to image a loading phantom in the shape of the neck mimicking human tissue and compared the SNR between the two coil arrays. The SNR measured with the printed array exceeded that of the commercially available four channel neck array (Siemens, Erlangen. Shown in Figure 2.5f) by forty percent in the center of the phantom and up to five hundred percent near the surface. Furthermore, we imaged a volunteer to generate high-resolution images of the neck and cervical spine. Images taken with the printed array exhibited less graininess and sharper tissue boundaries when compared to the images taken with the commercially available control and the same pulse sequence. Our fabrication approach for custom MRI coils can enhance high quality clinical or research subject imaging by ensuring an optimal fit of the MRI receive coils to body parts with complex geometries.

2.2 Results

2.2.1 Fabrication Process for Custom MRI Receive Coils

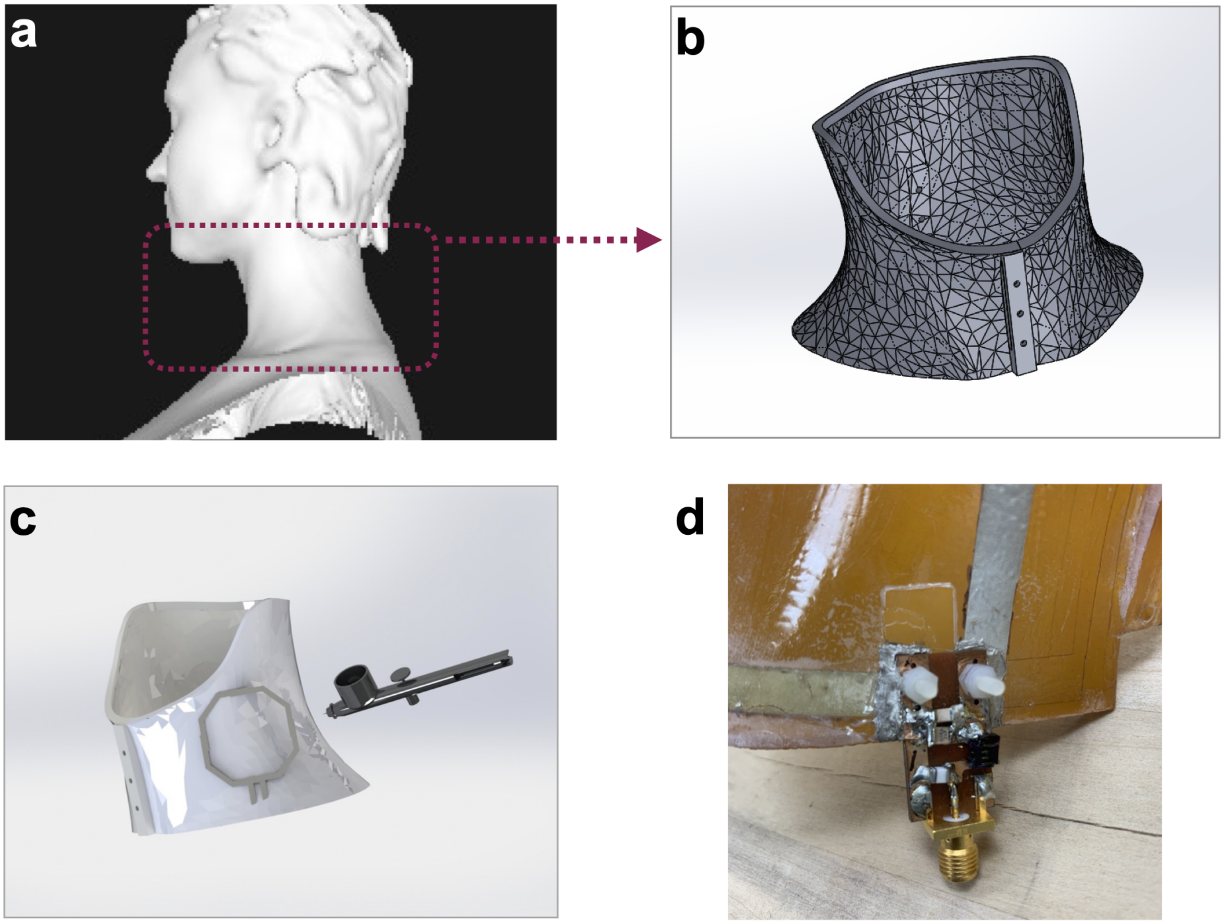

Figure 2.2: Manufacturing flow diagram for custom specific MRI receive coils. (a) A scan of the volunteer's body part (neck) generated using a structural scanner. (b) CAD drawing generated using the structural scan to perfectly fit the volunteer's neck and used to 3D-print a custom substrate. (c) Schematic representation of spray depositing coil components onto the 3D-printed custom substrate. (d) Q spoiling and matching circuitry connected to the coil with plastic screws and conductive epoxy. Image reproduced from [25].

The process for fabricating patient-specific MRI coils was designed to minimize the number of steps to enable on-demand manufacturing to drastically reduce the production lead time. In the first step, the patient's body part of interest is scanned using a commercially available hand-held structure sensor (Figure 2.2a). Then, a custom substrate of that region is 3D printed (Figure 2.2b). Finally, the solution-processed electronic materials are spray deposited onto these substrates to form the conductors and capacitors of the MRI receive coils (Figure 2.2c). This workflow can be readily adapted to the number of existing automated additive manufacturing approaches. We used the Carbon (Redwood City, CA) 3D printing process to fabricate the custom substrate. It enables the use of MRI transparent, heat and flame-resistant materials, as well as the ability to print monolithic parts with minimal artifacts of print anisotropy. We chose spray-deposition to layer coil components onto the substrate as it allows for rapid deposition of a wide range of electronic materials onto curvilinear surfaces. In order to spray-deposit patterns of desired geometry and eliminate the need for custom tooling or molds, custom masks were designed and 3D printed along with the substrate (Figure 2.8). Alternative deposition techniques such as aerosol jet or extrusion printing could be used in place of spraying to eliminate the need for printed masks.

2.2.2 Characterization and Optimization of the Coil Components

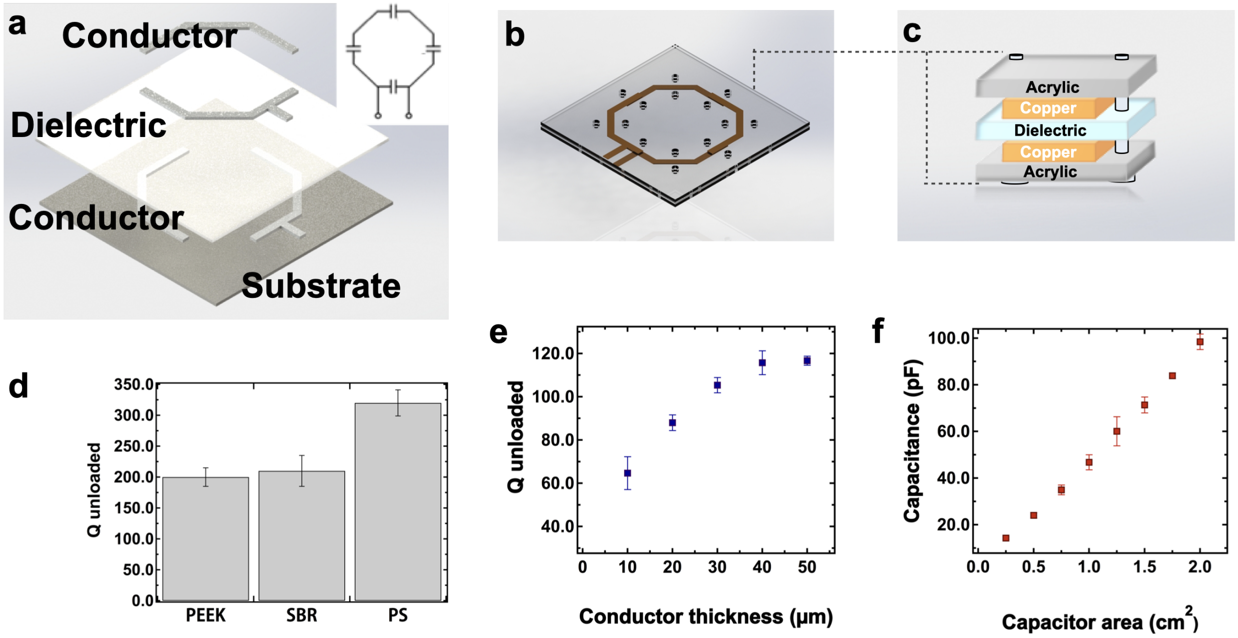

Figure 2.3: Characterization and optimization of coil components. (a) Schematics of the coil components that are sequentially deposited onto the substrate. The conductor traces are designed to overlap, forming coils with capacitors evenly spaced throughout the loop. Schematics of the top view (b) and crossection (c) of the custom setup used to characterize dielectric properties of the candidate materials. Dielectric films are spray-deposited onto the copper traces fabricated from the commercial foil. The copper coils are clamped together with the dielectric in between using two acrylic sheets. (d) Q unloaded of the styrene butadiene resin (SBR) and polystyrene (PS) dielectric films sprayed from the solution, and commercially available polyether ether ketone (PEEK) film. (e) Effect of conductor thickness on the Q unloaded. (f) Dependence of capacitance on the top electrode area. Image reproduced from [25].

Conventional MRI coils are resonant LC circuits formed with a loop of conductive wire and rigid porcelain capacitors. In order to achieve such circuit through spray deposition, we adapted a coil design previously reported by Corea et al. comprised of two silver conductor patterns with a dielectric layer separating them in certain areas [7]. Figure 2.3 shows the schematics of the corresponding layers that are sequentially deposited onto the substrate. The conductor traces were designed to overlap, forming coils with four parallel plate capacitors evenly spaced throughout the loop. Careful selection of materials is essential for achieving high performing sprayed MRI coils. Losses determined by the coil materials and fabrication approach can be characterized by measuring the quality factor in the absence of a sample (Q unloaded), which is inversely related to the loss contribution from the coil [8]. Losses from both dielectric and conductor material can contribute to a decrease in Q unloaded and, consequently, compromise SNR. Additionally, materials used to fabricate MRI receive coils must be MR Safe, as defined in the American Society for Testing and Materials (ASTM) standard F2503-05. Materials should also be tested for MR transparency by following the guidelines described in ASTM F2119. Furthermore, the substrate used in the current process must withstand exposure to high temperatures during the annealing process of the silver conductor. With all considerations, we selected a cyanate ester resin material from Carbon to fabricate the substrate. Cyanate ester's mechanical properties such as tensile strength and heat deflection temperature exceed those of commonly used plastics for MR devices like ABS and polycarbonate. Using alternative curing approaches such as pulse forge (Novacentrix) or UV curing would eliminate the need for heat resistive substrates and expand the pool of suitable substrate materials. The dielectric was chosen based on its ability to be spray-deposited from a solution, glass transition temperature of over $100^{\underline{o}}$ C to withstand the silver curing, and low dielectric loss to form high quality printed capacitors. Dielectric losses were measured at 123.3MHz, the characteristic frequency of our 3T MRI system. To characterize dielectric properties of candidate materials, we measured Q unloaded using a setup shown in Figure 2.3b. In this setup, a 60 μm thick dielectric film was spray-deposited onto 70 μm thick copper traces cut from a commercially available foil. Since the commercial copper foil is highly conductive (resistivity = 1.68x10-6 Ω-cm), losses of such coils are dominated by the dielectric loss of the tested films and the measured value of Q unloaded can serve an indicator of the dielectric properties of the films. The copper coils were tuned to a resonance frequency of 123.3 MHz and were clamped around the dielectric midlayer using two acrylic sheets (Figure 2.3c). Q unloaded was then measured using a network analyzer centered at the Larmor frequency (123.3 MHz). This testing setup has previously been shown to produce reliable Q unloaded measurements of dielectric films with minimum interference from the acrylic sheets [11]. Figure 2.3d compares the unloaded Q of spray-deposited styrene butadiene rubber (SBR) and polystyrene (PS) dielectric films to the unloaded Q of a commercially available polyether ether ketone (PEEK) film previously used to fabricate printed flexible MRI coils. Measured values were averaged over three trials to equal 200, 210 and 320 for PEEK, SBR and PS respectively. The Q unloaded value of the PEEK film was consistent with the previously reported results [8], confirming the reliability of the testing setup. The PS film had the highest Q unloaded and, thus, was chosen as the dielectric for the custom MRI coils. We further verified that dielectric properties of the PS films would not be affected by heating during silver curing. We exposed the films to the temperatures ranging from $25^{\underline{o}}$ C to $110^{\underline{o}}$ C for 30 min (the amount of time required to cure the silver layer, Figure 2.4a). The resulting average Q fluctuated between 318 and 341(Figure 2.4b) without direct correlation to temperature. Such fluctuations could be partially attributed to the variations in positioning and orientation of the setup that affect the measured Q on a network analyzer.

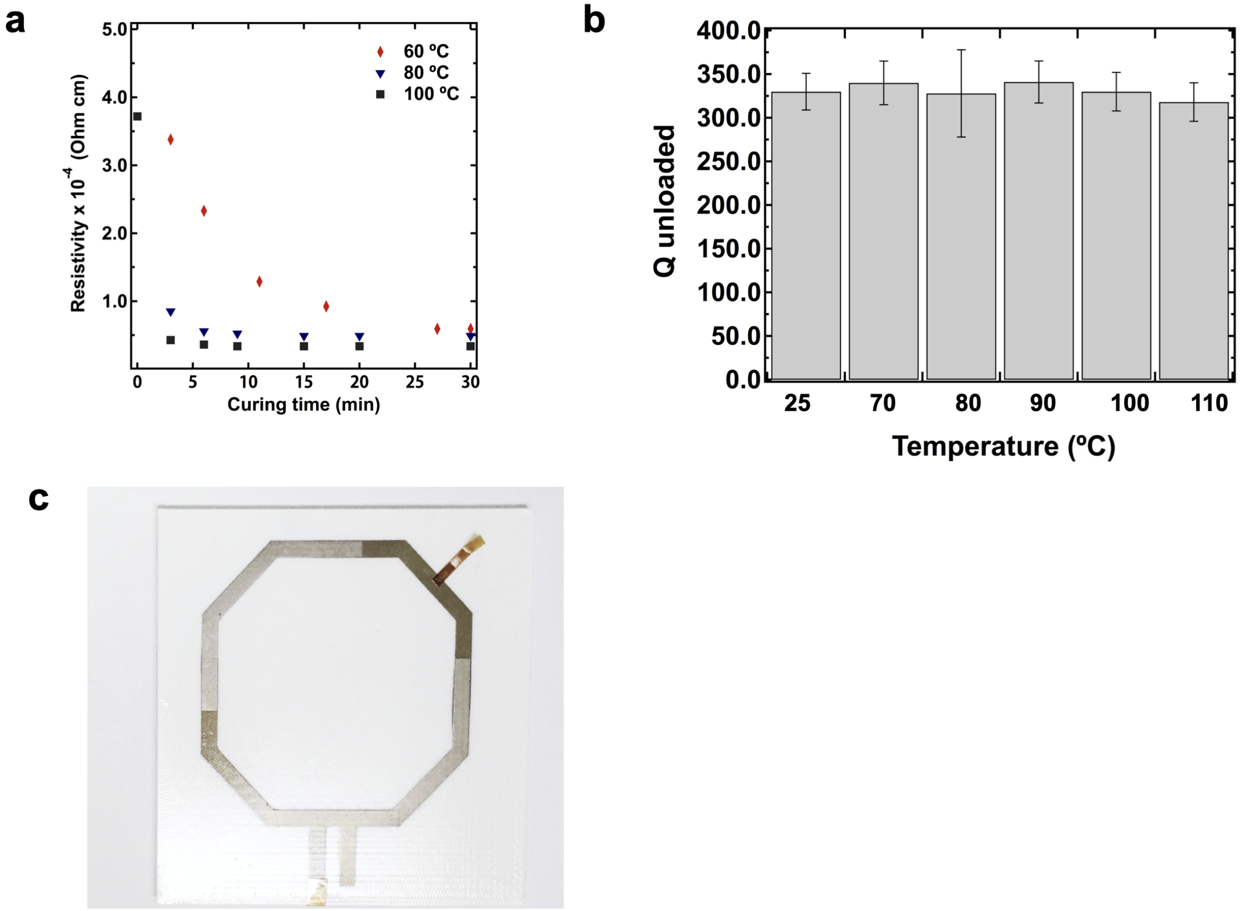

Figure 2.4: A) Effect of curing time and temperature on the conductivity of the silver traces. B) Effect of temperature on the dielectric properties of the polystyrene films, measured as change in Q unloaded. The films were exposed to the temperatures ranging from 25º C to 110^o C for 30 min. C) Photograph of a fully printed MRI receive coil fabricated via spray deposition of 10μm thick printed conductor traces and PS dielectric on a planar substrate. Image reproduced from [25].

A commercially available silver ink (PSPI 0250, Novacentrix) was used to create the conductive layers. It is an aqueous nanoparticle ink formulated for spray deposition processes. The water-based ink does not solvate the PS layer which helps to avoid short-circuiting between the top and bottom conductor traces. This ink can also be cured at relatively low temperatures of 80º C - 100º C, which is below the glass transition temperature of polystyrene (Figure 2.4a). Fully printed coils fabricated with 10 μm thick printed conductor traces and a PS dielectric layer (Figure 2.4c) resulted in a measured Q unloaded of 65 compared to the Q of 320 obtained with copper foil traces. This indicated that losses in the coil were dominated by the conductivity of the printed silver film. Printing additional silver layers increases the thickness and the conductivity of the silver traces and, in turn, the Q unloaded of the coil. We found that Q unloaded increases to the maximum value of 120 when the thickness of the conductor reaches 40 μm (Figure 2.3e). Further increases in conductor thickness has negligible effect on Q unloaded, as the conductivity of materials in AC current is limited by the skin depth effect. Therefore, we printed 40-μm-thick silver traces to fabricate all subsequent coils. It is important to note that in the clinical settings, imaging losses from the patient dominate the overall loss of the system [16, 17], and after a certain point, an increase in Q unloaded does not meaningfully improve the SNR. Our group previously demonstrated a method relating Q unloaded of the printed coils to its SNR in an image of a homogeneous phantom mimicking human tissue [8]. The results showed that increasing Q unloaded above 100 would only increase SNR of the printed coil by 3% compared to the control coil consisting of metal copper traces with porcelain capacitors. Thus, although the Q unloaded of the fully printed coils is lower compared to the Q of the coils with the copper foil traces, the difference between the two is negligible for all practical purposes. In contrast, the ability to place custom coils close to the body would result in significant SNR gains. The distance between a custom coil and patient is set by the thickness of the substrate to be on the order of 0.5 cm, eliminating the loss in SNR and minimizing the capacitive coupling to the patient. Changing the inductance and capacitance controls the resonant frequency of the coil. In the current process, the size and geometry of the loop fixes the inductance. We therefore adjust the capacitance to tune the coil to the Larmor frequency. Figure 2.3f demonstrates that varying area of a capacitor from 0.25 cm^2 to 2 cm^2 results in capacitance values ranging from 13 pF to 102 pF, which is sufficient to reach specific frequencies used in the MRI scanner (123.3 MHz; Siemens 3T Trio, Erlangen, Germany).

2.2.3 SNR from the Custom Coil Array

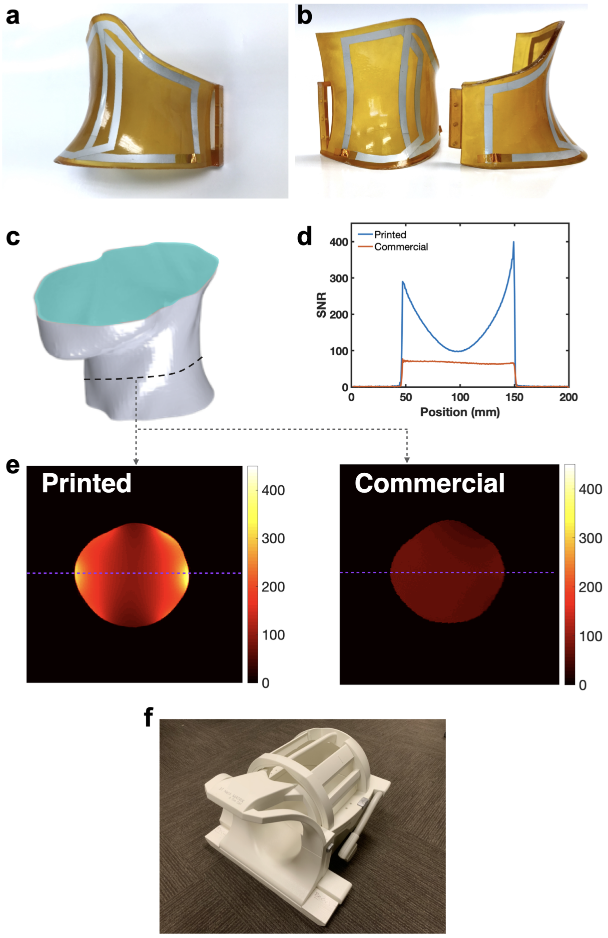

Figure 2.5: SNR from the custom coil array. (a) Photograph of the custom array fabricated by printing a pair of two-coil elements onto the custom substrate (b) Photograph of the top custom arrays covering the entire neck surface area (c) Schematics of the phantom consisting of 3D printed casing in a shape of the patient's neck and containing solution of salts mimicking human tissue (d) SNR of the printed and commercial coils along the crossection of the slice though the middle of the neck. (e) SNR maps of the phantom using the printed and commercial arrays. Dashed lines indicate the location of SNR cross sections shown in (d). SNR was normalized to the maximum seen with the printed array. (f) Image of the commercially available 4 channel neck coil attached to a 12 channel head coil. Image reproduced from [25].

Our approach aims to enhance high quality clinical imaging by ensuring an optimal fit of the MRI receive coils to the body parts. In order to demonstrate the benefits of using custom coils in clinical setting, we designed a custom array to image the neck and compared the SNR between conventional and printed coil arrays. The custom array was fabricated by printing a pair of two-coil elements onto the substrate covering the entire neck surface area for a total of four channels (Figure 2.5a,b). The elements' shape was adjusted to fit the substrate and maximize the coverage, while retaining the original four-capacitor circuit design. Neighboring coils were overlapped to minimize coupling. The commercially available neck array (Siemens Healthineers, Erlangen) consisted of four elements operating in an integrated fashion with the head matrix coil (Figure 2.5f). Both arrays were used to image a homogeneous loading phantom consisting of 3D printed casing in a shape of the patient's neck and containing solution of salts mimicking human tissue (Figure 2.5c).

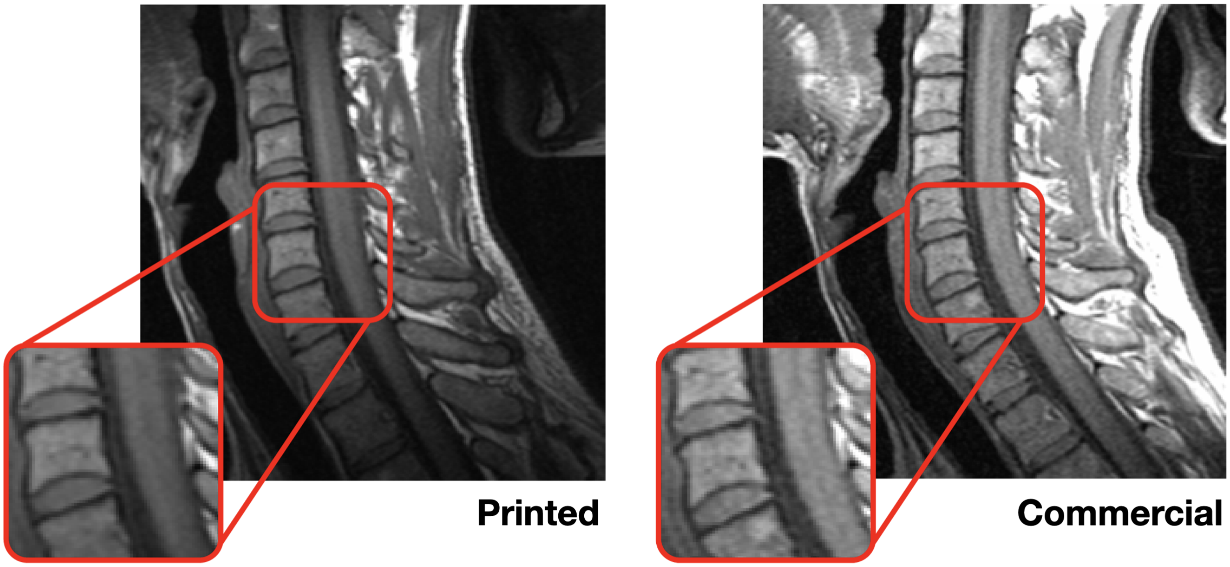

Figure 2.6: Sagittal image of the spine of the volunteer taken with printed (left) and commercial (right) coil arrays. Image taken by the custom array has less graininess and more clearly differentiated tissue interfaces. The window level of the image taken with the commercial coil was adjusted to emphasize the noise. Image reproduced from [25].

Due to improved conformability to the phantom and the higher number of coil elements, the printed array produced higher SNR throughout the cross section of the phantom. Figure 2.5d compares SNR of the printed and commercial coils along the cross section of the slice though the middle of the neck. SNR of the printed array exceeds that of the commercial array by forty percent near the center of the phantom and up to five hundred percent near the surface. The effect of coil proximity on the SNR can also be clearly seen from the SNR maps shown in Figure 2.5e, where the regions near the conductive traces of the elements yielded the highest signal. Thus, custom printed coil arrays can yield higher SNR compared to commercially available counterparts, despite the lower performance characteristics of the solution-processed materials used for printing of the coil components. This translates into higher quality images taken by the custom array, having less graininess and more clearly differentiated tissue interfaces (Figure 2.6). The experiment demonstrates that high quality custom 3D printed and sprayed coils are possible.

2.2.4 In-vivo Imaging

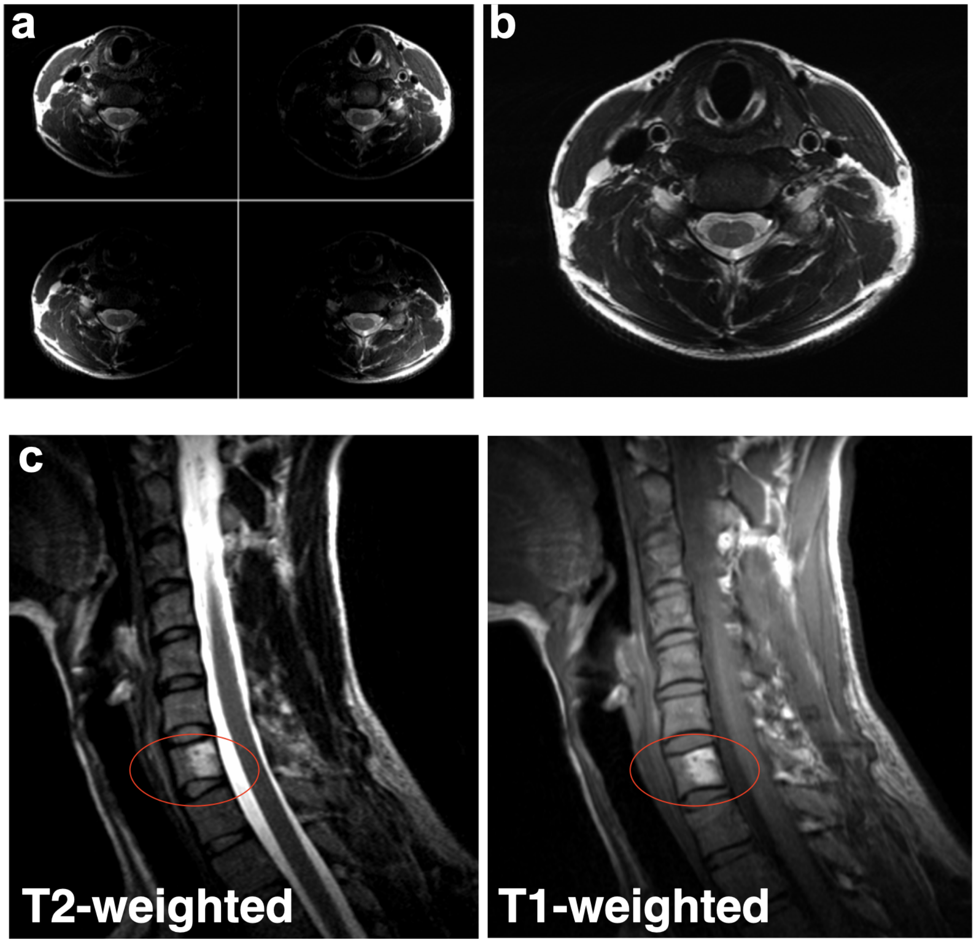

Figure 2.7: Imaging of the body parts relevant for clinical applications. (a) Images of the neck crossection taken by individual elements. (b) Combined image of the neck crossection. T2 (c) and T1 (d) weighted sagittal images of the spine of the volunteer with vertebral hemangioma (indicated with red line). Image reproduced from [25].

We used the 3D printed MRI coils described above for imaging the neck of a volunteer to demonstrate how they could be used in a clinical setting. The scanning was performed at UC Berkeley following an Institutional Review Board (IRB) approved protocol (2013-07-5491). Prior to the scan, informed consent was obtained from the subject for their participation. The subject also granted permission to publish data and photos from the scan. Figure 2.7a,b shows images of the neck cross-section taken by individual elements (a), as well as combined image (b). Each of the four elements contributes evenly to create a high-resolution image, with clearly differentiated anatomical features. Figure 2.7c,d shows the sagittal image of the spine of the volunteer with an incidental finding of vertebral hemangioma, a benign vascular tumor consisting primarily of blood vessels and fat tissue. T2-weighted images were acquired with a turbo spin echo (TSE) sequence with a repetition time (TR) of 3500ms, and an echo time (TE) of 104ms (Figure 2.7c). T1-weighted images were acquired with a TSE sequence with a TR of 700ms and TE of 10ms (Figure 2.7d). The short TR and TE result in an intrinsic T1 weighting since spins with a longer T1 do not fully recover before the next RF pulse. Different tissues are characterized by different intensity of T1 and T2 weighted images. Fat tissue shows increased signal intensity on T1-weighted images, while blood appears brighter on T2-weighted images. Since hemangioma has high content of both fat and blood - it appears bright on both T1 and T2-weighted images, as shown in Figure 2.7c,d.

2.3 Methods

2.3.1 Coil Fabrication

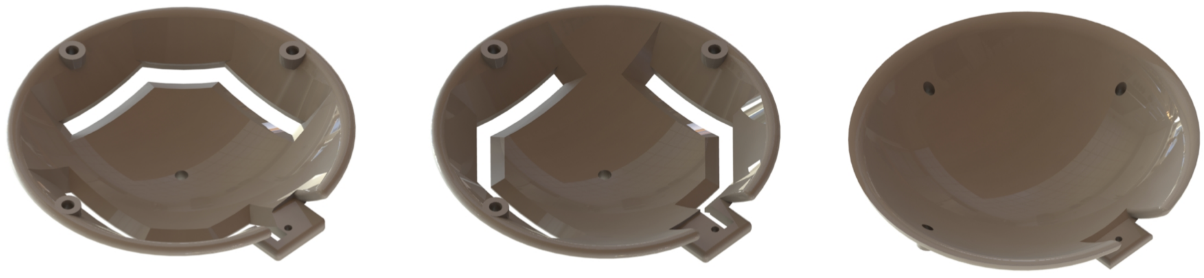

Figure 2.8: CAD drawings of the spherical substrate and masks printed along with the substrate to define the geometry of the conductor traces. Image reproduced from [25].

Coils were produced by sequentially spray-depositing coil components onto a 3D printed substrate. The substrate of cyanate ester resin (Carbon) was printed along with masks defining the geometry of the conductor traces (Figure 2.8) using a digital light synthesis (DLS) 3D printer (Carbon). The conductive traces were produced by spray-depositing an aqueous silver conductive ink (Novacentrix PSPI 0250/1000) onto a 3D printed substrate in the MRI coil trace pattern using a 3D printed mask. Subsequently, the metal layer was annealed at 100°C for 30 minutes. The dielectric layer was then deposited onto the substrate, evenly coating the entire surface. Finally, the surface metal layer was spray deposited on top of the dielectric layer with an alternate 3D printed mask. Each sprayed silver layer took approximately five minutes to apply by hand. The dielectric layer was applied with an automated spray coating machine for about three hours. To fabricate a custom array, a pair of two-coil elements was printed onto the substrate covering the entire neck surface area. Rigid printed circuit boards (PCB) with Q-spoiling circuitry were attached to each coil with plastic screws (McMaster-Carr) as shown in Figure 2.2d. An electrical connection was formed by direct contact between the copper on the PCB and the silver traces. The Q-spoiling circuit consisted of an inductor and PIN diode. When biased, the diode creates a resonant loop between the matching capacitor and the inductor creating a high impedance at the port of the coil [5, 31]. This is used to detune the coil and protect the receiver circuitry during the transmit phase of an MR sequence. A three-quarter wavelength non-magnetic RG316 cable (Alpha Wire) with a BNC connector (Amphenol) was soldered directly to the PCB. The cost of the four-channel array (without the preamplifiers) was approximately $200, including the 3D printed substrate and rigid components.

2.3.2 Characterization of the Coil Components

Dielectric properties of PS, SBR and PEEK were characterized by measuring Q unloaded of the coils fabricated with the corresponding dielectric as described below. PEEK film was purchased from Professional Plastics, PS and SBR films were deposited from solution. A 4% weight polystyrene (Sigma Aldrich, MW 200,000 by GPC) solution in toluene (Sigma Aldrich, anhydrous 99.8%) was used to deposit polystyrene dielectric film. Premade aqueous SBR solution (EQ-Lib-SBR) was purchased from MTI corporation for making SBR dielectric. The corresponding solution was deposited onto 70 μm-thick copper foils cut into the shape of the MRI traces using a custom-built three axis stage fitted with an airbrush (Badger 350-4) set at 15 psi. The airbrush was repeatedly passed over the copper patterns, until 60 μm thickness of dielectric was deposited. During SBR deposition process copper traces were attached to a hot plate to maintain a surface temperature of 100°C. Polystyrene films were deposited onto the surface at room temperature. The resulting film thicknesses were measured with a micrometer (Mitutoyo) after evaporating any remaining solvent (12hrs at room temperature for the polystyrene, 30 min at 100°C for SBR). To assemble the complete coil, another bare copper foil trace was placed over the aforementioned traces, creating a closed inductive loop with a total of 4 capacitors. The completed coil was then sandwiched between two sheets of MRI transparent acrylic to regulate pressure on each capacitor across different tests. To determine the optimum curing time and temperature for the silver nanoparticle ink (Figure 2.4a) 0.5 cm by 4 cm strips of the ink were sprayed onto a PET substrate until a film of 40μm was deposited. A four-point probe was used to measure the initial resistivity of the samples in three different positions 1cm apart from each other. The samples were then dried at 60°C, 80°C and 100°C with the resistivity measured periodically until no change was observed. The conductor thickness was optimized by fabricating coils with varying silver trace thicknesses on planar substrates (Figure 2.4c). The unloaded Q was measured for each sample and the silver thickness was chosen based on the point of diminishing returns due to the skin depth effect of alternating currents.

2.3.3 Coil Characterization

All coils were tested with an Agilent E5061B ENA network analyzer. To measure Q unloaded, each coil was calibrated to the correct resonance frequency of 123.3 MHz by varying capacitor areas. Capacitor area was changed by gently removing material from the top conductive trace. Two broadband loops were placed 30cm apart to minimize the S21 noise floor. Then, the coil was placed in between the probes. Extra caution was taken to remove any conductive material from the testing zone to avoid risk of unintentionally loading the coil. Unloaded Q was measured from the S21 response by dividing the center frequency by the -3dB bandwidth at a span of 25 MHz. Coils were matched to an input impedance of 50 ohms by adjusting the value of the matching capacitor while measuring S11 on a loading phantom. Preamp decoupling was tuned by adjusting the length of the coaxial cable by small increments while the preamps were powered and connected to the coil. Three inductively coupled cable traps were attached to each cable to reduce common mode currents on the shield of the coax.

2.3.4 Imaging

The SNR of the custom array was compared to that of the commercial array by imaging the conductive phantom on a 3T scanner (Siemens 3T Trio). The phantom consisted of the 3D printed casing in the shape of the patient's neck, containing a solution of 3.356 g l -1 NiCl2 * 6H2O and 2.4 g l - 1 NaCl for conductivity of 0.68 Sm -1 at 123 -127 MHz. Each coil was connected to a 4-channel interface box (Stark Contrast, Erlangen, Germany) containing low noise preamplifiers. The custom coil array was stress tested with a one hour long, high SAR turbo spin echo pulse sequence. After the scan, the entire apparatus was removed from the scanner and immediately imaged with a thermal camera (FLIR Systems, Wilsonville OR) to ensure that the temperature of components that might contact a subject did not rise more than 15°C above ambient, as required by our IRB approved protocol. SNR maps were derived from a 2D gradient echo sequence with an echo time (TE) of 10ms, repetition time (TR) of 438ms, a flip angle of 25°, a resolution of 0.8 x 0.8 x 5 mm^3, and a bandwidth of 260 Hz/pixel. Noise scans were acquired by running the same scan with the transmit voltage set to 0V. Image analysis was conducted on the raw data files from the scanner. SNR maps were calculated in absolute units with methods described by Kellman et al[32] using noise pre-whitening and optimal coil combination. To scan a volunteer the custom array was placed on the neck. Axial and sagittal T1 weighted images of the neck were taken with a turbo spin echo sequence (TE: 10ms, TR: 700ms, ETL: 5, Res: 0.6 x 0.8 x 3 mm^3) with an inherent T1 weighting due to the short TR. In addition, axial and sagittal T2 weighted images of the neck were acquired with a turbo spin echo sequence (TE: 104ms, TR: 3500ms, ETL: 5, Res: 0.6 x 0.8 x 3 mm^3).

2.4 Discussion

We present the first 3D MRI patient specific sprayed coils fabricated via additive manufacturing approaches. In spite of the higher resistivity and dielectric loss of solution-processed materials, custom printed coil arrays that conformed to the neck yielded higher SNR than a commercially available coil array. This resulted in images with less graininess and more clearly differentiated tissue interfaces. A limitation of this study is that the comparison is done with non-conforming coils. While other commercial coils exist, we did not have access to them. We attribute most of the SNR gain to the proximity of the custom coil to the phantom and its smaller element size. In addition, some SNR differences could be caused by the fact that the commercial array was not tuned and matched specifically for the phantom that we used. Another possible limitation is that the effects of B1 were not compensated for in the SNR measurements. However, we did not notice significant intensity changes in body coil images taken with the custom array placed on the phantom, hence any apparent SNR difference due to B1 would be small. In addition, the blocking impedance of the q-spoiling circuits was greater than 400 ohms for all channels. For our coil area of 64 cm^2 the recommended blocking impedance to produce less than 1% level of artifacts is 358 ohms according to Kocharian et al[33]. The SNR image (Figure 2.5e) has inhomogeneities at the edges due to the high signal at the proximity of each pair of surface coils. Wang et al report that SNR drops off as a cubic function of distance from the coil[34]. SNR is also lower at the top and bottom since the sprayed coils do not cover those regions to allow the coil to split in half, as illustrated in Figure 2.5b. Despite the ability to easily deposit conductors and dielectric materials to form the coil elements, fine tuning and matching is still a laborious process. One benefit of the sprayed coil is that the capacitance can be adjusted by scraping away portions of the silver traces. This method is simpler and easier than repeatedly reworking fixed capacitors by soldering. The 3D custom coils could bring substantial value in applications where in addition to higher SNR and reproducible placement on the patient is important, such as MRI guided surgeries. Though our prototype coil was designed as a proof of concept for carotid imaging, we want to emphasize that our techniques could be extended to other body parts. The work presented here is a step towards a future where coil manufacturing could be fully automated. In addition, coils made with our methods could be designed with additional features to attach the coils to the scanner and restrict subject motion. At the same time, utilization of 3D printing and spray-deposition to fabricate the coil components allows rapid manufacturing of such coils. This manufacturing flow can be adapted to other automated deposition approaches such as extrusion or aerosol printing, further advancing widespread adoption of the approach.

Bibliography

[1] Yasser Khan, Aminy E Ostfeld, Claire M Lochner, Adrien Pierre, and Ana C Arias. Monitoring of vital signs with flexible and wearable medical devices. *Advanced materials*, 28(22):4373–4395, 2016.

[2] Hiroki Ota, Sam Emaminejad, Yuji Gao, Allan Zhao, Eric Wu, Samyuktha Challa, Kevin Chen, Hossain M Fahad, Amit K Jha, Daisuke Kiriya, et al. Application of 3d printing for smart objects with embedded electronic sensors and systems. *Advanced Materials Technologies*, 1(1):1600013, 2016.

[3] Yun-Soung Kim and Woon-Hong Yeo. Smart and connected bioelectronics for seamless health monitoring and persistent human-machine interfaces. In *International Symposium on Microelectronics*, volume 2018, pages 000660–000664. International Microelectronics Assembly and Packaging Society, 2018.

[4] Jianming Jin. *Electromagnetic analysis and design in magnetic resonance imaging*, volume 1. CRC press, 1998.

[5] Peter B Roemer, William A Edelstein, Cecil E Hayes, Steven P Souza, and Otward M Mueller. The nmr phased array. *Magnetic resonance in medicine*, 16(2):192–225, 1990.

[6] Steven M Wright. Full-wave analysis of planar radiofrequency coils and coil arrays with assumed current distribution. *Concepts in Magnetic Resonance: An Educational Journal*, 15(1):2–14, 2002.

[7] Joseph R Corea, Anita M Flynn, Balthazar Lechêne, Greig Scott, Galen D Reed, Peter J Shin, Michael Lustig, and Ana C Arias. Screen-printed flexible mri receive coils. *Nature communications*, 7(1):1–7, 2016.

[8] Joseph R Corea, P Balthazar Lechene, Michael Lustig, and Ana C Arias. Materials and methods for higher performance screen-printed flexible mri receive coils. *Magnetic resonance in medicine*, 78(2):775–783, 2017.

[9] Takayuki Kinoshita. *Non-surgical ablation therapy for early-stage breast cancer*. Springer, 2016.

[10] Ilana Schlesinger, Ayelet Eran, Alon Sinai, Ilana Erikh, Maria Nassar, Dorith Goldsher, and Menashe Zaaroor. Mri guided focused ultrasound thalamotomy for moderate-to-severe tremor in parkinson's disease. *Parkinson's disease*, 2015, 2015.

[11] Joseph Corea, Patrick Ye, Dongjin Seo, Kim Butts-Pauly, Ana Claudia Arias, and Michael Lustig. Printed receive coils with high acoustic transparency for magnetic resonance guided focused ultrasound. *Scientific reports*, 8(1):1–10, 2018.

[12] NC Nielsen, C Kehlet, SJ Glaser, and N Khaneja. Encyclopedia of magnetic resonance, 2010.

[13] Ana Claudia Arias, J Devin MacKenzie, Iain McCulloch, Jonathan Rivnay, and Alberto Salleo. Materials and applications for large area electronics: solution-based approaches. *Chemical reviews*, 110(1):3–24, 2010.

[14] Alejandro H Espera, John Ryan C Dizon, Qiyi Chen, and Rigoberto C Advincula. 3d-printing and advanced manufacturing for electronics. *Progress in Additive Manufacturing*, pages 1–23, 2019.

[15] Tuomas Happonen, Markus Tuomikoski, Tuomas Kokko, and Kari Ronka. Roll-to-roll functional testing of printed conductors and organic light emitting devices. In *2018 7th Electronic System-Integration Technology Conference (ESTC)*, pages 1–5. IEEE, 2018.

[16] Luc Darrasse and J-C Ginefri. Perspectives with cryogenic rf probes in biomedical mri. *Biochimie*, 85(9):915–937, 2003.

[17] BH Suits, AN Garroway, and JB Miller. Surface and gradiometer coils near a conducting body: the lift-off effect. *Journal of magnetic Resonance*, 135(2):373–379, 1998.

[18] Jurek A Nordmeyer-Massner, Nicola De Zanche, and Klaas P Pruessmann. Stretchable coil arrays: application to knee imaging under varying flexion angles. *Magnetic resonance in medicine*, 67(3):872–879, 2012.

[19] John A Malko, Eric C McClees, Ira F Braun, Patricia C Davis, and JC Hoffman. A flexible mercury-filled surface coil for mr imaging. *American journal of neuroradiology*, 7(2):246–247, 1986.

[20] Jean Rousseau, Pascal Lecouffe, and Xavier Marchandise. A new, fully versatile surface coil for mri. *Magnetic resonance imaging*, 8(4):517–523, 1990.

[21] Sajad Hosseinnezhadian, Roberta Frass-Kriegl, Sigrun Goluch-Roat, Michael Pichler, Jürgen Sieg, Martin Vít, Marie Poirier-Quinot, Luc Darrasse, Ewald Moser, Jean-Christophe Ginefri, et al. A flexible 12-channel transceiver array of transmission line resonators for 7 t mri. *Journal of Magnetic Resonance*, 296:47–59, 2018.

[22] Gregor Adriany, Pierre-Francois Van de Moortele, Johannes Ritter, Steen Moeller, Edward J Auerbach, Can Akgün, Carl J Snyder, Thomas Vaughan, and Kâmil Uğurbil. A geometrically adjustable 16-channel transmit/receive transmission line array for improved rf efficiency and parallel imaging performance at 7 tesla. *Magnetic Resonance in Medicine: An Official Journal of the International Society for Magnetic Resonance in Medicine*, 59(3):590–597, 2008.

[23] Bahareh Behzadnezhad, Bruce D Collick, Nader Behdad, and Alan B McMillan. Dielectric properties of 3d-printed materials for anatomy specific 3d-printed mri coils. *Journal of magnetic resonance*, 289:113–121, 2018.

[24] Dario Mager, Andreas Peter, Laura Del Tin, Elmar Fischer, Patrick J Smith, Jürgen Hennig, and Jan G Korvink. An mri receiver coil produced by inkjet printing directly on to a flexible substrate. *IEEE transactions on medical imaging*, 29(2):482–487, 2010.

[25] AM Zamarayeva, K Gopalan, JR Corea, MZ Liu, K Pang, M Lustig, and AC Arias. Custom, spray coated receive coils for magnetic resonance imaging. *Scientific Reports*, 11(1):1–9, 2021.

[26] Franz J Wippold. Head and neck imaging: the role of ct and mri. *Journal of Magnetic Resonance Imaging: An Official Journal of the International Society for Magnetic Resonance in Medicine*, 25(3):453–465, 2007.

[27] Marianne Eline Kooi, VC Cappendijk, KBJM Cleutjens, AGH Kessels, PJEHM Kitslaar, M Borgers, PM Frederik, MJAP Daemen, and JMA Van Engelshoven. Accumulation of ultrasmall superparamagnetic particles of iron oxide in human atherosclerotic plaques can be detected by in vivo magnetic resonance imaging. *Circulation*, 107(19): 2453–2458, 2003.

[28] Walter P Maksymowych, Praveena Chiowchanwisawakit, Tracey Clare, Susanne J Pedersen, Mikkel Østergaard, and Robert GW Lambert. Inflammatory lesions of the spine on magnetic resonance imaging predict the development of new syndesmophytes in ankylosing spondylitis: evidence of a relationship between inflammation and new bone formation. *Arthritis & Rheumatism*, 60(1):93–102, 2009.

[29] Masaru Honda, Naoki Kitagawa, Keisuke Tsutsumi, Izumi Nagata, Minoru Morikawa, and Tomayoshi Hayashi. High-resolution magnetic resonance imaging for detection of carotid plaques. *Neurosurgery*, 58(2):338–346, 2006.

[30] Thomas J Masaryk, MT Modic, PM Ruggieri, JS Ross, G Laub, GW Lenz, JA Tkach, EM Haacke, WR Selman, and SI Harik. Three-dimensional (volume) gradient-echo imaging of the carotid bifurcation: preliminary clinical experience. *Radiology*, 171(3): 801–806, 1989.

[31] Boris Keil, Vijay Alagappan, Azma Mareyam, Jennifer A McNab, Kyoko Fujimoto, Veneta Tountcheva, Christina Triantafyllou, Daniel D Dilks, Nancy Kanwisher, Weili Lin, et al. Size-optimized 32-channel brain arrays for 3 t pediatric imaging. *Magnetic Resonance in Medicine*, 66(6):1777–1787, 2011.

[32] Peter Kellman and Elliot R McVeigh. Image reconstruction in snr units: a general method for snr measurement. *Magnetic resonance in medicine*, 54(6):1439–1447, 2005.

[33] Armen Kocharian, Phillip J Rossman, Thomas C Hulshizer, Joel P Felmlee, and Stephen J Riederer. Determination of appropriate rf blocking impedance for mri surface coils and arrays. *Magnetic Resonance Materials in Physics, Biology and Medicine*, 10 (2):80–83, 2000.

[34] Jianmin Wang, Arne Reykowski, and Johannes Dickas. Calculation of the signal-to-noise ratio for simple surface coils and arrays of coils [magnetic resonance imaging]. *IEEE transactions on biomedical engineering*, 42(9):908–917, 1995.

Chapter 3

Vacuum Formed Receive Coils for Magnetic Resonance Imaging

3.1 Introduction

In the past several years, there has been an effort to make coils that conform to the body in order to improve patient comfort and increase SNR. Numerous groups have shown that bringing coils closer to the subject dramatically improves image quality[3, 13, 1]. Advances in additive manufacturing methods such as 3D printing have enabled new innovations for coil design and form factor. For example, Zhang et al. demonstrated a glove coil that couples a flexible mechanical design with a novel electronic circuit to capture high resolution images of hands in motion[14]. In addition, some groups have demonstrated new manufacturing techniques that should accelerate the coil fabrication process. For example, Corea et al. developed a process for screen printing conductive inks onto a flexible PEEK substrate to make MRI coils that conform to the subject[1]. Though the coil arrays required manual tuning and assembly, the conductive traces and tuning capacitors were printed with a fast and reproducible process. Another novel method for creating receive coils was described by Vincent and Rispoli[11]. The authors used a desktop sewing machine to create an MRI coil that could stretch in multiple directions by sewing conductive threads into stretchable athletic fabric. Despite a decrease in SNR compared to conventional coils, the stretchable coils could conform to almost any body part and the manufacturing method was fast and scalable.

Many recent innovations in receive coil development have focused on flexible coils that can conform to the body. However, flexible coils may be limited when placed on complex curved surfaces like the back of the head or neck. Our prior work patterning coil geometries on rigid 3D printed substrates showed that a form fitting coil can improve image quality by bringing the coils as close as possible to highly curved anatomy[13]. In addition, Keil et al. showed that placing a subject in an closely fitting head coil resulted in a dramatic improvement in peripheral SNR[3]. The authors developed five 32 channel receive coil arrays for different age groups using conventional coil construction methods. Their work showed the benefits of tailoring the coils to the body and choosing the correct coil size for the subject. However, conventional coil manufacturing methods are time consuming and require a skilled RF engineer. It is currently not practical or cost effective to have a wide range of coil sizes at every scanner site. In order to improve the speed of manufacturing, we developed a method to deposit coil traces on curved plastic substrates using a combination of vacuum forming, sandblasting, and electroless copper plating.

Vacuum forming is an industrial process where a plastic sheet is heated beyond its glass transition temperature and pulled over a mold. Once the plastic makes contact, a vacuum force is applied to force the sheet to conform to the contours of the mold. We use vacuum forming to create MRI coil arrays that are in close proximity to specific body parts by making molds from digital MRI scans or 3D scans. To fabricate a coil array, we start with a plastic sheet that is prepared with a sandblasted pattern of the desired coil layout. Sandblasting uses air pressure to etch a surface by bombarding it with abrasive material like sand, glass beads, or metal particles. The patterned sheet is then sensitized with a palladium-tin catalyst and vacuum formed into the shape of a target anatomical structure. The formed plastic is copper plated, and electronic components like inductors, capacitors, and diodes are attached to make functional receive coils. To demonstrate our methods, we built and tested an 8 channel coil array to image the visual cortex. Since vacuum forming stretches a flat sheet into a 3D object it was not possible to uniformly pattern the coil layout. In order to account for the deformation inherent to vacuum forming, we designed a simulation of the vacuum forming process in C++. The simulation compensates for the distortion and stretching and generates a predistorted pattern that attempts to minimize areal distortion on the final 3D surface. We also developed a method to validate and correct the simulation by printing a grid on a plastic sheet, vacuum forming it to a known 3D model, and 3D scanning the grid. With our methods, it is possible to make dense three dimensional conductor designs and pattern traces over complex curved surfaces.

3.2 Methods

The process flow for creating a vacuum formed MRI receive coil array starts with a 3D scan of a specific body part. The scan is used to prepare a layout of coil geometries with custom built vacuum forming simulation software. Next, the 3D model is turned into a mold by CNC milling a negative of the model out of foam and filling the negative with gypsum cement. A flat plastic sheet is then covered in a tape mask and the predistorted coil geometries are cut out with a laser cutter (Figure 3.1A). Next, the exposed areas of the plastic are sandblasted, cleaned, and catalyzed for copper plating (Figure 3.1B,C). The mask is removed and the flat plastic sheet is vacuum formed into the shape of the mold (Figure 3.1D). After vacuum forming, the 3D plastic substrate is removed from the mold and place into a copper plating tank (Figure 3.1E). The copper traces are then tin plated to make them more stable in open air. Electronic components are used to connect the traces and form functional MRI receive

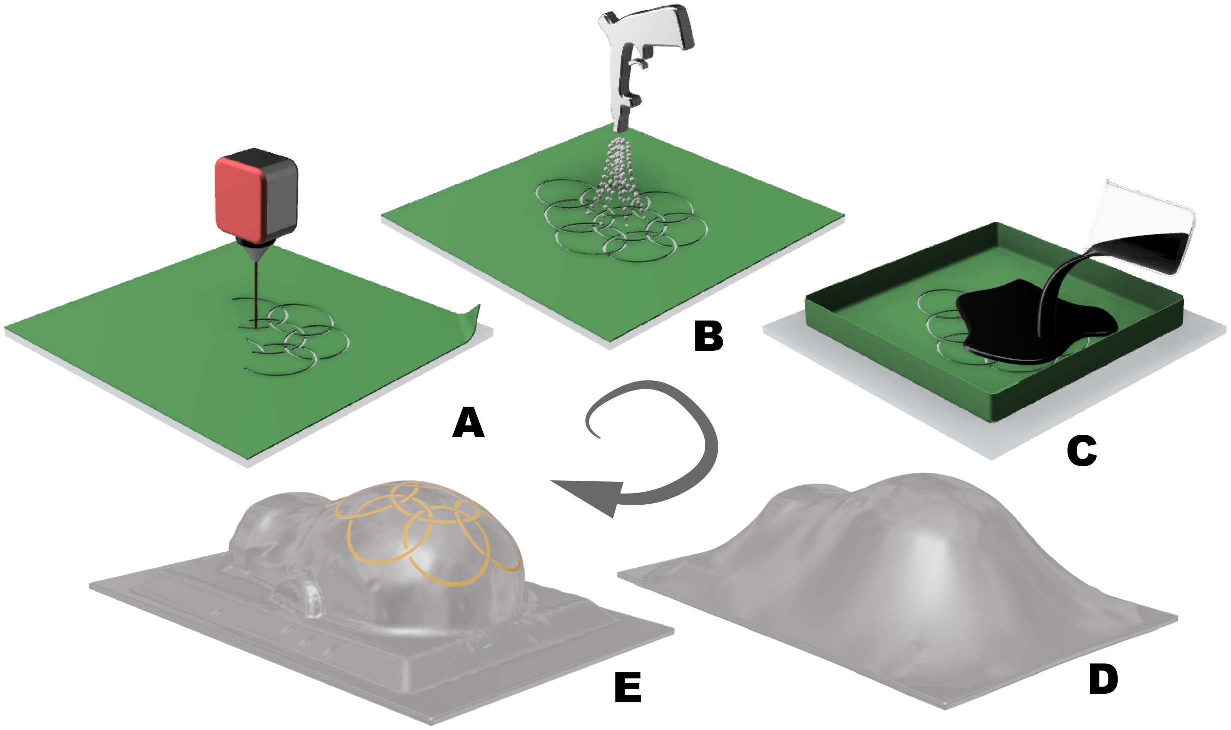

Figure 3.1: A) A polycarbonate sheet is masked with polyester tape and the pre distorted coil pattern is cut out of the mask with a CO2 laser. B) The sheet is sandblasted with 100 grit white fused aluminum oxide. C) After cleaning, the exposed areas are catalyzed with a palladium-tin solution. D) The mask is removed, and the sheet is vacuum formed. E) The vacuum formed plastic is removed from the mold and copper plated in an aqueous solution of copper sulfate, EDTA, sodium hydroxide, and formaldehyde.

coils.

3.2.1 Vacuum Forming Simulation

In order to predict the deformation inherent to vacuum forming, we developed a graphical simulation in C++ using OpenGL. Our simulation models the plastic as a discrete network of point masses and springs. The point masses are connected with edges in order to triangulate the surface. Collisions for arbitrary objects, including the build platform and mold, are handled with the Embree ray tracing kernel[12]. The initial state of the simulation is shown in Figure 3.2A. The figure shows a digital plastic sheet raised over a mold to be vacuum formed. The modeled plastic sheet is lowered over a 3D model as shown in Figure 3.2B. We assume that the plastic experiences infinite friction when it collides with the mold [15] and will stick to the surface. In Figure 3.2C, the sheet makes contact with the base of the vacuum

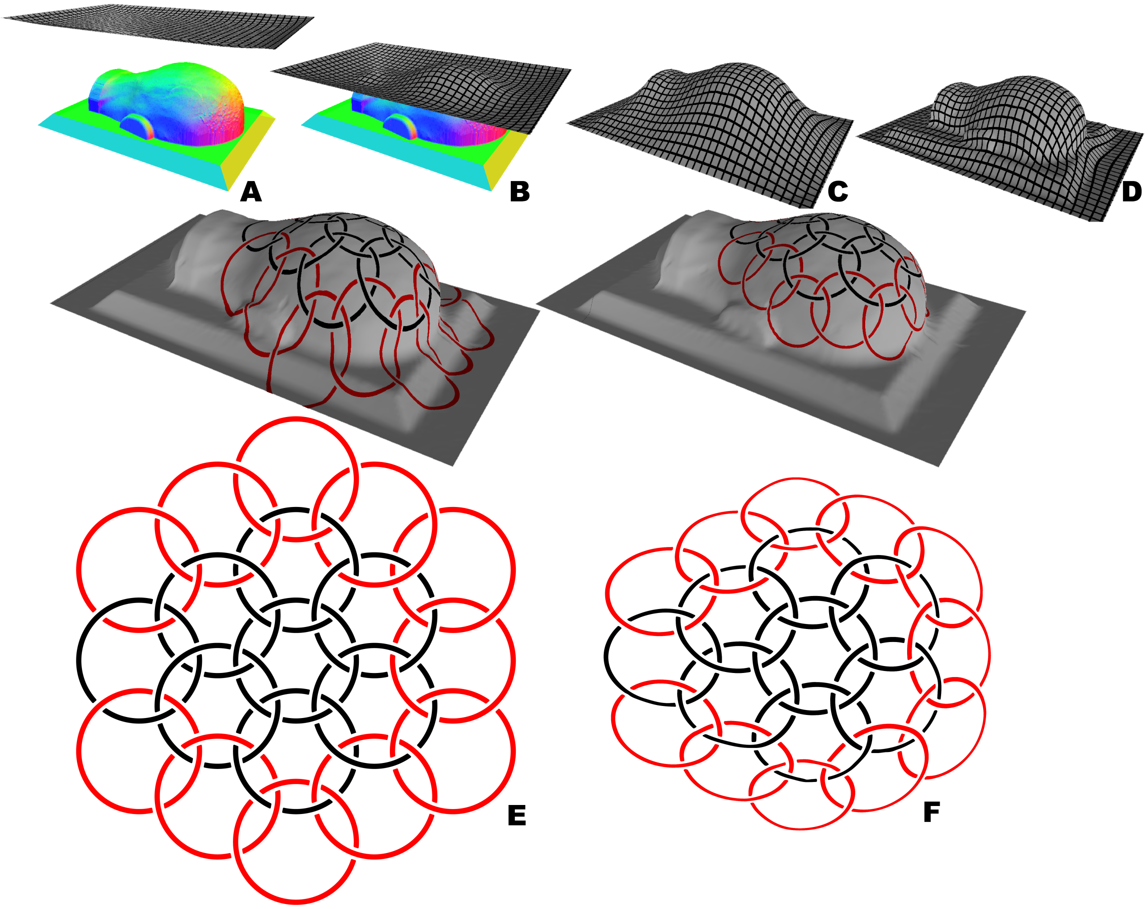

Figure 3.2: Example of the vacuum forming simulation with a head model. A) The initial state of the simulation. B) The plastic sheet starts to intersect the model. C) The sheet then intersects the base before a vacuum force is applied. D) The final state of the simulation after the vacuum force is applied and all points of the sheet are stuck to the model. E) The 2D undistorted coil array design and the result of naively applying it before vacuum forming. Out of the 19 elements shown, the eight black channels were used for our prototype coil array. F) The predistorted design created with an ARAP planar parameterization produces coils with less deformation.

former and vacuum is applied to force the plastic to conform to the mold. Figure 3.2D shows the final state of the simulation when the entire sheet has made contact with the mold or the platform. The vacuum force (F_{vac}) is modeled as a force proportional to the area (A) of each triangle and a user defined constant p applied along the normal ($\hat{n}$) vector of the triangle, as shown in Equation 3.1.

$$F_{vac} = -pA\hat{n} \tag{3.1}$$

We also integrated portions of the computational geometry algorithms library (CGAL) to perform an as rigid as possible (ARAP) planar parameterization of the deformed plastic sheet [5, 8]. The parameterization allows the user to provide a 2D image of an undistorted design and get a predistorted image that attempts to minimize areal distortion when applied to the 3D model. An example of a distorted pattern created with this method is shown in Figure 3.2E,F. The figures show that uniformly patterned coil geometry stretches undesirably after vacuum forming while the predistorted pattern creates more reasonable loops on the 3D model.

3.2.2 Simulation Verification

In order to verify the deformation simulation, we printed a grid on a polycarbonate sheet with a Sharpie marker attached to our CNC milling machine (Figure 3.3A). Before drawing the grid, the sheet was sandblasted in order to provide a non reflective surface. Reflections from the plastic interfere with the photogrammetry software and introduce errors in the 3D reconstruction. The gridded sheet was then vacuum formed to a head shaped mold and the formed plastic was imaged with a cell phone camera from multiple angles. An example image is shown in Figure 3.3B. The images were uploaded to a cloud based photogrammetry software (Autodesk Recap) to generate a digital 3D model (Figure 3.3C). The texture map is then extracted from the 3D model and displayed with Cairo, a 2D graphics library (Figure 3.3D). A low pass filter is applied to the texture and the grid is reconstructed by labeling the contours of the deformed white squares with OpenCV. The labelling is shown in Figure 3.3E. The centroids of the labeled boundaries are connected to form a mesh which corresponds to the final position of the uniformly patterned grid after vacuum forming (Figure 3.3F). This connected mesh is uniformly scaled, rotated, and translated to be as close as possible to the simulated mesh by minimizing the euclidean distance between simulated and experimentally measured points. Grid points that were obscured by noise were ignored.

3.2.3 Electromagnetic Simulation

In addition to the mechanical simulation, electromagnetic simulations were used to determine the electrical performance of the vacuum formed coils. Closely placed MRI receiver coils couple inductively, reducing the array's sensitivity at the desired resonant frequency [7]. This effect can be mitigated by adjusting the overlap between neighboring coils in order to

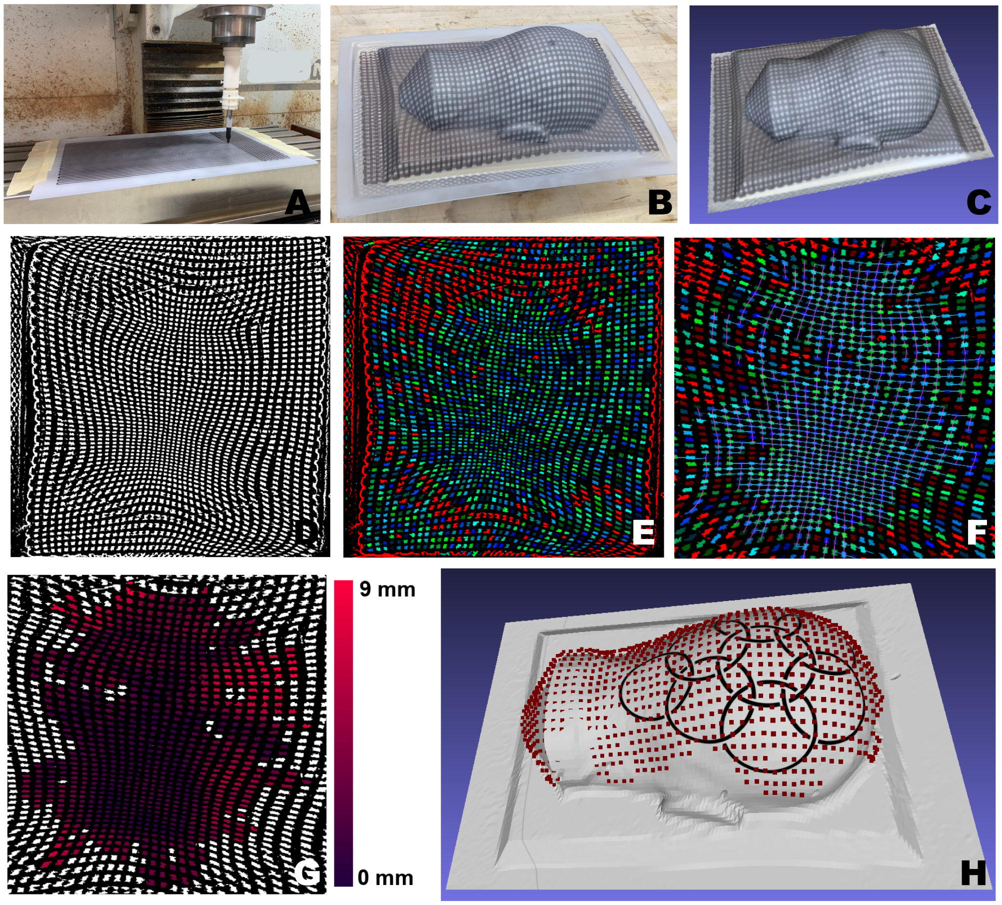

Figure 3.3: Simulation Verification. A) Printing a grid on a flat polycarbonate sheet with our CNC milling machine. B) A single image of the vacuum formed plastic to be used for photogrammetry. C) Reconstructed 3D model of the vacuum formed plastic with grid lines. D) Flattened model texture. E) Texture with labeled contours. Red indicates shapes which are filtered out due to being non-rectangular, and the remaining rectangles are colored a random mixture of blue and green to distinguish them from each other. F) Re-forming the grid from adjacent rectangles, blue/purple lines indicate correct grid lines. G) Relative error of squares where connectivity succeeded, darker purple indicates lower error while brighter red indicates higher error. Error was not calculated for the white squares due to the noise of the scan. H) 3D reconstruction of scanned grid points shown in red and overlayed on a simulated model of a vacuum formed sheet.

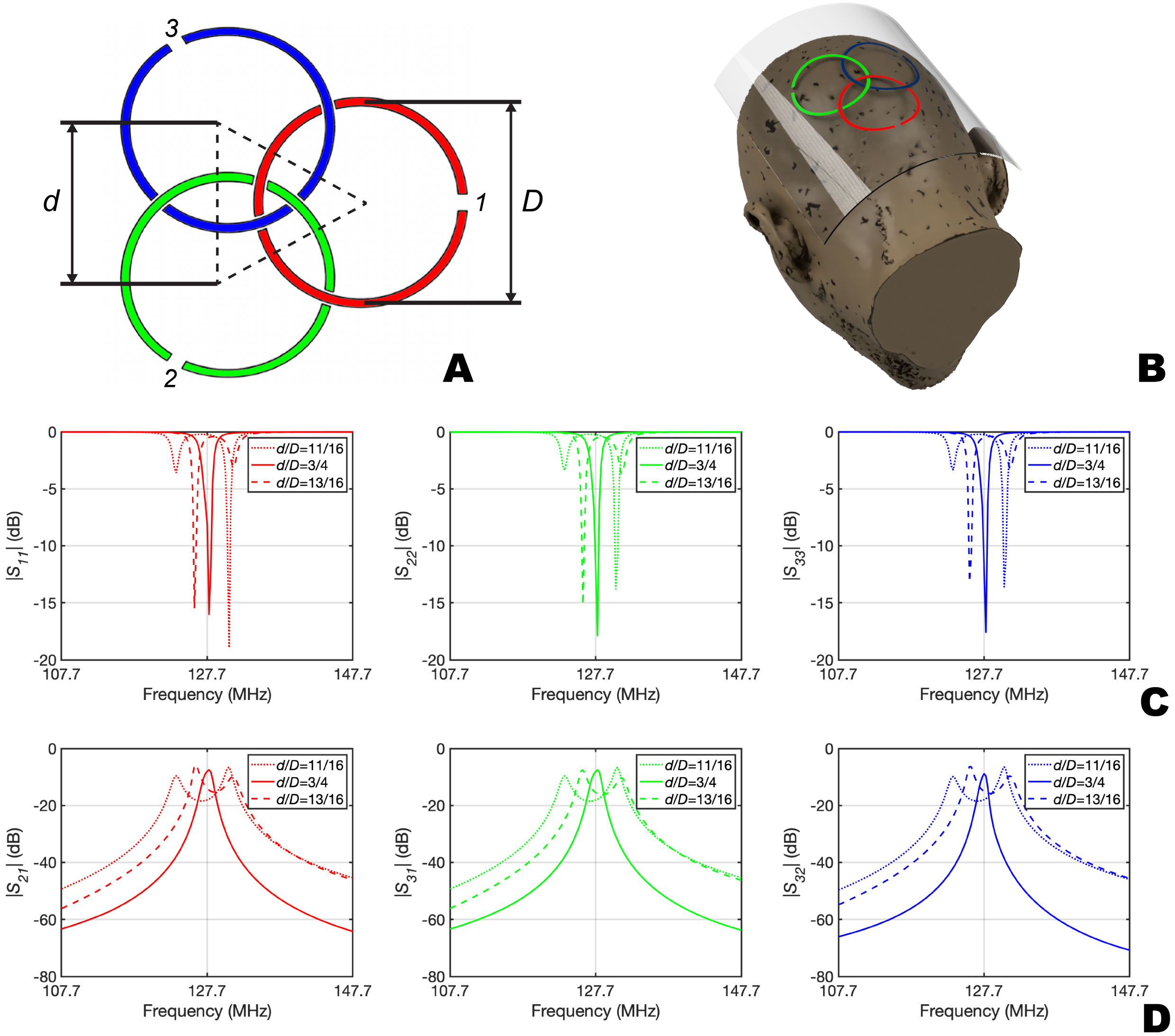

Figure 3.4: Geometric Decoupling Simulation. A) Tri-Coil pattern used in HFSS/ADS simulation. The ratio of the distance between the coils and the diameter of the coils was used to classify the overlap between the elements. Excitations were assigned to ports 1, 2, and 3 in HFSS. Those results were placed into ADS for tuning and matching. B) 3D model of Tri-Coil pattern on a curvilinear surface. This surface was used to mimic the back of the head. C) Return loss for each coil. The optimal return loss is achieved when the ratio of overlap to diameter is approximately 3/4's. D) Coupling between the coils for each pair. When the overlap to diameter ratio is approximately 3/4's the coupling between the coils is minimized and no resonant splitting occurs.

minimize the mutual inductance. To determine the critical overlap on a complex vacuum formed surface, the aid of an electromagnetic simulation software (HFSS, Ansys Inc.) in combination with electronic design automation software (ADS, Keysight Technologies) was used to optimize coil placement.

A Tri-Coil layout (Figure 3.4A) was used to model the eight-channel coil pattern used for the head array. This layout provides enough information to determine the overlap need between elements for a larger scale array. The Tri-Coil pattern was wrapped on a curved surface to mimic the shape of the back of a head (Figure 3.4B). Coil placement is classified by the ratio of the overlap distance to the diameter of the coil (d/D). Multiple simulations were executed by varying the distance between coils until the mutual inductance was minimized. When d/D is approximately 3/4's, the coupling between the elements was minimized (Figure 3.4C,D). This simulation can be applied to many curvilinear surfaces. This simulation method could be used to characterize the decoupling performance of different vacuum formed coils.

3.2.4 Mold Preparation

Mold standard tesslation language (STL) files are prepared from 3D MR scans using surface reconstruction tools in Horos. These files are edited with Autodesk Meshmixer in order to remove internal geometry like the brain and skull. The visible faces are first selected with a brush tool and the selection set is inverted to delete the unwanted parts of the model. The remaining surface is smoothed with the RobustSmooth brush to reduce the layering artifacts from the surface reconstruction. An example of a finished head model is shown in Figure 3.5A. Next, a machining toolpath is designed with Autodesk Fusion 360 and the negative of the digital models are cut out of laminated insulating foam (Foamular 150, Owens Corning) with a Tormach 1100M milling machine (Figure 3.5B). We used a six inch long, quarter inch diameter carbide ball end mill. The foam block is made by laminating sheets with a thin layer of Gorilla Glue and clamping overnight. After milling, we pour Perfect Cast casting material into the negative along with two bolts and a brass tube running to the top of the mold for blowing compressed air after vacuum forming (Figure 3.5C). The bolts are used to mount the gypsum mold to a wooden support. We also experimented with making positive molds out of wood and aluminum but the gypsum and foam were more cost effective for larger models.

3.2.5 Substrate Preparation

A polycarbonate sheet (TAP Plastics, El Cerrito, CA) is dried overnight in an oven set to 110°C to prevent absorbed moisture from creating bubbles and surface imperfections during the vacuum forming process. Two layers of 90 μm (3.5 mil) polyester powder coating masking tape (Advanced Polymer Tape, Toronto, Canada) are applied to the plastic sheet with a rubber roller. A pattern is then cut out of the tape with a CO_2 laser (Universal Laser Systems, Scottsdale, AZ). Next, the exposed areas of the plastic are sandblasted with

100 grit white fused aluminum oxide blasting media (Industrial Supply, Twin Falls, ID). Sandblasting is used to increase the surface area of the plastic and is essential for copper adhesion. The substrate is then cleaned with deionized (DI) water and Alconox cleaner. The substrate is then treated with a 1% aqueous solution of benzalkonium chloride which is a cationic surfactant used to improve the adhesion of the catalyst. After rinsing, the edges of the tape are peeled upwards to make a small reservoir around the laser cut mask. This method is used to reduce the amount of copper plating catalyst solution required. The catalyst is prepared by adding 60 mL of 37% hydrochloric acid (HCl) and 0.25 g palladium chloride ($PdCl_2$) to 1 liter of DI water. 12 g of tin chloride ($SnCl_2$) is added when the palladium salt completely dissolves and the solution is ready after one hour of stirring at 40-50°C [6]. The catalyst can be prepared and stored until the salts crash out of solution. The catalyst is then poured into the tape reservoir and allowed to sit for 10 minutes.

3.2.6 Vacuum Forming

After catalyzing, the substrate is rinsed in deionized water and the tape mask is removed. The polycarbonate is vacuum formed over a mold of the desired geometry with a Formech 300XQ vacuum former. The vacuum forming machine has five heating zones consisting of a large element in the center and four elements on the edges. We found that setting the central element to 70% and the others to the maximum reduced vacuum forming artifacts such as wrinkles and folds near the corners of the mold. The substrate is heated for approximately 120 seconds until it drooped uniformly in the center. Next, the mold is raised into the soft substrate and a vacuum is pulled simultaneously until the substrate makes complete contact with the mold.

3.2.7 Electroless Plating

After vacuum forming, the mold is removed and the edges of the plastic are cut with a band-saw to prepare for copper plating. The copper plating solution is prepared with 18 g/L copper sulfate pentahydrate ($CuSO_4 \cdot 5H_2O$), 48 g/L ethylenediaminetetraacetic acid (EDTA), 57.3 mg/L potassium ferrocyanide ($K_4[Fe(CN)_6]$), and 1 mL/L concentrated 37% hydrochloric acid (HCl) [2]. The EDTA is a complexing agent that binds with the copper ions to make them more soluble in water. The potassium ferrocyanide is a safe chemical that brightens the copper deposits by promoting a smaller copper grain size and slightly reducing the plating rate[10]. The HCl is used to increase the amount of chloride ions in the solution which modulates the plating rate. Sodium hydroxide (NaOH) is used to raise the pH to 12.8 and 22.5 mL/L of 37% formaldehyde (HCHO) is added as a reducing agent just before plating. We also built a plating tank (Figure 3.6A) including a fourteen liter polypropylene tank, a plastic circulation pump, a 25 micron filter bag, and a plywood support structure. The vacuum formed part is submerged in the plating tank with vigorous nitrogen bubbling. The nitrogen displaces the dissolved oxygen in the bath to prevent the formation of copper oxides. In addition, the agitation from the bubbling helps dislodge hydrogen gas bubbles created

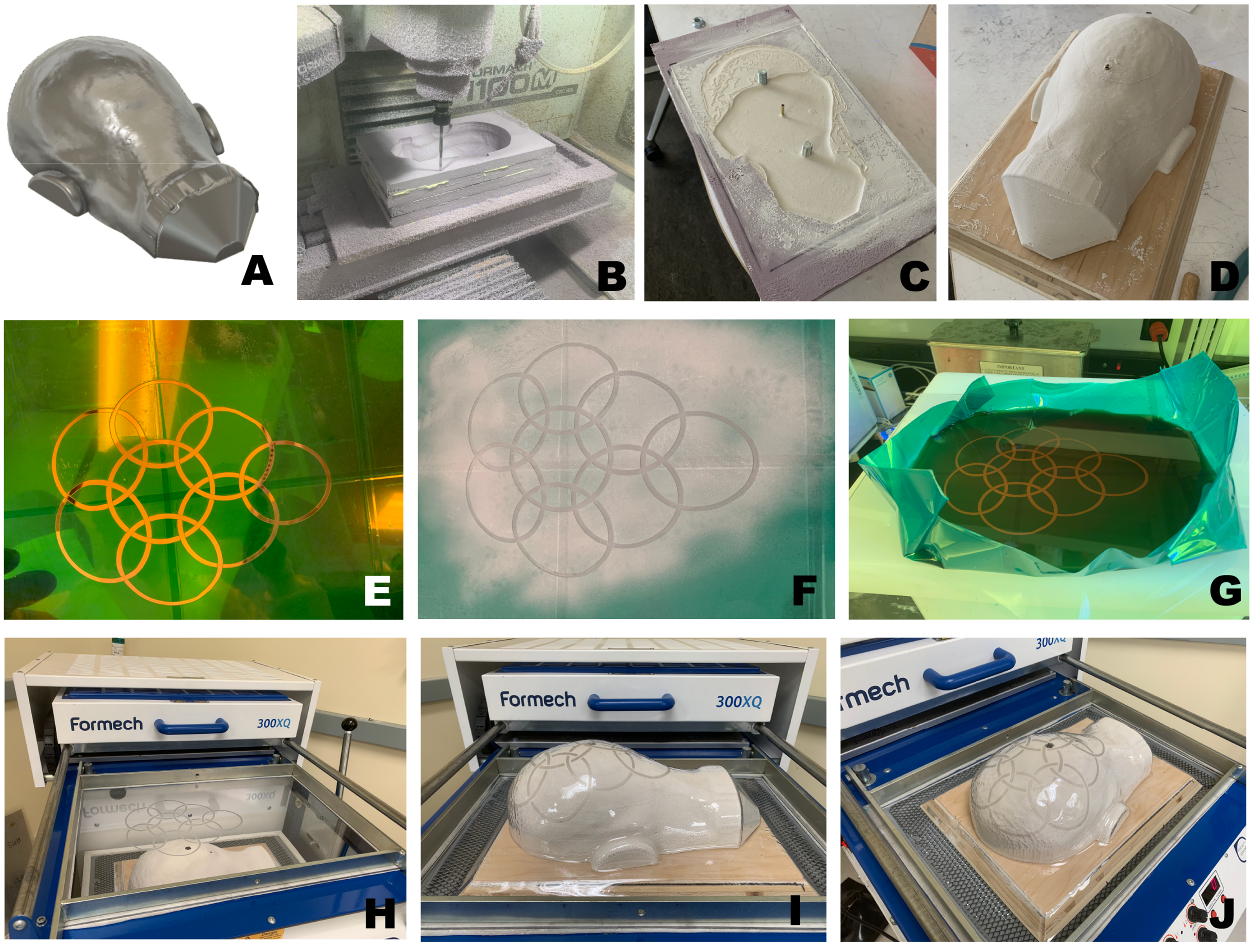

Figure 3.5: The physical process steps of creating our 8 channel visual cortex coil. A) A digital model of the back of a subjects head is created from 3D MRI scan data. B) The negative of the head mold is milled out of insulating foam with a CNC milling machine. C) Casting plaster is cast into the foam. D) The foam is removed and the cast mold is attached to a wooden support. E) A predistorted coil layout is laser cut out of a tape mask. F) The design is sandblasted into a polycarbonate sheet. G) After cleaning, a catalyst is poured into a well made out of the tape. H,I,J) The tape mask is removed and the catalyzed plastic is vacuum formed over the head shaped mold.

Figure 3.6: Electroless plating with a smaller sample. A) Our electroless copper plating setup including a polypropylene tank, circulation pump, filter bag, and nitrogen line. B) A small vacuum formed sample after copper plating to showcase the capabilities of our method. C) Demonstration of soldering a resistor to the plated copper traces.

from the plating reaction. The plating is performed at room temperature. We measured a plating rate of 5 μm per hour by plating on a smooth polycarbonate sheet, removing the copper, and measuring the film thickness with a Mitutoyo 293-340-30 micrometer with an accuracy of 1 micron. We were able to choose the plating time of our coils by relying on the skin effect which states that RF currents run on the surface of conductors. We plated our 127 MHz coils for five hours to ensure that all conductive areas had a thickness of at least three skin depths ($\sigma = 5.79\mu m$). An example of a plated sample is shown in Figure 3.6B. Using our technique, we are able to pattern conductors on complex three dimensional surfaces. Soldering is also possible (Figure 3.6C) if care is taken not to melt the polycarbonate. We also use an immersion tin plating solution to passivate the surface of the copper. The aqueous solution is composed of 4 g/L tin chloride ($SnCl_2$), 50 g/L thiourea, and 12 mL/L sulphuric acid (H_2SO_4). The solution is heated to 90°C and the copper traces are submerged for approximately 30 seconds to coat them in tin.

3.2.8 Coil Tuning and Matching

After the copper traces are patterned on the substrate, the gaps between the traces are connected with flexible PCBs (PCBWay, Shenzhen, China) that have pads for soldering rigid tuning capacitors. We then solder another flexible board that contains matching and q-spoiling circuitry to each channel. The coil elements are completed by attaching electronic components according to the circuit diagram in Figure 3.7A. This topology uses a tuning capacitor for q-spoiling since the lower capacitance provides a higher blocking impedance. We use 1111 non-magnetic capacitors (Passive Plus, Huntington, NY), ceramic chip inductors (Coilcraft, Cary, IL), and non-magnetic RF PIN diodes (Macom MA4P7470F-1072T, Lowel, MA). The loop is first tuned by measuring with a lightly coupled double probe and adjusting the tuning capacitors C_t until the resonance is close to 127.7MHz. Next, the coil is connected directly to the network analyzer through a half wavelength RG316 cable and the matching capacitor C_m is adjusted to match the impedance to 50Ω (Figure 3.7B). The coil is then connected to a 16 channel preamplifier box (Clinical MR Solutions, Brookfield, WI) and the output of one channel is connected to one port of the network analyzer. The coil is then probed with a pickup loop connected to the other port of the network analyzer. The measurement setup is illustrated in Figure 3.7A. L_{pre} is adjusted to resonate with C_m and the cable length is reduced until the observed dip from preamplifier decoupling is centered around the Larmor frequency as shown in Figure 3.7C. A bias-T is used to protect the analyzer and apply a 5V DC signal to turn on the PIN diode through the output of the preamplifier. Finally, the inductor L_Q is adjusted until the received signal is in the noise floor at the desired resonant frequency as shown by the red trace in Figure 3.7C.

Subsequent elements are tuned independently by detuning all of the other channels with the PIN diodes turned on or one tuning capacitor removed.

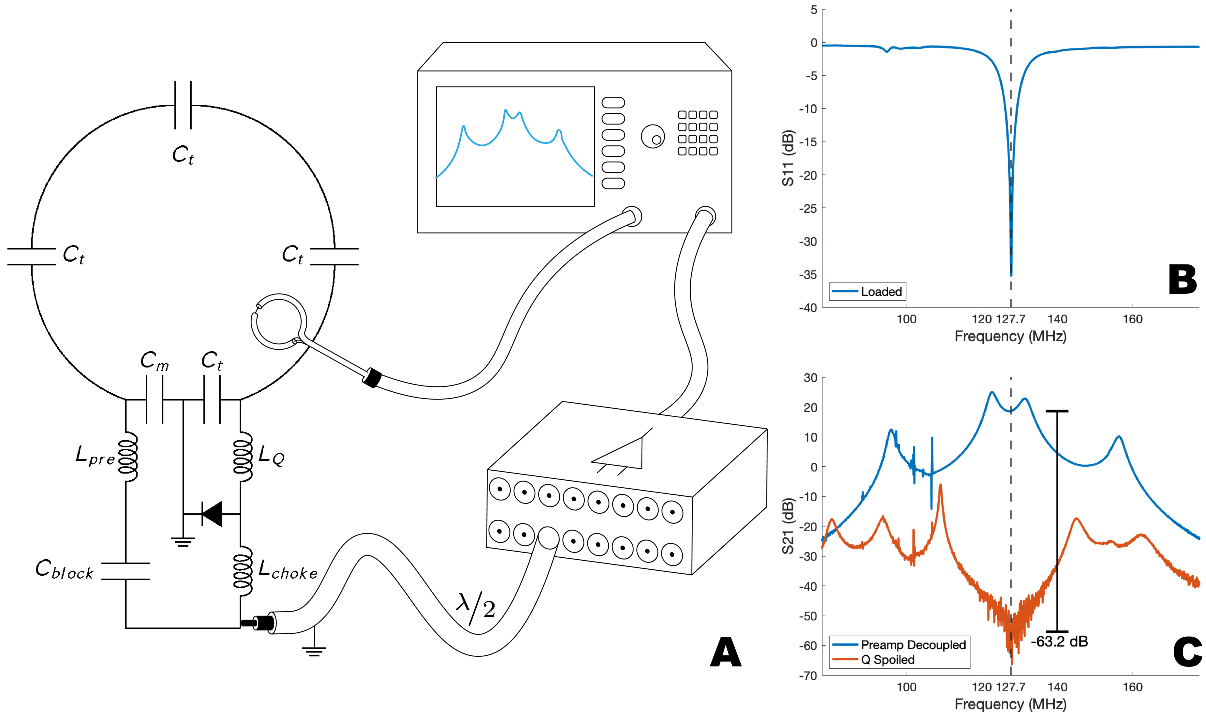

Figure 3.7: A) The circuit diagram of a single channel with Q-spoiling and matching circuitry. The coil is connected to a 16 channel pre-amplifier box and measured with a network analyzer. B) The S11 measurement of a tuned and matched coil connected directly to the network analyzer. C) Measurements of the coil when connected to the preamplifier. The red trace shows the detuned state when the PIN diode is biased.

3.2.9 Cable Traps

We designed and built inline traps to suppress common mode currents on the shields of the coaxial cables. The inline traps are made by winding the coax around a PCB former as shown in Figure 3.8A,B. The shield is then exposed on both sides of the winding by removing the jacket with a curved scalpel blade. The exposed shields are soldered to pads on the PCB and a capacitor is soldered across the winding to form a resonant circuit (Figure 3.8C). The traps are shielded by wrapping a 3D printed shell with copper tape (Figure 3.8D). These parts are made with clear resin with a Formlabs Form 2 3D printer. The devices with the shields are tuned to 127.7MHz over a large ground plane with an Agilent Technologies E5061A network analyzer (Figure 3.8E). Insertion loss of at least 20 dB was reported for each of the traps at 127.7 MHz (Figure 3.8F). The tuned traps are attached approximately eight centimeters away from the Q-spoiling circuitry of each channel.

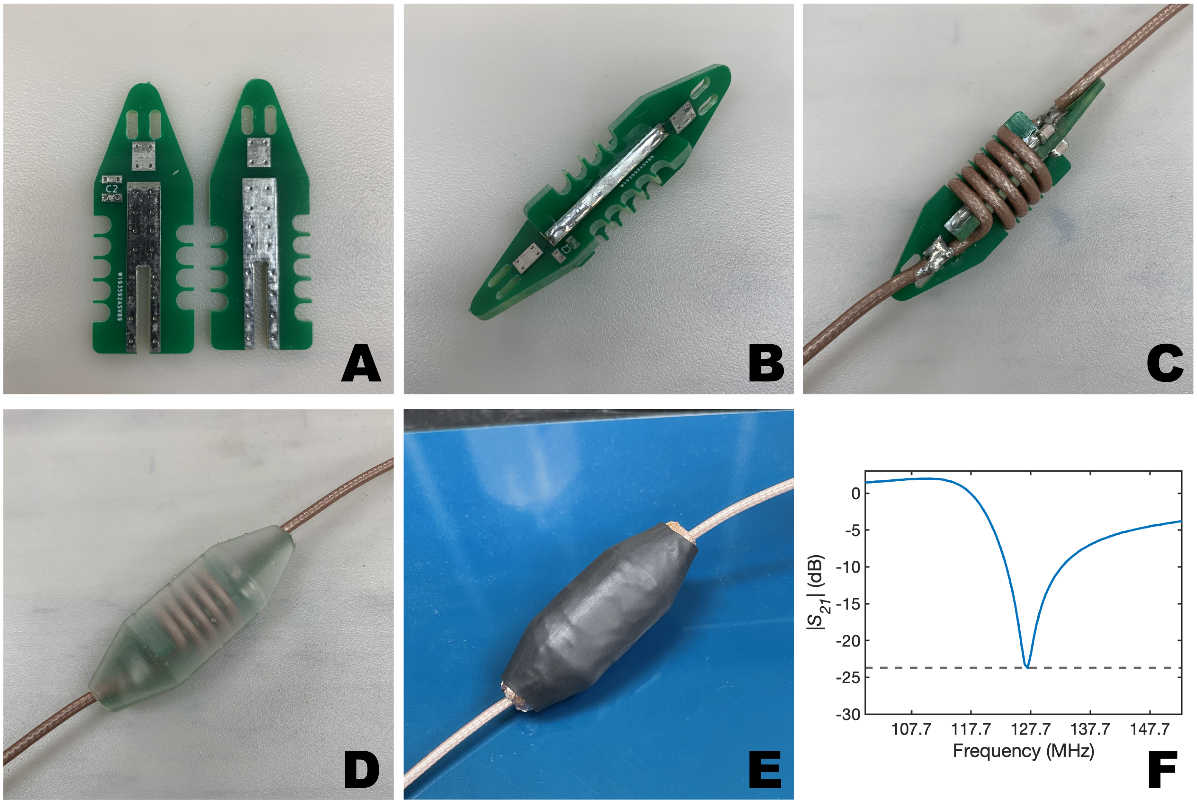

Figure 3.8: A) Pair of printed circuit boards used to form a single trap. B) The two boards soldered together to make a winding guide. C) The coaxial cable wound and attached to the board. D) The placement of the clear 3D printed shield before adding copper tape. E) Trap attached to measurement setup. F) S_{21} of a single trap.

3.2.10 Phantom Imaging

Coil testing was performed with a head shaped loading phantom. The phantom was constructed with two polycarbonate sheets vacuum formed into the shape of the back of a head. The two halves were joined together with nylon screws and a laser cut silicone gasket. The phantom was filled with a solution made with deionized water, 2.4 g/L NaCl, 3.37 g/L $NiCl_2 \cdot 6H_2O$. The additives are used to increase conductivity and shorten T1 recovery and T2 relaxation times. SNR measurements for our eight channel visual cortex coil were performed on a Discovery 3T MR750W scanner (GE Healthcare, Waukesha, WI). The 2D gradient echo scans had a repetition time (TR) of 2000ms, an echo time (TE) of 10ms, a voxel size of 1.2x1.2x5 mm^3, a bandwidth of 122 Hz/pixel, and 16 slices. Data was collected in the sagittal, coronal, and axial planes. Noise measurements were acquired with the same imaging parameters but with the RF transmit coil turned off. SNR maps were calculated in absolute units using noise pre-whitening and optimal coil combination following the methods of Kellman et al.[4].

To verify coil detuning, B1 maps were acquired with a GE product B1 mapping sequence. The sequence was run with the coil in place and repeated after carefully removing the coil without changing the position of the phantom.

Following B1 mapping, the coil was heat tested according to the scanner manufacturer's protocol. This consists of placing the coil array in the scanner without a phantom. The transmit gain is increased and the gradients are turned off. The heat testing sequence is a 2D GRE with a TE of 7ms, TR of 18ms, and a 90^o flip angle. The specific absorption rate (SAR) monitor is disabled and the scan is run for 15 minutes. The coil array, traps, and preamplifer box are imaged with a FLIR E4 thermal camera (Teledyne FLIR, Wilsonville, OR) to detect hot spots. Next the scan is repeated for 1.5 hours with thermal probes placed around the custom hardware.

3.2.11 In-vivo Imaging

After obtaining informed consent, a subject was placed in the coil array and scanned. The scan was performed at UC Berkeley under an Institutional Review Board (IRB) approved protocol (2013-07-5491). Images were acquired with a GE built in 3D T1 weighted Bravo sequence. The scan is an inversion recovery (IR) prepped, fast spoiled gradient echo (FSPGR) sequence. Images were taken with varying resolution.

3.3 Results

3.3.1 Simulation Verification

We are able to quantify the total error in the simulation as the sum of the euclidean distances between each simulated grid point and its equivalent real-world point (Figure 3.3H). Given this error, we ran a sweep of adjustable parameters in the simulation. Since the vacuum

Sandblasting Pressure	R_a (nm)	Sandpaper Grit	R_a (nm)
50 psi	1370.49	120	1632.41
75 psi	2193.37	320	704.53
100 psi	2754	Bare	19.96

Table 3.1: Average surface roughness of sandblasted and manually sanded polycarbonate.

formed plastic is modeled as a set of point masses coupled with springs, these parameters include the spring constants, damping factor, density, and mass. These values were swept to find a set that minimized the global error between the output of the simulation and the reconstructed grid from the 3D scanned vacuum formed plastic. Each parameter was optimized individually while holding the others fixed. The optimization reduced the global error between the simulation and the scanned model by 11%.

3.3.2 Characterization of Surface Roughness and Copper Plating

The surface preparation before plating was optimized by copper plating small strips of polycarbonate with various surface treatments. Our initial experiments shown in Figure 3.9 consisted of manually sanding polycarbonate samples, copper plating them, and conducting a tape test to analyze copper adhesion. As illustrated by the figure, copper adhesion on bare polycarbonate is quite poor so a surface treatment is required. Adhesion tends to improve with increased surface roughness. Regions with an average surface roughness (R_a) of greater than 2 μm consistently passed tape and scratch tests after copper plating. The surface roughness of the polycarbonate samples was measured with a profilometer (Veeco Dektak 6M Stylus Profilometer, New York, USA). Compared to manual sanding, sandblasting provided a more uniform and repeatable surface roughness. With manual sanding, it was also not possible to sand close to the edges of the tape mask.

3.3.3 Eight Channel Visual Cortex Coil

The methods described above were used to design and build an 8 channel coil array for imaging the visual cortex. All of the physical process steps are illustrated in Figure 3.5 and Figure 3.10. A digital 3D model of the back of a head was derived from MRI scan data. The model was modified to accommodate the subject's ears and the ends were tapered to help with the removal of the plastic after vacuum forming. We then fabricated a vacuum forming mold by casting plaster into a CNC milled negative of the head model. A pre-distorted pattern of an eight channel coil design was created with the aid of our vacuum forming simulation software. That pattern was laser cut out of a tape mask and sandblasted into a polycarbonate sheet as shown in Figure 3.5E,F. The tape mask was used as a container for a

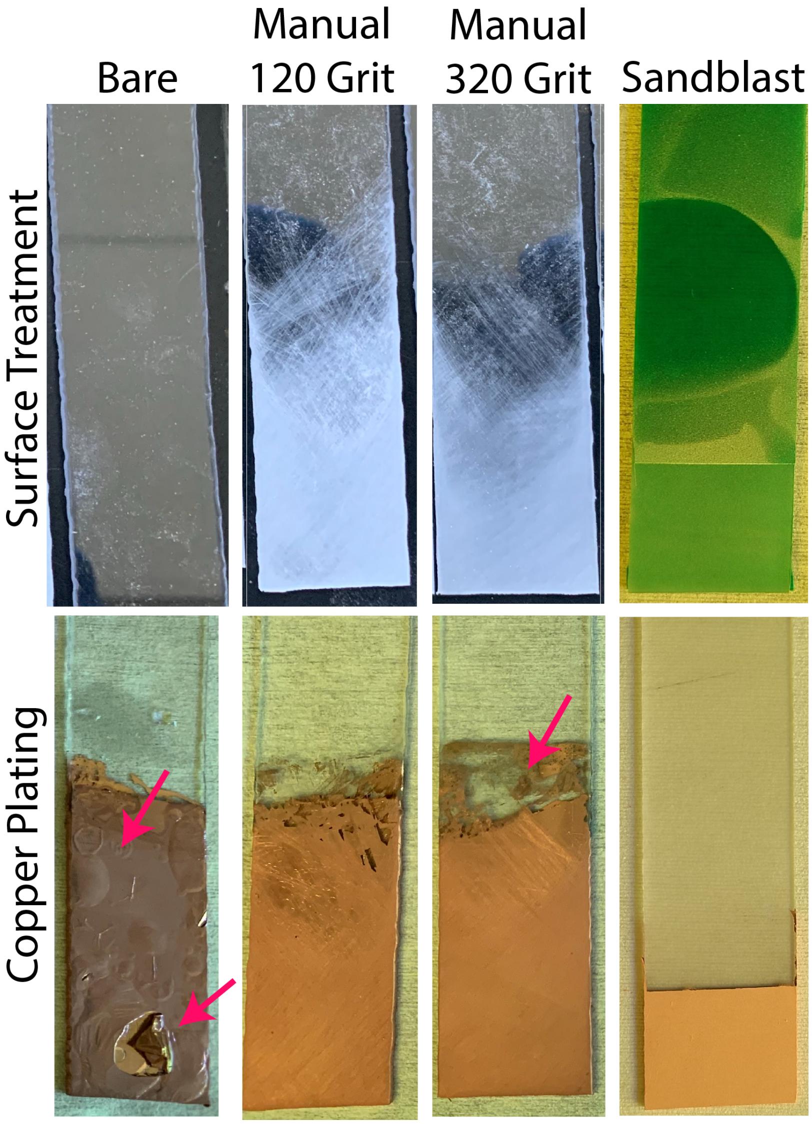

Figure 3.9: Copper plating experiments on small strips of polycarbonate. The strips on top from left to right were left bare, hand sanded with 120 grit sand paper, hand sanded with 320 grit sand paper, and sandblasted with 100 grit white fused aluminum oxide blasting media. All strips were cleaned, catalyzed, and copper plated. Red arrows reveal defects in the copper plating. This indicates that a surface treatment is necessary for copper adhesion and sandblasting produces the most uniform results.

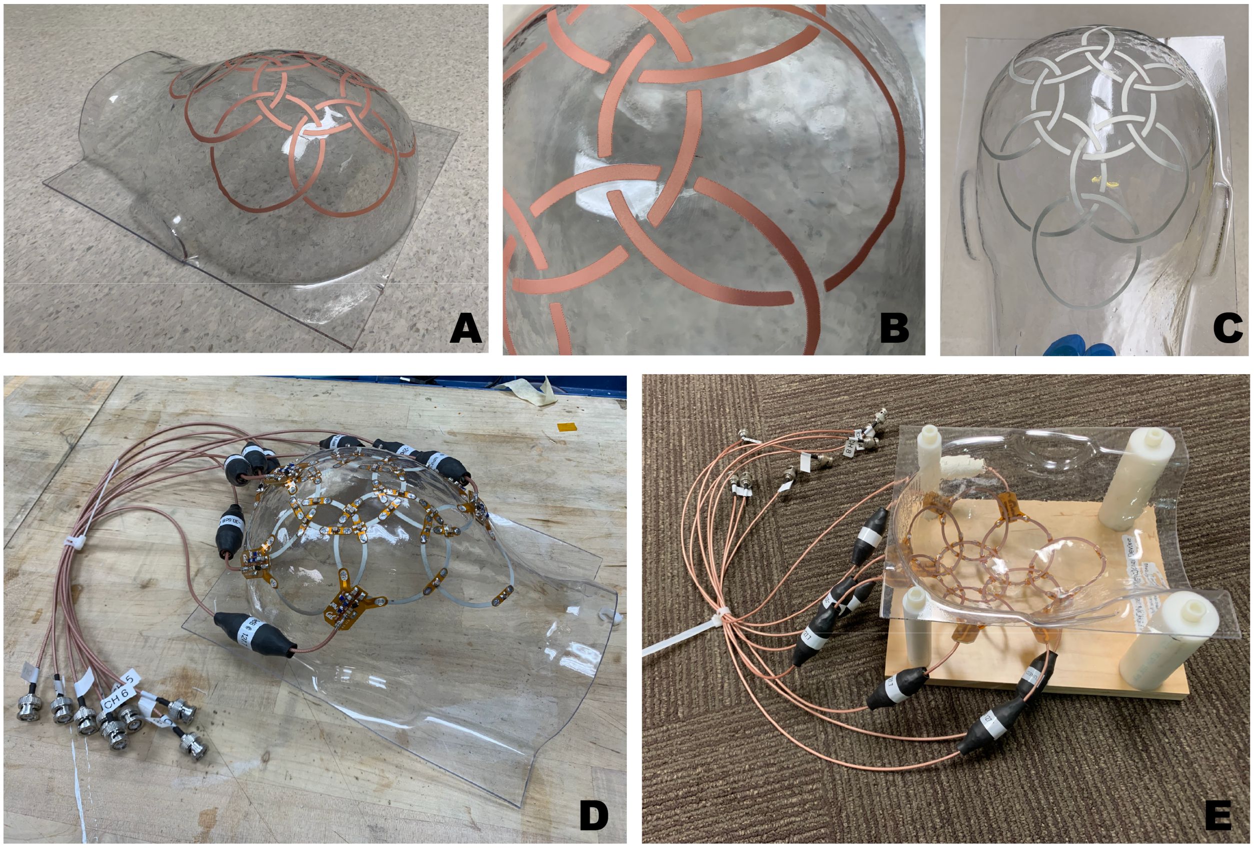

Figure 3.10: Copper plating and populating the vacuum formed substrate. A) The mold is removed, the plastic is trimmed with a bandsaw and the traces are copper plated. B) A close up of the copper reveals a high quality surface finish. C) The copper is passivated with an immersion tin solution. D) Rigid components including cables, traps, and tuning capacitors are added to properly tune and match the coil array. E) The coil is attached to a support created with delrin rods, nylon screws, and plywood.

cleaning solution, a surfactant, and a palladium-tin catalyst which was used to prepare the sanded surfaces for copper plating (Figure 3.5G). The tape was removed and the catalyzed plastic sheet was vacuum formed over the head shaped mold (Figure 3.5H,I,J). The plastic was removed from the mold, trimmed with a bandsaw, and placed into our custom made plating tank (Figure 3.6A). After removal from the plating tank, the substrate was rinsed and the copper traces were submerged in an immersion tin plating solution (Figure 3.10A,B,C). All coils were then tuned and matched with discrete components and flexible printed circuit boards. The final coil array is shown in Figure 3.10D,E.

The individual channels of our coil had an average unloaded Q of 146 and an average loaded Q of 29. The Q-ratio of our coils was 5.03 which indicated body noise dominance. A copper tape coil constructed with the same flexible circuit boards on a polycarbonate substrate produced an unloaded quality factor of 175. The quality factor is likely lower than that of a typical coil made on a fiberglass printed circuit board due to the dielectric losses within the polycarbonate substrate. Network analyzer measurements revealed a strong match with a return loss of more than 30dB per channel when placed on a loading phantom. This is shown in the S11 plot in Figure 3.7B. The Q spoiling circuitry detuned the coils by 63dB and brought the frequency response to the noise floor at the Larmor frequency (Figure 3.7C). To test stability, we measured the average Q ratio for 3 channels after the coil sat in open air for 10 months. The average unloaded Q after that time was 129 and the average loaded Q was 26. This degradation by 12-15% can be explained by the oxidation of the tinned copper surfaces and could be prevented by encapsulating the conductive traces with an inert polymer.

The SNR maps (Figure 3.11A,B) revealed high peripheral SNR with the highest signal exhibited near the surface of the coils. This is due to the coil proximity which is intrinsic to the vacuum formed coil manufacturing method. Since the plastic conforms to a mold of the desired anatomical features, the coils are as close to the subject as possible while maintaining a safe distance to prevent RF burns. The noise correlation matrix (Figure 3.11C) showed some coupling between neighboring coils labeled in Figure 3.11D but excellent decoupling otherwise. B1 mapping was also performed on a loading phantom as shown in Figure 3.11E,F,G. The B1 field was slightly influenced by the presence of the coil array but the lack of major artifacts indicated that the Q-spoiling circuitry was working properly.

In vivo images shown in Figure 3.12 revealed high signal near the surface of the brain.

3.4 Discussion and Conclusions

We present the first example of a receive coil for magnetic resonance imaging created with a combination of vacuum forming and electroless copper plating. With our method, it is possible to make coil arrays that place the receivers as close to the body as possible. This process may enable the rapid development of a set of coils of different sizes. Though our example presented a coil for the visual cortex, it is possible to use our methods to design coils for other parts of the body. In addition, the ability to make bespoke arrays may be useful

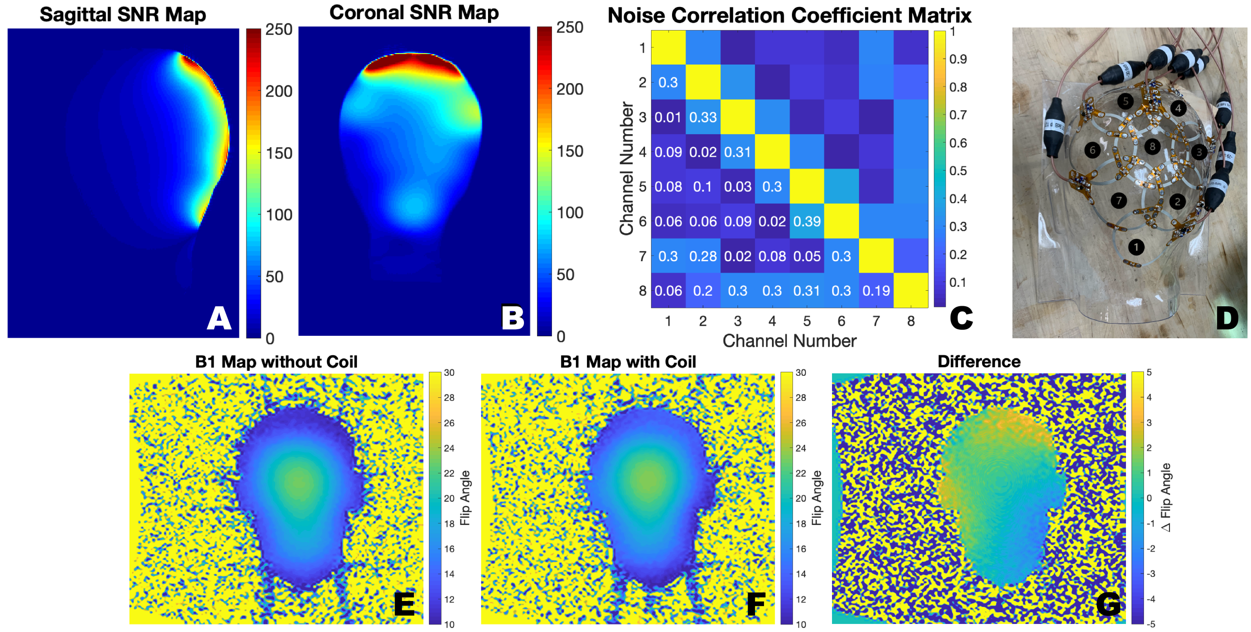

Channel Number	1	2	3	4	5	6	7	8
1								
2	0.3							
3	0.01	0.33						
4	0.09	0.02	0.31					
5	0.08	0.1	0.03	0.3				
6	0.06	0.06	0.09	0.02	0.39			
7	0.3	0.28	0.02	0.08	0.05	0.3		
8	0.06	0.2	0.3	0.3	0.31	0.3	0.19	

Figure 3.11: A) Sagittal SNR map taken on a loading phantom using optimal coil combination and displayed in absolute units. B) Coronal SNR map. C) The noise correlation coefficient matrix. D) Physical layout of the coil channels by coil number. E) B1 map with a loading head shaped phantom without the custom coil array. F) B1 map with the 8 channel coil array on top. G) Difference of the two showing the lack of major B1 variations.

for applications that require motion restriction or reproducible subject placement, such as MR guided radiation therapy or longitudinal fMRI studies.

Our process represents a major step towards additive manufacturing of MRI receive coils but there are many areas for improvement and future work. Though the mechanical simulation produces usable predistorted designs, we measured up to 1 cm of variation between the simulated plastic sheet and a 3D scanned physical sheet. This error was most apparent towards the edges of the head shaped model since the plastic was stretched farther in those regions. The mechanical simulation could be improved by integrating more realistic plastic models as demonstrated in [9].

We explored methods to verify the vacuum forming simulation by 3D scanning a grid printed onto a vacuum formed sheet. Due to the noise and quality of the scan, we were only able to reconstruct the central squares of the grid. In addition, our methods of filtering, edge detection, and construction of the connectivity grid could be improved. The reconstructed points overlayed on our simulated vacuum formed sheet are shown in Figure 3.2H. Despite having to ignore numerous grid points, the points that we were able to reconstruct cover the regions that were patterned by coil geometry.

The electrical simulation was performed with 3 channels on a surface that mimicked the

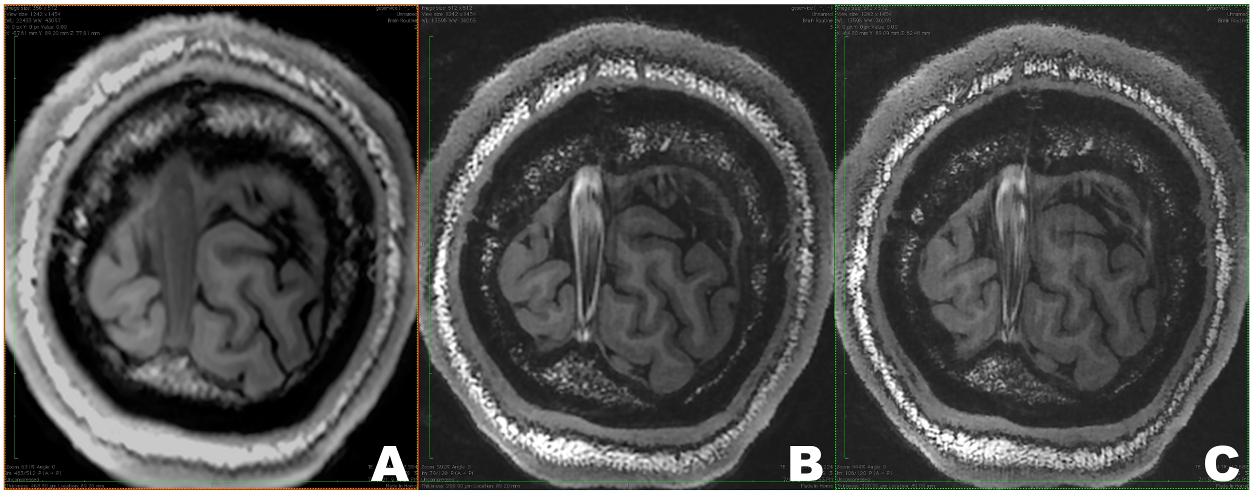

Figure 3.12: In vivo MR images of the visual cortex taken with our 8 channel coil. The scans were acquired with a 3D T1 weighted Bravo sequence with varying resolutions. A) Image taken with 1x1x1 mm^3 voxel size. B) 0.5x0.5x0.67 mm^3. C) 0.37x0.37x0.67 mm^3.

curvature of the back of our head model. This could be improved by importing the full coil design (Figure 3.2F) from the mechanical simulation.

Construction of the coil with this method still requires manual work. The flex PCBs and other rigid components need to be soldered on with care to avoid melting the polycarbonate substrate. Each coil must still be tuned and matched with conventional methods. We did find that all of the coils required approximately the same series capacitance to tune them to the Larmor frequency. It was therefore much easier to finish the rest of the array once one coil was properly tuned and matched. This could improve the speed of manufacturing of MRI coils since the electrical traces can be repeatably patterned on a specific 3D substrate.

Though we focus on MRI coils, it would be possible to use these methods for any circuit. These techniques could expand electronic design beyond conventional, planar printed circuit boards.

Bibliography

[1] Joseph R Corea, Anita M Flynn, Balthazar Lechêne, Greig Scott, Galen D Reed, Peter J Shin, Michael Lustig, and Ana C Arias. Screen-printed flexible mri receive coils. *Nature communications*, 7(1):1–7, 2016.

[2] Chen-Yu Kao and Kan-Sen Chou. Electroless copper plating onto printed lines of nano-sized silver seeds. *Electrochemical and solid-state letters*, 10(3):D32, 2007.

[3] Boris Keil, Vijay Alagappan, Azma Mareyam, Jennifer A McNab, Kyoko Fujimoto, Veneta Tountcheva, Christina Triantafyllou, Daniel D Dilks, Nancy Kanwisher, Weili Lin, et al. Size-optimized 32-channel brain arrays for 3 t pediatric imaging. *Magnetic Resonance in Medicine*, 66(6):1777–1787, 2011.

[4] Peter Kellman and Elliot R McVeigh. Image reconstruction in snr units: a general method for snr measurement. *Magnetic resonance in medicine*, 54(6):1439–1447, 2005.

[5] Ligang Liu, Lei Zhang, Yin Xu, Craig Gotsman, and Steven J Gortler. A local/global approach to mesh parameterization. In *Computer Graphics Forum*, volume 27, pages 1495–1504. Wiley Online Library, 2008.

[6] E Matijevic, AM Poskanzer, and P Zuman. Characterization of the stannous chloride/palladium chloride catalysts for electroless plating. *Plating and Surface Finishing*, 62(10):958–965, 1975.

[7] Peter B Roemer, William A Edelstein, Cecil E Hayes, Steven P Souza, and Otward M Mueller. The nmr phased array. *Magnetic resonance in medicine*, 16(2):192–225, 1990.

[8] Laurent Saboret, Pierre Alliez, Bruno Lévy, Mael Rouxel-Labbé, and Andreas Fabri. Triangulated surface mesh parameterization. *CGAL User and Reference Manual. CGAL Editorial Board*, 4(1), 2019.

[9] Christian Schüller, Daniele Panozzo, Anselm Grundhöfer, Henning Zimmer, Evgeni Sorkine, and Olga Sorkine-Hornung. Computational thermoforming. *ACM Transactions on Graphics (TOG)*, 35(4):1–9, 2016.

[10] R Veleva. Role of potassium ferrocyanide in electroless copper baths. *Surface and Coatings Technology*, 29(2):87–93, 1986.

[11] Jana M Vincent and Joseph V Rispoli. Conductive thread-based stretchable and flexible radiofrequency coils for magnetic resonance imaging. *IEEE Transactions on Biomedical Engineering*, 67(8):2187–2193, 2019.

[12] Ingo Wald, Sven Woop, Carsten Benthin, Gregory S Johnson, and Manfred Ernst. Embree: a kernel framework for efficient cpu ray tracing. *ACM Transactions on Graphics (TOG)*, 33(4):1–8, 2014.

[13] AM Zamarayeva, K Gopalan, JR Corea, MZ Liu, K Pang, M Lustig, and AC Arias. Custom, spray coated receive coils for magnetic resonance imaging. *Scientific Reports*, 11(1):1–9, 2021.

[14] Bei Zhang, Daniel K Sodickson, and Martijn A Cloos. A high-impedance detector-array glove for magnetic resonance imaging of the hand. *Nature biomedical engineering*, 2(8):570–577, 2018.

[15] Yizhong Zhang, Yiying Tong, and Kun Zhou. Coloring 3d printed surfaces by thermoforming. *IEEE transactions on visualization and computer graphics*, 23(8):1924–1935, 2016.

Chapter 4

Quantitative Anatomy Mimicking Slice Phantoms

4.1 Introduction

Magnetic Resonance Imaging (MRI) is a diagnostic tool that provides invaluable clinical information. It can be made sensitive to a variety of biophysical contrast mechanisms including changes in blood oxygenation, flow, diffusion, and differences in soft tissue. While in some cases it is possible to extract quantitative biophysical parameters, standard clinical practice has been predominantly qualitative in nature through contrast weightings. Quantitative imaging could change the way clinicians diagnose, study, and treat diseases. The main drawback of quantitative MRI is the associated long scan time, as multiple measurements must be made to capture the signal evolutions. In recent years, a large effort has been placed on reducing the acquisition time and improving the robustness of quantitative imaging methods. These approaches take advantage of spatio-temporal modeling, e.g. through compressed sensing [13, 6], MR Fingerprinting [14], and machine learning [20].

There is a growing need for realistic phantoms to calibrate and validate these new techniques across different sequences, users, and imaging sites. Most MRI phantoms are made with separate compartments that contain aqueous solutions of paramagnetic ions. Each compartment is designed to mimic certain tissue parameters such as T1, T2, spin density, and diffusion coefficients. Although these phantoms are very useful, they are usually constructed with spheres and cylinders and therefore lack the complicated structure seen in real anatomy. This poses a major drawback, as rapid MRI techniques often make strong modeling assumptions in the reconstruction. Using constraints like Total Variation can produce better results on piece-wise constant phantoms than on real anatomy. That is why the reconstruction community has moved towards prototyping their methods on more anatomically realistic digital phantoms. Phantoms with realistic contrasts and anatomical features could reduce the time required for clinical translation of these ideas, as it would allow researchers to prototype and compare their methods before testing on subjects and volunteers.

MRI phantoms typically use chemicals such as nickel chloride, manganese chloride, copper sulfate, and gadolinium chloride to influence a voxel's T1 and T2 values. Though many phantoms use one chemical, combinations of paramagnetic ions can be used to achieve a wider range of contrasts [18]. Some phantoms use gels, such as agar, to improve structural stability and to mold into more realistic shapes [15, 1]. By adjusting the concentration of agar to water, one can vary T2 without influencing T1. It has also been reported that combinations of agar and sucrose can be used to alter a phantom's apparent diffusion coefficient (ADC) [12]. Polyvinylpyrrolidone (PVP) may also be used to restrict diffusivity [16].

Russek et. al.[17] and Keenan et. al.[11] describe the design, construction, and validation of a highly calibrated system phantom and breast phantom intended for mass manufacturing. These phantoms are becoming the standards for quantitative imaging and are widely used in the field. Though these contributions address a growing need for standardized phantoms, the designs do not include anatomical features and the use of only one chemical produced monotonically increasing T1/T2 pairs. Many phantoms [7, 9] use separate printed compartments to mimic human anatomy. However, phantoms designed with this method cannot reproduce fine structures due to the limitations of three-dimensional printing. Altermatt et. al. [1] described a novel approach for producing highly realistic 3D phantoms using anatomically derived silicone molds. By casting agar in the molds, the authors were able to build a multi-compartment 3D phantom. While their method produced exceptional phantoms, the authors described that some of the anatomical detail was lost due to the fragility of the manufacturing technique.

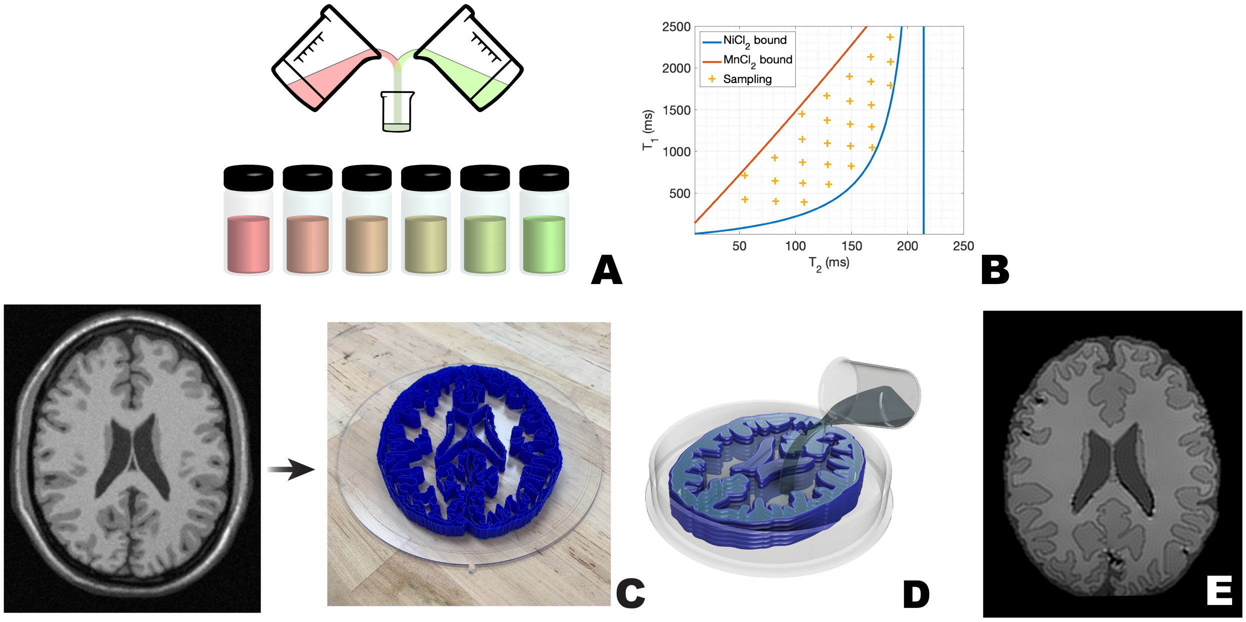

Figure 4.1: Process flow of converting an image of a brain slice into a phantom. (a,b) Solutions of paramagnetic ions $NiCl_2$ and $MnCl_2$ are prepared with agar and salt to calibrate the influence of their concentrations on T1/T2. (c) A slice of a brain is acquired, [4] segmented into compartments, and labeled. The compartment boundaries are 3D printed onto an acrylic sheet. (d) Pre-mixed gels are blended following different linear combinations to target specific R1 and R2 values. Different blend compositions are used to fill each compartment according to the anatomy. (e) Finally, the phantom is scanned for verification and visualized here with a T1-weighted image. Image reproduced from [8].

Another category of phantoms is digital, numerical phantoms. They are frequently used to validate segmentation, reconstruction, and physics based algorithms. The Shepp-Logan phantom is a widely used numerical phantom that uses a set of ellipses to mimic human anatomy [19]. The Brainweb database [4, 5] is one of the most popular digital phantoms for MRI. The phantom consists of ten tissue compartments, and can include mixtures of multiple tissues to emulate multi-compartment relaxation. Guerquin-Kern et al. describe an approach for creating numerical phantoms in k-space with arbitrary shapes based on splines, and include a brain phantom containing multiple compartments[10]. Though digital phantoms are excellent for testing, they cannot model all of the intricacies of scanning a physical object, and they neglect the specific systematic errors present in MR scanners.

In this work we introduce the idea of converting a digital model into a physical phantom so that any segmented data can be realized as a slice phantom. We describe a process for fabricating realistic slice phantoms with anatomy mimicking T1 and T2 contrasts. By deriving a slice phantom from the Brainweb database, we have developed a physical analogue to the digital brain phantom that can be used for actual scanning experiments. The combination of both realistic anatomy and realistic contrast provides a path for creating phantoms that mimic in-vivo scanning and bridges the gap between initial prototyping and human subjects testing of new MR acquisitions and reconstructions.

4.2 Methods

The production of a slice phantom requires three major steps; gel calibration, digital design, and construction and filling. First, two solutions of paramagnetic ions are calibrated to accurately derive the dependence of T1 and T2 on their concentrations within a gel (Fig. 4.1a). Our calibration method is a two step process in which samples of unknown T1/T2 values are prepared, mapped, and fit to a linear model. The parameters from the fit of the crude data are then used to make samples that densely cover the space of attainable T1/T2 values. The mapping procedure is repeated in order to improve the linear fit (Fig. 4.1b).

Next, a model of a slice derived from an image, scan data, or vector file is converted into a set of boundaries that will define the walls of the physical phantom (Fig. 4.1c). The boundaries are then 3D printed onto an acrylic sheet to form separate compartments. These compartments are subsequently filled with gels that are prepared from the calibrated solutions (Fig. 4.1d). Finally, the phantom is sealed with a sheet of acrylic and scanned for verification (Fig. 4.1e).

4.2.1 Gel Preparation and Calibration

A combination of agar, $NiCl_2$, $MnCl_2$, NaCl, and deionized water (DIw) is used to target specific T1/T2 values. Large stock solutions of $NiCl_2$ and $MnCl_2$ are prepared and stored in airtight containers. The use of solutions is preferred since dry chemicals can absorb moisture and introduce inaccuracies over time. The stock is calibrated by preparing samples with varying concentrations of the solutions mixed with agar gel. The compositions of every sample can be found in Table 4.1.

All chemicals were acquired from MilliporeSigma (Burlington, MA). Our stock solutions consist of 500 mL of 25 mM $NiCl_2$ and 500 mL of 10 mM $MnCl_2$ in deionized water (DIw). Larger volumes of water are measured with graduated cylinders (Kimble Kimax, Rockwood, Tennessee). Using an adjustable pipette (Eppendorf, Hamburg, Germany), multiple combinations of each stock solution is added to 20 mL glass vials. Uncertainties were estimated with the manufacturers reported error rates for our equipment. Our pipettes have a systematic error of 0.6% when dispensing 1mL and an error of 5% when dispensing 20μL. The total volume of each vial is adjusted to 5 mL with DIw. At this stage, the concentrations are arbitrarily chosen. We use a grid of values ranging from 0.4 mL to 1.2 mL of the $NiCl_2$ solution and from 0.2 mL to 0.6 mL of the $MnCl_2$ solution. We then prepare a mixture of 300 mL of DIw, 3 g of agar powder (CAS number: 9002-18-0), and 2 g of sodium chloride in a beaker. All solid reagents are weighed with a milligram balance (Mettler Toledo, Columbus,

Initial Mix for Pre Calibration				Calibration				Targeting			
Vial	$NiCl_2$ Sol. (mL)	$MnCl_2$ Sol. (mL)	DIw (mL)	Vial	$NiCl_2$ Sol. (mL)	$MnCl_2$ Sol. (mL)	DIw (mL)	Vial	$NiCl_2$ Sol. (mL)	$MnCl_2$ Sol. (mL)	DIw (mL)
1	0.40	0.10	4.50	1	1.83	0.56	2.61	1	0.09	0.18	4.73
2	0.80	0.10	4.10	2	0.24	0.62	4.14	2	0.53	0.24	4.23
3	1.20	0.10	3.70	3	2.79	0.24	1.97	3	1.81	0.18	3.01
4	0.40	0.20	4.40	4	1.20	0.30	3.50	4	3.67	0.06	1.28
5	0.80	0.20	4.00	5	0.41	0.33	4.26	5	2.64	0.04	2.33
6	1.20	0.20	3.60	6	3.24	0.09	1.67	6	0.08	0.10	4.81
7	0.40	0.30	4.30	7	1.65	0.15	3.20	7	0.57	0.08	4.35
8	0.80	0.30	3.90	8	0.87	0.18	3.96	8	1.68	0.04	3.28
9	1.20	0.30	3.50	9	0.40	0.20	4.41	9	0.55	0.06	4.39
				10	0.09	0.21	4.70	10	0.46	0.05	4.49
				11	1.91	0.06	3.03	11	0.93	0.01	4.06
				12	1.13	0.09	3.78	12	0.03	0.06	4.91
				13	0.66	0.11	4.23	13	0.30	0.03	4.66
				14	0.35	0.12	4.53	14	0.59	0.01	4.40
				15	0.13	0.13	4.74	15	0.40	0.01	4.59
				16	1.30	0.03	3.67	16	0.29	0.01	4.70
				17	0.83	0.05	4.12				
				18	0.52	0.06	4.41				
				19	0.30	0.07	4.63				
				20	0.14	0.08	4.79				
				21	0.96	0.01	4.04				
				22	0.65	0.02	4.33				
				23	0.43	0.03	4.55				
				24	0.26	0.04	4.70				
				25	0.13	0.04	4.83				
				26	0.35	0.00	4.64				
				27	0.22	0.01	4.77				
				28	0.12	0.01	4.87				

Table 4.1: Compositions of each vial made with a 25mM solution of nickel chloride and a 10mM solution of manganese chloride. Each vial was also filled with 15 grams of a hot, aqueous mixture of 1% agar and 0.66% NaCl.

Ohio). The mixture is microwaved for 2-3 minutes until the solution boils and becomes clear. Fifteen grams of the hot gel are added to each vial and thoroughly mixed. The bulk agar gel is covered and placed in a hot water bath in between filling each vial to limit the amount of evaporation.

The samples are then scanned, mapped, and fit to a linear model of R1/R2 vs paramagnetic ion solution volume [18]:

$$\begin{bmatrix} R_1 \\ R_2 \end{bmatrix} = \begin{bmatrix} m_{1,a} & m_{1,b} \\ m_{2,a} & m_{2,b} \end{bmatrix} \begin{bmatrix} k_a \\ k_b \end{bmatrix} + \begin{bmatrix} R_{1,w} \\ R_{2,w} \end{bmatrix}, \tag{4.1}$$

where R_1 and R_2 are the relaxation parameters in seconds, k_a and k_b are the known solution volumes of the two chemicals in mL, and $m_{1,a}$, $m_{1,b}$, $m_{2,a}$, $m_{2,b}$, $R_{1,w}$, and $R_{2,w}$ are the parameters of the linear fit. Rearranging Equation 4.1, we have

$$\begin{bmatrix} R_1 \\ R_2 \end{bmatrix} = \begin{bmatrix} k_a & k_b & 0 & 0 & 1 & 0 \\ 0 & 0 & k_a & k_b & 0 & 1 \end{bmatrix} \begin{bmatrix} m_{1,a} \\ m_{1,b} \\ m_{2,a} \\ m_{2,b} \\ R_{1,w} \\ R_{2,w} \end{bmatrix} \tag{4.2}$$

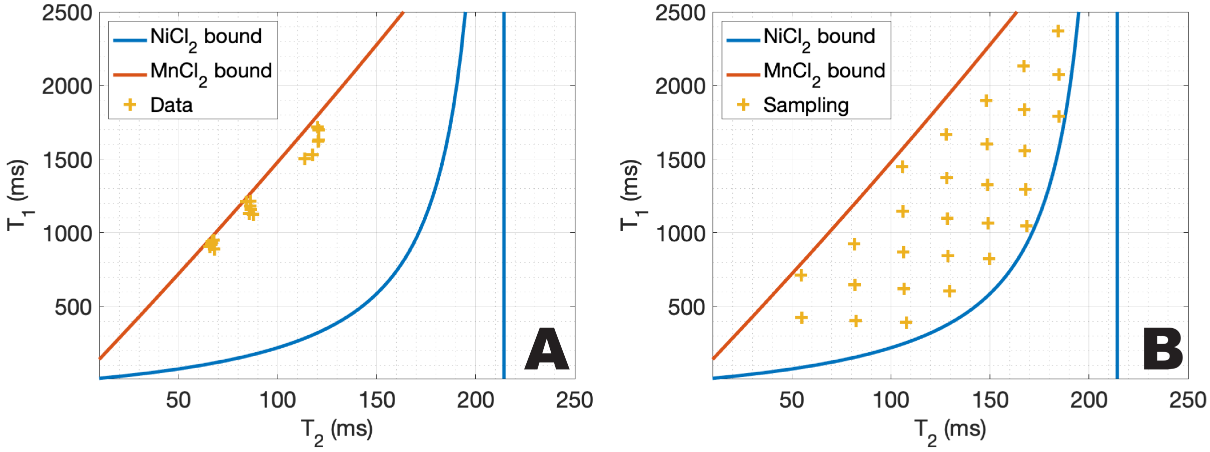

Figure 4.2: Blue and red lines represent the extrapolated T1/T2 values achievable with $NiCl_2$ or $MnCl_2$ alone, respectively. (a) After an initial experiment with arbitrary mixtures, only a small portion of the space is sampled to achieve a rough approximate of the extrapolated fit. (b) The entire mixing, scanning, and mapping procedure is then repeated with a uniform sampling of the attainable T1/T2 pairs to derive a more accurate model. Image reproduced from [8].

After an initial fit based on a small sample size of arbitrary mixtures, the procedure is repeated by uniformly sampling the space of attainable T1/T2 pairs to derive a more accurate fit. To reliably solve for the six unknowns, we use 28 unique mixtures. By using our calibration procedure, the T1 and T2 values are not dependent on making a solution of a specific molarity which is what most phantom literature reports. Accurately making a solution of a specific molar concentration requires specialized glassware. The calibration method permits the use of volumetric measurements to determine T1/T2. Care must be taken to ensure that the temperature remains the same, otherwise it would be possible to perform the calibration using the masses of the solutions. Figure 4.2 depicts the full process of calibration. The red and blue curves represent the extrapolated T1 and T2 values achievable when a single chemical solution is used. Using the linear model parameters, targeted values are chosen, mixed, and mapped, demonstrating the ability to target specific relaxation values. Once the model is validated, gels are created to mimic the relaxation times of human anatomy found in the literature[21].

To derive the relaxation fit, we scanned vials filled with the prepared gel mixtures. The vials were placed in a bath of water to reduce temperature variation and sudden changes in susceptibility. To estimate T1, a single slice was scanned with a slice-selective inversion recovery spin echo (IR-SE) sequence using a repetition time (TR) of 15 seconds and inversion times (TI) of 100, 500, 900, 1300, and 2000 ms. To estimate T2, the same slice was scanned with a multiple pure spin echo (SE) sequences with echo times (TE) of 10, 25, 50, 75, 120ms. Scans were performed with a Siemens 3T Trio (Siemens, Erlangen, Germany) scanner using a commercial 12-channel birdcage head coil. All scans were performed with a 4mm slice thickness and in-plane resolution of 256 x 256. The field of view (FOV) depended on the arrangement and number of vials, but was typically around 140 mm.

After scanning, the raw, complex-valued data were analyzed in Matlab (Mathworks, Natick, MA). A boundary labeling algorithm was used to draw regions of interest (ROI) around each vial. The background along with the edges of the vials were then masked to reduce noise. Outlier pixels beyond 99% of the median intensity were removed from each ROI. The remaining pixels within the ROIs were then used to estimate T1 with an algorithm described in [2] and to estimate T2 with a non linear least squares fit. All mapping was performed on the complex-valued data to reduce bias in the fits due to noise. Following the mapping, Equation 4.2 was solved to derive the model parameters for the stock solution volume versus R1 and R2.

4.2.2 Digital Model Creation

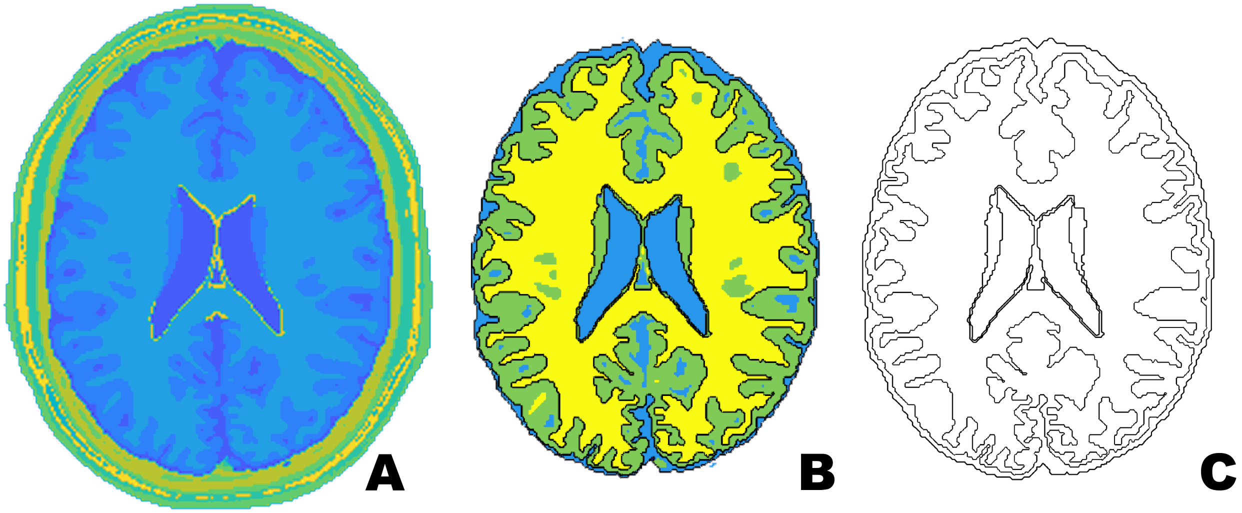

Figure 4.3: (a) An image or vector file (e.g. from an MR scan or digital phantom) is used to create the digital phantom model. (b) The image is segmented into compartments, and undesired segments are removed and the boundary of each compartment is labeled and filtered. (c) The final boundaries are scaled and converted to a common dialect of GCode to be interpreted by a 3D printer. Image reproduced from [8].

The digital model for the slice phantom can be derived from any image or vector file and prepared for digital fabrication. Figure 4.3 shows the process using a slice from the 3D Brainweb data[4]. An axial slice from the Brainweb digital phantom is shown in Figure 4.3a. The segmented areas of the phantom outside the brain, including the skull and skin, are removed with a masking region. The boundaries of the desired slice are automatically labeled with Matlab's image processing toolkit and are displayed as black borders in Figure 4.3b. Boundaries with perimeters below a certain threshold are discarded. Some of the boundaries are offset and trimmed to avoid intersections. Finally, the slice boundaries are directly converted to a standard dialect of GCode to be interpreted by a 3D printer. The toolpath is depicted in Figure 4.3c.

4.2.3 Phantom Fabrication

Each slice phantom is composed of 3D printed internal structures, gel, and an acrylic enclosure. Polylactic Acid (PLA, Hatchbox3D) filament is printed directly onto a 3 mm thick acrylic circle (Fig. 4.4a). PLA forms a strong bond with the acrylic and permits the printing of subsequent layers. The 0.45 mm thick walls are printed to a height of 10 to 15 mm, as shown in Figure 4.4b. The resolution of the method is limited to the resolution of the 3D printer used. We used a custom built 3D printer, though many commercially available printers would work. The base and walls are then sprayed with a commercially available sealing spray (Rust-Oleum, Extra Cover, Satin Clear) to fill in any gaps inherent to 3D printing. A 25mm tall acrylic ring is attached to the base with acrylic cement (TAP Plastics, El Cerrito, California). Figure 4.4c illustrates how each compartment of the phantom is filled with the appropriate gel to target specific T1/T2 values derived from the literature[21]. After the gels are prepared, they are allowed to cool until they are below or near the glass transition temperature of PLA, around 65°C. A beaker is used to fill larger compartments while a syringe is used to fill the smaller cavities. Compartments that are too small can be challenging to fill by hand. Once the gels cool, the phantom is sealed by solvent welding a second acrylic circle to the top of the acrylic ring as shown in Figure 4.4d.

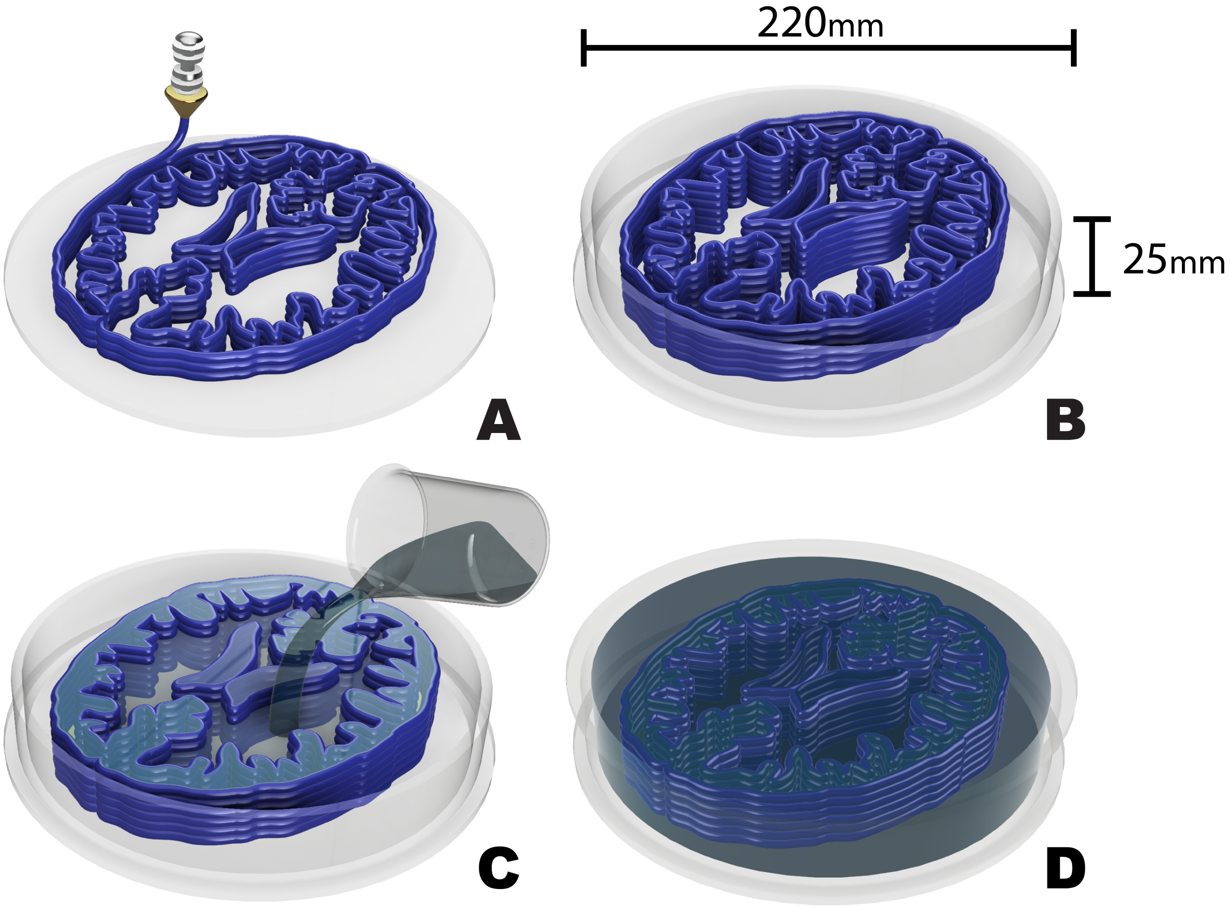

Figure 4.4: (a) Each compartment wall is 3D printed directly onto an acrylic base. (b) The walls are then sealed with an aerosol sealant like acrylic or polyurethane and a surrounding acrylic ring is attached. (c) The compartments of the phantom are then filled with gels with anatomically mimicking T1/T2 contrasts. (d) The surrounding compartment is filled and the phantom is sealed by attaching an acrylic sheet with acrylic cement. Image reproduced from [8].

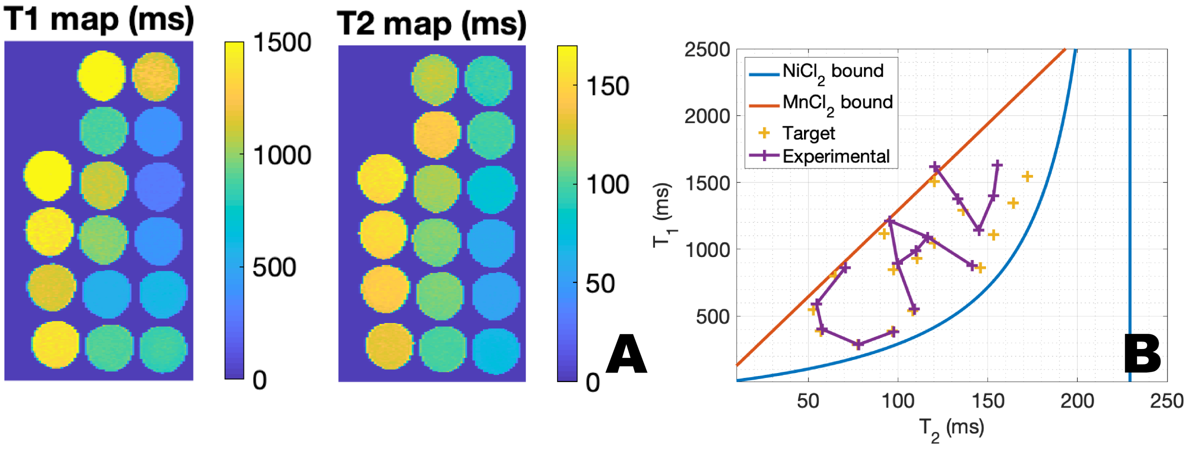

Figure 4.5: (a) The parameter maps of samples targeting specific T1 and T2 values. (b) A plot of the results of the final experiment where targeted values are chosen and samples are mixed and characterized. The experimental values are then compared with the original target values. Image reproduced from [8].

4.3 Results

Figure 4.5 shows the results of the experiment performed after the calibration procedure. The data is obtained by preparing samples to target specific T1 and T2 values then scanning and mapping them with the methods described above. These values are also listed in Table 4.2. The highest error between expected and measured values was 8.6% for T1 and 9.7% for T2. We observed that the error in the T2 measurement generally increased for samples with longer T2 values and we discuss possible reasons in the following section.

An axial brain slice from the Brainweb database was used to build a slice phantom with the methods described above. The 15mm tall PLA boundaries took about two hours to print onto an acrylic base. The multi compartment phantom was filled with gels designed to mimic the CSF, gray matter, and white matter. The concentrations used to make vial 13 and vial 8 in Table 4.2 were used to target gray and white matter, respectively. The CSF was modeled with a lower concentration agar gel (0.5%) with no doping chemicals to have a long T1 and T2.

Figure 4.6a depicts a T1 weighted image of an axial slice of the digital Brainweb model that was used to design the slice phantom. T1 and T2 weighted MR scans of the slice phantom are shown in Figure 4.6 b and c, respectively. Though it is missing some of the smaller features, the physical slice phantom appears qualitatively similar to the digital model. The 0.45mm boundaries between compartments are visible in the scans. Red arrows in Figure 4.6b depict issues with the construction and filling that resulted in air bubbles within

Target T_1 (ms)	Measured T_1 (ms)	Error (%)	Target T_2 (ms)	Measured T_2 (ms)	Error (%)	Vial
288.16	286.70	-0.50	77.49	77.95	0.59	4
387.91	402.94	3.87	56.94	57.67	1.28	3
387.91	384.91	-0.77	96.90	97.71	0.84	5
541.38	552.08	1.98	108.31	109.08	0.71	8
549.05	591.65	7.76	52.95	54.61	3.15	2
800.00	864.51	8.06	65.00	70.73	8.82	1
848.31	893.78	5.36	97.47	99.73	2.32	7
863.66	877.69	1.63	145.98	141.30	-3.21	11
932.72	989.46	6.08	110.59	110.10	-0.44	9
1047.82	1091.74	4.19	120.30	116.51	-3.15	10
1109.21	1142.01	2.96	153.40	144.99	-5.48	14
1116.88	1212.38	8.55	92.33	95.56	3.50	6
1293.37	1378.50	6.58	136.28	133.52	-2.03	13
1347.08	1402.55	4.12	164.24	153.26	-6.69	15
1508.22	1617.57	7.25	120.30	120.55	0.21	12
1546.59	1630.06	5.40	172.24	155.53	-9.70	16

Table 4.2: Expected and achieved values of T_1 and T_2 using the entire calibration procedure. Results are listed in order of increasing T1. The vial number corresponds to the number in the Targeting column of Table 4.1

the phantom. Figure 4.7 showcases another example of a slice phantom made with a sagittal slice from the brain web digital model.

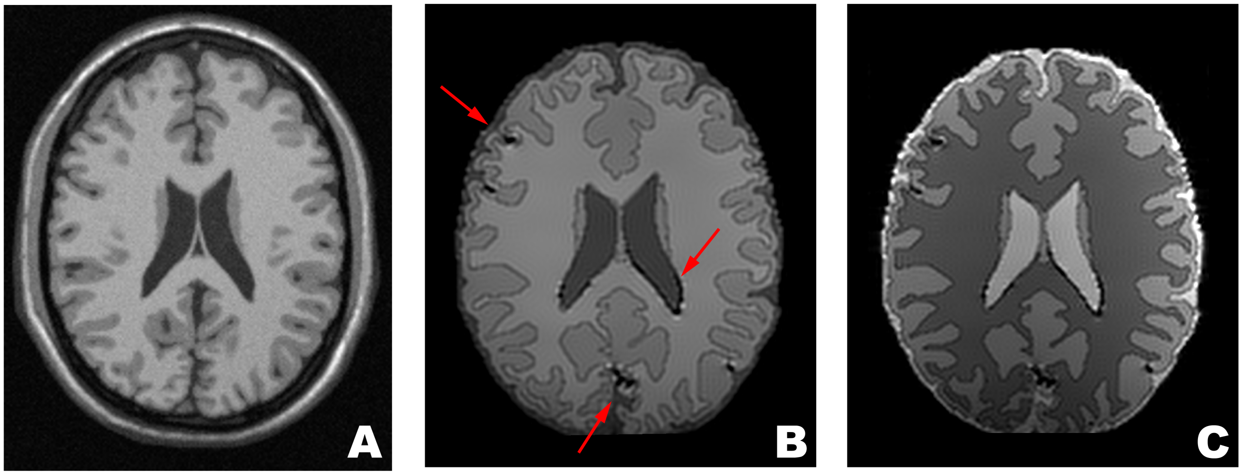

Figure 4.6: (a) The T1 weighted image of the original brainweb model used to design the phantom. (b) T1 weighted IR-SE image of the slice phantom with an inversion time of 2000ms. Arrows point to susceptibility artifacts due to air bubbles and voids. (c) T2 weighted SE image of the slice phantom with an echo time of 90ms. Image reproduced from [8].

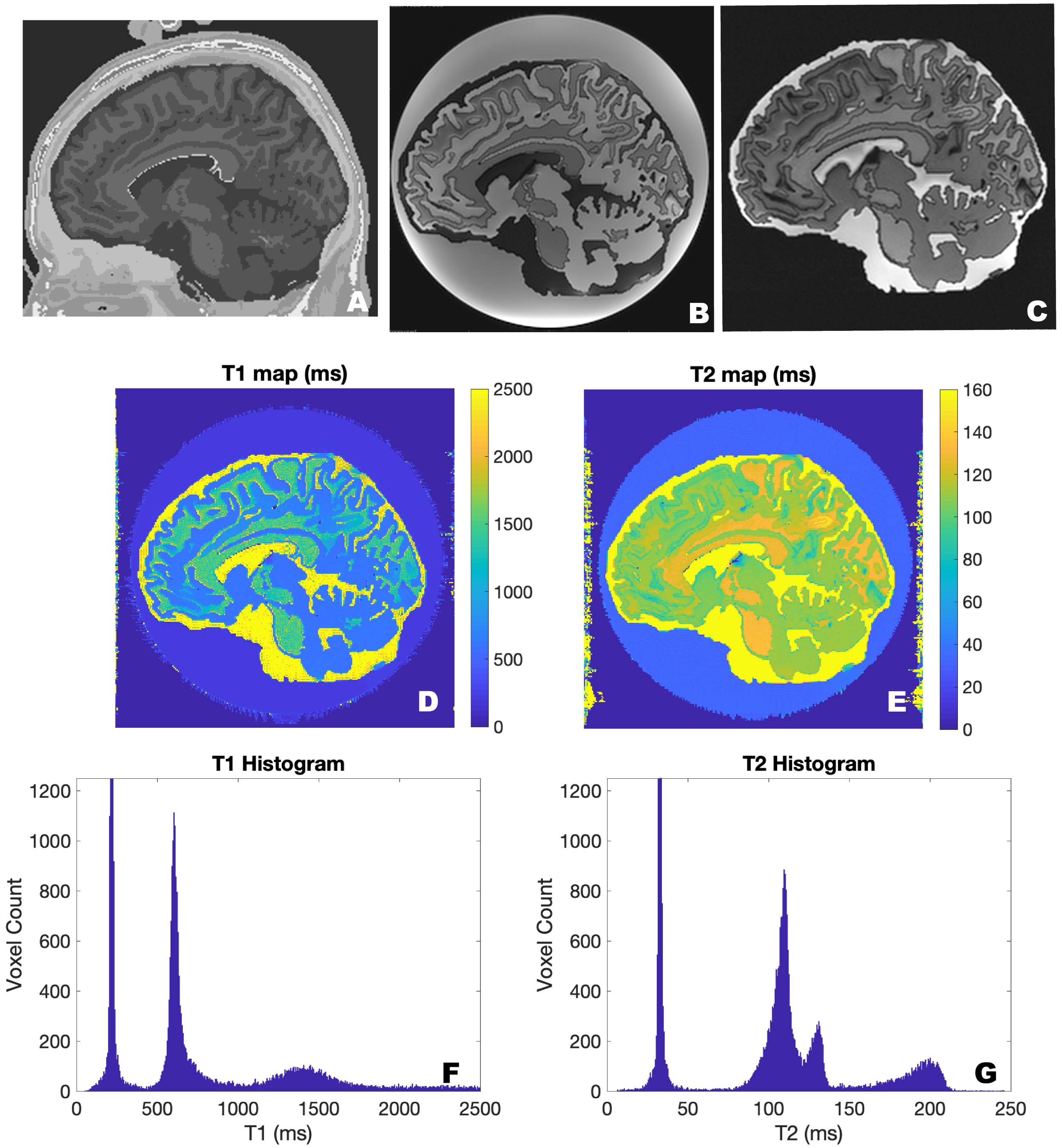

Figure 4.7: (a) A sagittal slice of the original brainweb model used to design the phantom. (b) T1 weighted IR-SE image of the slice phantom with an inversion time of 2000ms and repetition time of 10000ms. (c) T2 weighted SE image of the slice phantom with an echo time of 250ms. (d) The T1 map, (e) the T2 map of the slice phantom as well as relaxivity histograms for (f) T1 and (g) T2. Images of this phantom were acquired with a General Electric 750W scanner (GE, Waukesha, Wisconsin). All scans were performed with a repetition time of 10s and a matrix size of 256x256. Seven spin echo sequences were run with echo times of 10, 25, 50, 75, 120, 175, and 250 milliseconds. Inversion recovery spin echo sequences were performed with an echo time of 14ms and inversion times of 100, 500, 900, 1300, and 2000 milliseconds. Image reproduced from [8].

4.4 Discussion and Conclusions

In this work, we have shown that we can target specific T1/T2 values with less than 10% error. We have also presented a method that uses 3D printing to create anatomically realistic phantoms. Our work represents a step towards truly 3D phantoms that would be hard to distinguish from real anatomy by comparing MRI scans. However, the phantoms presented here have limitations. We noticed that T2 error increases as the target T2 gets larger. This may be due to the small amounts of solution required to make gels with longer T2 values (Eq. 4.1) as dispensing small volumes intrinsically has more error. However, the manufacturer reported error rates of our equipment do not account for the measured discrepancies. Different amounts of evaporation during microwaving and handling the gels could cause changes in gel concentration and apparent T2. In addition, the use of a pure spin echo mapping method could be inaccurate for longer T2 values since diffusion effects can shorten the apparent T2. The use of a multi echo method such as CPMG may reduce the error[3]. Since T1 and T2 values are dependent on the measurement methods, effects like magnetization transfer and diffusion can change the relaxation times. While we chose particular sequences and methods for scanning and mapping, there are numerous other techniques that could be used to calibrate the parameters of the phantom. Our phantoms are physical representations of true anatomy and the method that we developed could easily be extended to print structures with arbitrary geometries. This work could be extended by stacking multiple slice phantoms to create a "2.5D" phantom, providing the ability to create high in-plane resolution with varying anatomy across the slice direction.

Our phantoms have not been validated with long term stability tests. With improper sealing, the agar gel could become dehydrated and change contrast. Acrylic is also not a perfect moisture barrier so some water will leech through over time. PLA is biodegradable and hygroscopic so it may affect the relaxation times of the gels if the sealant fails. In addition, the phantoms have a risk of mold growth if they are not prepared in a sterile environment or mixed with an antibacterial chemical or preservative such as ProClin 150, EDTA, or alcohol. We have also noticed problems with air bubbles. Gases dissolved in the gels can cling to the walls of phantom as the gels cool. These bubbles can lead to susceptibility artifacts as illustrated by red arrows in Figure 4.6b. This problem could be mitigated by degassing the solutions and preparing the phantoms in a nitrogen environment. Our phantoms only model T1 and T2 though parameters like diffusion, susceptibility, and proton density would be desirable.

We see digital manufacturing playing a large role in the development of MRI hardware. With recent developments in additive processing, high resolution three dimensional phantoms could be printed directly from a scan. Going beyond T1 and T2, parameters like diffusion and susceptibility could be modeled and realized with multi material 3D printing. In addition, a phantom that is easy to manufacture could become widely used in the MR community. The work presented here is a small step towards standardized, realistic, and high quality phantoms.

Bibliography

[1] Anna Altermatt, Francesco Santini, Xeni Deligianni, Stefano Magon, Till Sprenger, Ludwig Kappos, Philippe Cattin, Jens Wuerfel, and Laura Gaetano. Design and construction of an innovative brain phantom prototype for mri. *Magnetic resonance in medicine*, 81(2):1165–1171, 2019.

[2] Joëlle K Barral, Erik Gudmundson, Nikola Stikov, Maryam Etezadi-Amoli, Petre Stoica, and Dwight G Nishimura. A robust methodology for in vivo t1 mapping. *Magnetic resonance in medicine*, 64(4):1057–1067, 2010.

[3] Noam Ben-Eliezer, Daniel K Sodickson, and Kai Tobias Block. Rapid and accurate t2 mapping from multi–spin-echo data using bloch-simulation-based reconstruction. *Magnetic resonance in medicine*, 73(2):809–817, 2015.

[4] Chris A Cocosco, Vasken Kollokian, Remi K-S Kwan, G Bruce Pike, and Alan C Evans. Brainweb: Online interface to a 3d mri simulated brain database. In *NeuroImage*. Citeseer, 1997.

[5] D Louis Collins, Alex P Zijdenbos, Vasken Kollokian, John G Sled, Noor J Kabani, Colin J Holmes, and Alan C Evans. Design and construction of a realistic digital brain phantom. *IEEE transactions on medical imaging*, 17(3):463–468, 1998.

[6] Mariya Doneva, Peter Börnert, Holger Eggers, Christian Stehning, Julien Sénégas, and Alfred Mertins. Compressed sensing reconstruction for magnetic resonance parameter mapping. *Magnetic Resonance in Medicine*, 64(4):1114–1120, 2010.

[7] Karthik Gopalan, J Tamir, A Arias, and Michael Lustig. Toward 3d printed, anatomy-mimicking, quantitative mri phantoms. In *Proceedings of the 25th Meeting ISMRM, Honolulu*, 2017.

[8] Karthik Gopalan, Jonathan I Tamir, Ana C Arias, and Michael Lustig. Quantitative anatomy mimicking slice phantoms. *Magnetic resonance in medicine*, 86(2):1159–1166, 2021.

[9] Nadine N Graedel, Jonathan R Polimeni, Bastien Guerin, Borjan Gagoski, and Lawrence L Wald. An anatomically realistic temperature phantom for radiofrequency heating measurements. *Magnetic resonance in medicine*, 73(1):442–450, 2015.

[10] Matthieu Guerquin-Kern, Laurent Lejeune, Klaas Paul Pruessmann, and Michael Unser. Realistic analytical phantoms for parallel magnetic resonance imaging. *IEEE Transactions on Medical Imaging*, 31(3):626–636, 2011.

[11] Kathryn E Keenan, Lisa J Wilmes, Sheye O Aliu, David C Newitt, Ella F Jones, Michael A Boss, Karl F Stupic, Stephen E Russek, and Nola M Hylton. Design of a breast phantom for quantitative mri. *Journal of Magnetic Resonance Imaging*, 44(3):610–619, 2016.

[12] Ioannis Lavdas, Kevin C Behan, Annie Papadaki, Donald W McRobbie, and Eric O Aboagye. A phantom for diffusion-weighted mri (dw-mri). *Journal of Magnetic Resonance Imaging*, 38(1):173–179, 2013.

[13] Michael Lustig, David Donoho, and John M Pauly. Sparse mri: The application of compressed sensing for rapid mr imaging. *Magnetic Resonance in Medicine: An Official Journal of the International Society for Magnetic Resonance in Medicine*, 58(6):1182–1195, 2007.

[14] Dan Ma, Vikas Gulani, Nicole Seiberlich, Kecheng Liu, Jeffrey L Sunshine, Jeffrey L Duerk, and Mark A Griswold. Magnetic resonance fingerprinting. *Nature*, 495(7440):187–192, 2013.

[15] Matthew D Mitchell, Harold L Kundel, Leon Axel, and Peter M Joseph. Agarose as a tissue equivalent phantom material for nmr imaging. *Magnetic resonance imaging*, 4(3):263–266, 1986.

[16] C Pierpaoli, J Sarlls, U Nevo, PJ Basser, and F Horkay. Polyvinylpyrrolidone (pvp) water solutions as isotropic phantoms for diffusion mri studies. In *Proc Intl Soc Magn Reson Med*, volume 17, page 1414, 2009.

[17] SE Russek, M Boss, EF Jackson, DL Jennings, JL Evelhoch, JL Gunter, and AG Sorensen. Characterization of nist/ismrm mri system phantom. In *Proceedings of the 20th Annual Meeting of ISMRM, Melbourne, Australia*, page 2456, 2012.

[18] Nicholas J Schneiders. Solutions of two paramagnetic ions for use in nuclear magnetic resonance phantoms. *Medical physics*, 15(1):12–16, 1988.

[19] Lawrence A Shepp and Benjamin F Logan. The fourier reconstruction of a head section. *IEEE Transactions on nuclear science*, 21(3):21–43, 1974.

[20] Ge Wang, Jong Chu Ye, Klaus Mueller, and Jeffrey A Fessler. Image reconstruction is a new frontier of machine learning. *IEEE transactions on medical imaging*, 37(6):1289–1296, 2018.

[21] Janaka P Wansapura, Scott K Holland, R Scott Dunn, and William S Ball Jr. Nmr relaxation times in the human brain at 3.0 tesla. *Journal of Magnetic Resonance Imaging: An Official Journal of the International Society for Magnetic Resonance in Medicine*, 9(4):531–538, 1999.

Chapter 5

Conclusions and Future Outlook

5.1 Summary

This dissertation presented new methods for tailoring MRI coils and phantoms to the body. Chapters 2 and 3 discussed two techniques for creating rigid receive coil arrays that conform to complex geometries found on the body. The first method involved spray coating silver nanoparticle inks and polystyrene dielectric materials to form resonant coils on 3D printed substrates. The coil geometries were spray coated through a 3D mask which could enable rapid manufacturing. This method was used to make a bespoke four channel coil array for imaging the neck and carotid artery. The signal to noise ratio of this coil was significantly higher (1.4x in the center, 5x in the periphery) than the SNR of a commercially available coil designed to fit the majority of subjects.

The second method for creating anatomically inspired coils involved vacuum forming and electroless copper plating. We started with a 3D scan of a desired anatomy which was used to lay out coil elements. The layout was pre-distorted with a self built simulation of the vacuum forming process and the geometric overlaps were tested with HFSS. Next, the desired coil pattern was sandblasted onto a polycarbonate sheet through a tape mask. The sandblasted areas were catalyzed with a palladium-tin solution and the plastic was vacuum formed. The catalyzed, three dimensional part was placed into a custom built plating tank and copper plated. Rigid components were attached to the copper traces to form resonant receive coils. An 8 channel visual cortex coil was built to highlight the capabilities of this method. Coil measurements were performed on the bench and in the scanner. The manufacturing method can create coil arrays that are as close to the body as possible. This process may enable the rapid development of a set of coils of different sizes for applications ranging from longitudinal fMRI studies to MR guided therapies.

Chapter 4 discussed a technique for creating quantitative anatomy mimicking slice phantoms. The chapter described a reproducible method for calibrating a basis set of chemical solutions that could be used to make gels with varying T1 and T2 values. We were able to target specific T1/T2 values with less than 10% error. Additionally, our slice phantoms looked more realistic than commercially available phantoms since their geometries are derived from anatomical data. Standardized and accurate tools for validating new techniques across sequences, platforms, and different imaging sites are important. Anatomy mimicking, multi-contrast phantoms designed with our procedures could be used for evaluating, testing, and verifying model based methods.

5.2 Future Outlook

The work presented here shows the potential to make receive coil arrays that perfectly conform to the body. In order to be commercially viable, it would be necessary for the process to be more streamlined. Future work could explore automating the creating of a coil array directly from a 3D scan of a body part. One could envision a process where a subject is 3D scanned, the coil geometries are automatically designed and simulated, and a coil array is printed without human intervention. Accomplishing this vision of a fully automated coil design would have a massive impact on procedures like MR guided radiation therapy where motion restriction and high SNR are important.

Though the work here describes the use of electroless plating and spray coating for MRI coils, it would be possible to use these methods for other electronics. Being able to pattern conductors on 3D surfaces could change the way electronics are designed. At the time of writing, most electronics are designed to be manufactured on planar substrates like polyimide or FR-4. The ability to move electronics out of the plane could enable the creation of new antenna designs or could simplify the integration of electronics into consumer products.

The work described in the chapter on phantoms focused on a casting gels into a 3D printed structure. The next step towards anatomically realistic phantoms could involve 3D printing the gels themselves. To realize this goal, it would be necessary to do a full characterization of new gels that could be printed. One avenue that is currently being explored in our lab is the use of UV curable hydrogels. These gels are made with water, a monomer, a crosslinker, and a photoinitiator and can be fully cured with a 405 nm UV lamp. The gels can also be doped with paramagnetic ions in order to alter their T1/T2 contrast. With advanced printing techniques like inkjet printing, it would be possible to deposit UV curable hydrogels to print an entire phantom. This phantom could have significantly more anatomical detail since it would not have separate compartments. A manufacturing method to create a phantom that is indistinguishable from a human scan would be immensely powerful.

This dissertation hopes to change the way MRI hardware is designed. We hope that coil designers will be inspired by these methods to make many sizes of coils to ensure the optimal fit for everyone. In the future, every scanner site could have a set of coils for many shapes and sizes instead of using a one size fits all model. In addition, the future of MRI phantoms should have anatomically realistic structure and contrast rather than simplified structures like spheres and cylinders. Tailoring the hardware to interface with and look like the body will be the next step forward in magnetic resonance imaging.